Laser-based Powder Bed Fusion of Zirconium-based Metallic Glass in the MARS-M Sounding Rocket Payload

Dissertation
zur Erlangung des Grades
der Doktorin der Ingenieurwissenschaften

der
Naturwissenschaftlich-Technischen Fakultäten

der
Universität des Saarlandes

in Zusammenarbeit mit dem
Deutschen Zentrum für Luft- und Raumfahrt

von
Mélanie Anne Clozel

Saarbrücken, 2025

Tag des Kolloquiums: 24.06.2025

Dekan: Prof. Dr.-Ing. Dirk Bähre

Berichterstatter: Prof. Dr. Ralf Busch
Prof. Dr.-Ing. Dirk Bähre

Akad. Mitarbeiter: Dr.-Ing. Florian Schäfer

Vorsitz: Prof. Dr. Karen Lienkamp

CV & Scientific career

Name:	**Mélanie Anne Clozel**
Birthdate:	29.10.1991
Birthplace:	Lyon, France
ORCID:	0000-0002-1071-3309

2020–2024	PhD student, Institute of Material Physics in Space, German Aerospace Centre (DLR), Cologne, Germany • *2 papers published, 1 under review*
2018–2020	Researcher, Materials Science Lab (LBM), National Centre for Nuclear Research (NCBJ) Świerk-Otwock, Poland • *Responsible for Nanoindentation devices and experiments* • *Local partner for European research project M4F (Materials for Fission and Fusion, Horizon2020), conducted nanomechanical testing of low energy ion-irradiated materials* • *Obtained the Young Scientist Grant (Government of Poland)* • *9 papers published*
2014–2017	Double-diploma MSc student, Department of Mechanics, INSA Rouen, France and Faculty of Mechanical and Process Engineering, RPTU Kaiserslautern-Landau, Kaiserslautern, Germany • *Master's in Materials and Process science* • *Thesis: Processing and characterisation of bulk metallic glasses (with the Wrocław University of Science and Technology, Poland)*
2010–2014	Engineering student, Department of Mechanics, National Insitute of Applied Sciences (INSA), Rouen, France
2010	French Baccalauréat Général, Lycée Juliette Récamier, Lyon, France • *Additional course: History-Geography class in German* • *6-month exchange with pupil from Theodor Heuss Gymnasium, Göttingen, Germany*

Publications

Parts of this thesis have already been published in

- Neumann, C. *et al.* Additive manufacturing of metallic glass from powder in space. *NPJ microgravity* **9,** 80. ISSN: 2373-8065 (2023)
- Zocca, A. *et al.* Challenges in the Technology Development for Additive Manufacturing in Space. *Chinese Journal of Mechanical Engineering: Additive Manufacturing Frontiers* **1,** 100018. ISSN: 27726657 (2022)

Manuscript accepted on 19th of July 2025:

- Clozel, M. *et al.* Microstructure formation during gas flow-assisted additive manufacturing of a metallic glass powder on ground and in microgravity. *Progress in Additive Manufacturing* (2025)

Parts of this work were presented at

- 17th European Congress and Exhibition on Advanced Materials and Processes – FEMS EUROMAT, 2023, Frankfurt-am-Main, Germany. Talk title: *PBF-LB of metal powders in microgravity.*
- RQ 17 & ISMANAM 27 Conference, 2023, Warsaw, Poland. Poster title: *PBF-LB of AMZ4 powder in microgravity.*
- DLR Doctoral Symposium, 2022, Hamburg, Germany. Poster title: *3D printing of Zr-based bulk metallic glasses in microgravity.*
- International School of Crystallography, 2022, Erice, Italy. Poster title: *3D printing of Zr-based bulk metallic glasses in microgravity.*

Acknowledgements

I would like to thank several people, of which:

Prof. Andreas Meyer, Prof. Ralf Busch, and Prof. Daniela Zander, who allowed this work to happen officially.

Dr. Christian Neumann, Johannes Thore, Dr. Fan Yang, who allowed this work to happen – in practice! Thank you Fan for your patience at my repeated questions, I hope you did not get too many grey hairs because of having me as a PhD student . . .

Dr. Matthias Kolbe for guidance and instruction using SEM, EDS, and EBSD, Dr. Nuria Navarrete Argiles for help with the vacuum furnace, and Dr. Carolina Villada Vargas for help with understanding DSC.

The library team of the DLR Köln-Porz: Astrid Bölt and Regina Kraus for finding publications for me.

Katarzyna Mulewksa and Edyta Wyszkowska for nanoindentation at the NCBJ, Poland, it was a pleasure to work with you again. Dr. Janka Wilbig for help with the powder characterisation at the BAM, Germany. Dr. Christoph Altenbach and Chijioke Kenneth Akuata for transmission electron microscopy from the RWTH Aachen, Germany. Dr. Olof Gutowski and Dr. Ann-Christin Dippel for synchrotron measurements at Beamline P07, and Dr. Azat Khadiev at Beamline 27, PETRA III, DESY, Hamburg, Germany, for their help with ex-situ and in-situ synchrotron measurements, respectively. Lucas Ruschel for the DSC measurements at the Uni Saarland.

Members of the Sámi people for their help in retrieving the sounding rocket payload (which involved health and safety of team members and safe transportation of the payload from the point of impact to the helicopter, i.e. the lending of a warm coat, a wooden sleigh covered in reindeer pelts, and a ski-mobile).

As to my fellow PhD students at the institute, a special thanks to Ya-Chun, Benni, Gwen, Marlo, Juan-Carlos, Louisa, Kathi, Will, Marimel, Nico, and all the others, I really enjoyed the weekly coffee morning chats, you made the stress and pressure of PhD student life more bearable!

And last but not least, thank you Asbjørn, colleague, friend, partner, eternal support, LaTeX formatting nerd, and father to our little Astrid, your help through this was invaluable.

Abstract

Additive Manufacturing (AM) technologies offer great opportunities to meet the challenges of the space industry thanks to the reduction of material usage, mass to transport, as well as production time. Though the use of polymer AM on the ISS is undoubtedly a success, metal-based AM is bound to become a requirement for future space exploration missions. Laser-based Powder Bed Fusion is an AM process able to achieve complex geometries unattainable to traditional manufacturing techniques in one piece, and can use any feedstock materials thanks to scalable process parameters. Since their birth in the 1960s, metallic glasses – amorphous metals with potentially very attractive properties – have improved in glass-forming ability to become *bulk* metallic glasses, extending their field of application. However, their size is still limited by their traditional production by casting or thermoplastic forming (from millimetre to centimetre range) due to decreasing cooling rates and ensuing crystallisation, generally deteriorating the attractive properties sought after. AM has recently proved to be a game-changer for these innovative materials, as it has allowed them to sidestep the size limitations by building bit by bit, producing an amorphous item larger than traditionally possible. Here we explore this union specifically in this domain by manufacturing parts from BMG in a powder-based process independent of gravity, in the lab and in a sounding rocket.

Zusammenfassung

Additive Fertigung (AM) ist eine Chance, die Herausforderungen der Raumfahrtindustrie zu meistern, da sie den Materialverbrauch, die zu transportierende Masse und die Produktionszeit reduziert. Obwohl der Einsatz von Polymer-AM auf der ISS ein Erfolg ist, wird metallbasierte AM für künftige Raumfahrtmissionen unweigerlich zur Voraussetzung. Das pulverbettbasiertes Schmelzen von Metall mittels Laserstrahl ist ein AM-Prozess, mit dem komplexe Geometrien erreicht werden können, die mit herkömmlichen Herstellungsverfahren in einem Stück nicht möglich sind. Seit ihrer Erfindung sind Metallische Gläser – amorphe Metalle mit potenziell sehr attraktiven Eigenschaften – zu "bulk" metallischen Gläser geworden, was ihren Anwendungsbereich erweitert. Ihre Größe ist jedoch nach wie vor durch ihre traditionelle Herstellung durch Gießen oder thermoplastische Verformung aufgrund abnehmender Abkühlungsraten und der daraus resultierenden Kristallisation begrenzt, was im Allgemeinen die angestrebte Eigenschaften beeinträchtigt. AM erlaubt aber diese Materialien, die Größenbe-schränkungen umzugehen, indem sie Stück für Stück ein amorphes Objekt herstellen, das größer ist als traditionell möglich. Hier erforschen wir diese Verbindung speziell in dem Raumfahrtbereich, indem wir Teile aus BMG in einem pulverbasierten Prozess unabhängig von der Schwerkraft im Labor und in einer Höhenforschungsrakete herstellen.

Contents

List of Figures

Acronyms

μXRD X-ray Micro-Diffraction.

AM Additive Manufacturing.

BAM Bundesanstalt für Materialforschung und -prüfung.

BMG Bulk Metallic Glass.

CT Computer Tomography.

EBSD Electron Backscatter Diffraction.

EDS Energy Dispersive Spectroscopy.

FFF Fused Filament Fabrication.

FIB Focused Ion Beam.

GFA Glass-Forming Ability.

GSE Ground Support Equipment.

ISRU In-Situ Ressource Utilisation.

LM Light Microscopy.

MAPHEUS MAterialPHysikalische Experimente Unter Schwerelosigkeit.

PBF-LB Laser-based Powder Bed Fusion.

SEM Scanning Electron Microscopy.

TEM Transmission Electron Microscopy.

TTT Time-Temperature Transformation.

XRD X-ray Diffraction.

Chapter 1

Introduction

Imagine an astronaut on the Moon. Or Mars, for that matter. She is preparing a device that will be launched on the surface to collect information. This is a routine task, one that she and her colleagues have performed many times. So many, in fact, that upon tightening the last screw – crack! The head breaks off. In the harsh space environments, equipment fatigue, wear, or simply loss, are and will be problematic for astronauts and future space explorers. It is estimated that at any given time, about 2 % of spare parts are lost onboard the ISS [4]. Resupplying the ISS – which is *only* 400 km from Earth – has proved hazardous at times [5]. Astronauts will not be able to rely so heavily on Earth from the Moon and beyond. They need their own manufacturing systems. Additive Manufacturing (AM) technologies offer great opportunities to meet the challenges of the space industry due to the possibilities they present: reduction of material usage, mass to transport, as well as production time. They are optimal for the fabrication of unique or small series parts.

Additionally, they could allow the use of materials recycled or extracted on-site, so-called In-Situ Ressource Utilisation (ISRU). NASA and Made In Space, Inc., proved the feasibility of polymer-based AM in microgravity by running a Fused Filament Fabrication (FFF) printer on the International Space Station. Without downplaying this success, firstly polymer tools and parts cannot replace metal in terms of mechanical construction and structures, and secondly, of the spare parts mentioned above, about 17 % are metallic objects [4]. This should certainly encourage the research and development of metal-based AM applied to space applications.

One of the earliest AM processes, Laser-based Powder Bed Fusion (PBF-LB) is also one of the most popular. It can achieve strikingly complex geometries unattainable to traditional manufacturing techniques in one piece, using virtually any feedstock materials thanks to highly scalable process parameters [6–17]. Though this technology has matured over the recent years and become – in some cases – a satisfactory alternative for building structural parts subjected to static high stresses, there are still many issues to deal with: the complexity of the thermal history of each area of the 3D build can affect the microstructure in intricate and so far hardly foreseeable ways.

Meanwhile, metallic glasses were born in the early 1960s and so are a relatively new class of materials. As compositions with higher glass-forming ability were developed, these glasses increased in size and became Bulk Metallic Glass (BMG) in the 1990s, thereby extending their field of application. BMG of vastly different compositions have been produced, each with their own attractive properties such as excellent corrosion resistance, good mechanical properties, magnetic properties, or low friction coefficient [18, 19]. For example NASA is working on BMG gearboxes which would require neither lubrication nor heating – reducing the mass and energy consumption of future landers[1]. However, BMG are usually produced by casting or thermoplastic forming, which limits their maximum size (from millimetre to centimetre range) due to decreasing cooling rates and ensuing crystallisation, generally deteriorating the properties required for structural applications and tools [20]. AM has recently proved to be a game-changer for these innovative materials, as it has allowed them to sidestep the size limitations by building bit by bit, producing an amorphous item larger than possible through casting [11, 13, 21–23].

Consequently, the space industry can greatly benefit from both BMG and PBF-LB thanks to the doors their combination can unlock. This work proposes to explore this union specifically in this domain by manufacturing parts from bulk metallic glass powder in a process meant to work independently from gravitational environment, in the lab and onboard a sounding rocket. Additionally, this work purports to delve into the difficulties of PBF-LB such as the microstructural heterogeneities arising from the complex thermal history of various regions of the part/solidified melt-pool.

The thesis is arranged as follows. The conventional state of the art will be followed by an in-depth description of the experimental hardware, upon which the methods adopted to produce the research will be introduced, their results presented and discussed. Finally, the conclusions and outlook will be disclosed, and the inquisitive reader will find a collection of documents in the appendix.

---

[1] https://www.nasa.gov/stmd-game-changing-development/bulk-metallic-glass-gears/, last consulted 18.09.2024

Chapter 2

State of the Art

2.1 Zr-based BMG

The term *metallic glass* refers to a glassy alloy, i.e. an alloy that possesses an amorphous structure – with neither translational nor rotational symmetry – obtained by continuous cooling from the liquid state[1]. The first metallic glass (ca. 10 µm thick, over an area of 0.2 mm) was produced at a high cooling rate around $10^6\,\mathrm{K\,s^{-1}}$) by rapid quenching from the liquid state by spat cooling, and it rapidly started to decompose [25]. Later, metallic glasses were produced as micron-thick ribbons by quenching on a spinning casting wheel or by splat-cooling. Over time, the critical size limiting the production of an amorphous structure increased and today's metallic glasses are usually produced by casting. The *bulk* adjective applies to a metallic glass if its cast section thickness exceeds 1 mm. Though in theory all alloys can be "frozen" into a glass, BMG do not require as high cooling rates for this as typical crystalline alloys. Indeed, the cooling rate required to avoid crystallisation for a BMG can reach below $1\,\mathrm{K\,s^{-1}}$ while for a reluctant glass former it increases to $10^4\,\mathrm{K\,s^{-1}}$, and 10^{10}–$10^{12}\,\mathrm{K\,s^{-1}}$ for pure metals [24, 26, 27]. This slow cooling rate is made possible by choosing a composition which fulfils certain criteria (though exceptions to every rule exist): it is generally a multi-component composition that possesses sluggish dynamics / low diffusivity, a low melting point, and is near a eutectic composition [24, 28]. Beyond these criteria, a vast array of parameters based on transition temperatures, structural and topological models was developed by as many authors, but none so far seem to apply perfectly to *all* BMG [24]. Their evaluation is beyond the scope of this section.

A liquid alloy "freezes" to a glassy solid through the *glass-transition* as the temperature is decreased. This is not a thermodynamic transition but rather an arresting of flow through a strong increase in viscosity. The ease

---

[1] The more general term *amorphous* can refer to parts produced by vapour deposition or mechanical alloying for example [24].

with which an alloy follows this development is called the Glass-Forming Ability (GFA). It is often represented graphically by the Time-Temperature Transformation (TTT) diagram shown in fig. 2.1, where the C-shaped curve (or “nose”) represents the time necessary to form the crystalline phase and is shaped – as temperature is decreased – by the competing effects of an increasing driving force for nucleation and a decreasing atom diffusivity [24, 26, 27, 29, 30]. The critical cooling rate R_c is then the slowest rate at which the material will solidify without forming a crystalline structure. The process is described by various temperatures – T_g the glass-transition temperature, T_x the crystallisation temperature (at a given cooling/heating rate), and T_l the liquidus temperature. These quantities are then combined into complex temperatures – $\Delta T_x = T_x - T_g$ the super-cooled liquid region, $\Delta T(T) = T_l - T$ the undercooling, $T_{rg} = \frac{T_g}{T_l}$ the reduced glass transition temperature[2]. R_c is related to the critical casting thickness one can attain with a given composition. The greater the thickness, the slower the cooling rate at the centre of the cast. The first experimentally determined TTT-diagram for an alloy was achieved by Kim *et al.* using the containerless electrostatic levitation technique [31].

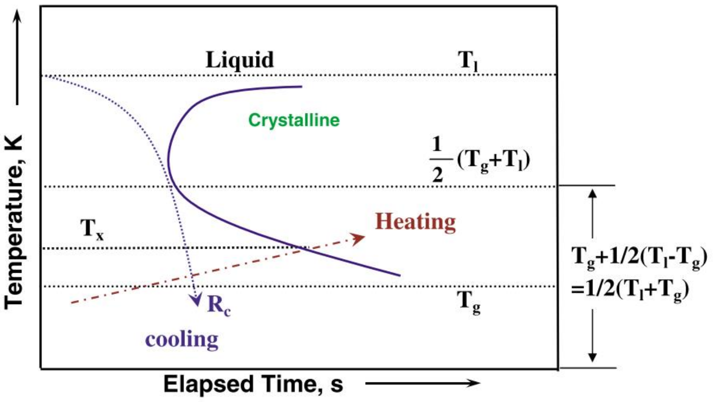

Figure 2.1: Schematic representation of a TTT diagram [29].

As shown in fig. 2.2 on the next page, the GFA depends on the stability of the liquid phases and their resistance to crystallisation. This can be framed as a reduced desire as well as ability to crystallise. This explains why eutectic compositions preferentially form glasses [32]: the alloy remains liquid at lower temperatures compared to off-eutectic compositions, and the energy difference between the crystalline and liquid phases is lower. Furthermore, using a multi-component alloy means that several crystalline phases compete for existence and can frustrate each other, rendering crystallisation more

---

[2] The ratio $\frac{T_g}{T_m}$ is often interchangeably used in the literature though it was found to correlate less well with the GFA or critical cooling rate of glasses [28].

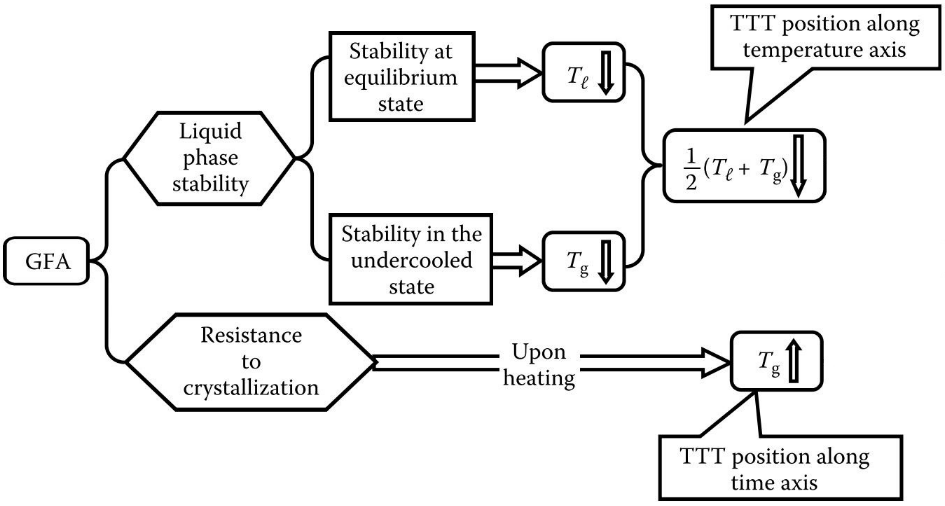

Figure 2.2: Schematic representation of the different factors at play in the GFA (modified from [24] itself from [30]). TTT refers to the time-temperature-transformation curve, as shown in fig. 2.1 on the preceding page.

difficult [24, 27, 33] (however, it seems that for some *bulk* metallic glasses, off-eutectic compositions can be more successful than their eutectic relatives [24, 34]). Factors influencing GFA include what Louzguine–Luzgin *et al.* separate into two categories: *intrinsic* factors concern homogeneous nucleation and refer to aspects inherent to the alloy composition (the thermal quantities described above, heat capacity, thermal diffusivity and expansion, etc.), while *extrinsic* factors appertain to heterogeneous nucleation (impurities in the melt, container defects and contamination, but also turbulence during solidification) [35].

In terms of AM, *Zr-based* BMG are the most intensively studied, as they are usually cheaper than those based on precious metals, thereby more appealing to the industry, while having a better GFA than glasses based on Fe, Al, Ni and Cu [36]. Additionally, they are attractive due to their mechanical properties [37–39]. They show promise also for space applications as cutting tools [40]. In this work, powders of two different chemical compositions specially developed to form bulk metallic glass parts are used: AMLOY-Zr01 and AMLOY-Zr02, both produced by Heraeus AMLOY Technologies GmbH (see manufacturer's data in appendix A on page 98).

The composition for AMLOY-Zr01 (formerly AMZ4) was developed by Heinrich *et al.* [41]. It evolved from the composition of Vit106a ($Zr_{58.5}Cu_{15.6}$-$Ni_{12.8}Al_{10.3}Nb_{2.8}$, at-%), a Be-free Zr-based alloy known for its excellent GFA [42]. The purpose of AMLOY-Zr01 is a simplification of the production and reduction of its cost by using an industrial grade Zr-Nb-prealloy and substituting Ni for Cu [41], so that its nominal composition is $Zr_{59.3}Cu_{28.8}Al_{10.4}Nb_{1.5}$, at-%. Because of the use of the pre-alloy, it also contains impurities: *"oxygen content up to 10300 ppm, H impurity of up to 4540 ppm, N of up to 1630 ppm, C of up to 3810 ppm as well as Fe and Cr of up to 3280 ppm"* [41]. However, this does not stop it from possessing good GFA [21, 41].

The composition of AMLOY-Zr02 is based on the Vit105 alloy ($Zr_{52,5}$-$Cu_{17,9}Ni_{14,6}Al_{10}Ti_5$, at-%) developed at the California Institute of Technology in 1997 [43]. It is one of the Zr-based glass-formers with highest GFA.

2.2 PBF-LB

The process used in this work is part of the family of AM. ISO/ASTM 52900:2021(en) gives the definition of AM as "a process of joining materials to make parts from three dimensional (3D) model data, usually layer upon layer, as opposed to subtractive manufacturing methodologies" [44]. AM can be used with polymers [16, 17], ceramics [14, 15], metals [10–13], or as composites [45–48]. AM of metals can be done in varying ways. For example, wire feed systems rely on the use of wire as feedstock being directly delivered and melted where the part should be built [49, 50], while powder feed systems use powder as feedstock, with the powder being applied and melted directly where the part is meant to be [51]. Powder bed systems also rely on powder as feedstock, however the part is built by applying a layer of powder on the whole surface of the build-platform and selectively melting the powder in the required configuration, after which a new layer is applied and selectively melted, and so on and so forth until a 3D part is obtained [22, 45, 52–54]. Other less commonly used methods rely on slurries [14, 55, 56]. Each of these techniques have advantages and disadvantages. In the case of powder and wire feed, the amount of feedstock used during the process is the same as – or close to – what is being applied, whereas the powder bed system requires – as the name indicates – a complete powder bed: the horizontal dimensions of the bed are independent of the size of the part to build. Feedstock recycling is therefore of greater importance for powder bed systems. On the other hand, powder bed systems allow the production of several parts simultaneously, as many as can fit on the built-platform. Additionally, they have the highest dimensional accuracy and are less likely to require post-processing of the built part [57]. These methods require an energy source to sinter or melt the feedstock. This can be an electron beam [12, 52, 58], a laser [54, 59–61], or an electric arc [62, 63]. According to the review by DebRoy *et al.* [57], electric arcs have very high energy so that using electric arcs leads to the shortest production times but also the lowest dimensional accuracy and therefore to more post-processing, while using lasers requires the longest production times but the highest dimensional accuracy, with less post-processing. Meanwhile, electron beams are generally situated in-between in terms of characteristics.

For the work performed here, a laser is used in combination with a powder bed so that the process is named Laser-based Powder Bed Fusion (PBF-LB). PBF-LB belongs to the most versatile metal AM processes thanks to its possible geometries and variable process parameters. The product of this process at any given time is schematically represented in fig. 2.3. A detailed model view of the laser-melting process is shown in fig. 2.4. The melt-pool or melt-track describes the melted and not yet solidified portion of material on and in the immediate vicinity of the laser beam path on the powder bed. For simplification, it can roughly be divided into zones: a depression zone at the laser spot dominated by the recoil force, a tail region near the end of the melt track dominated by surface tension, and a transition region between the two [66].

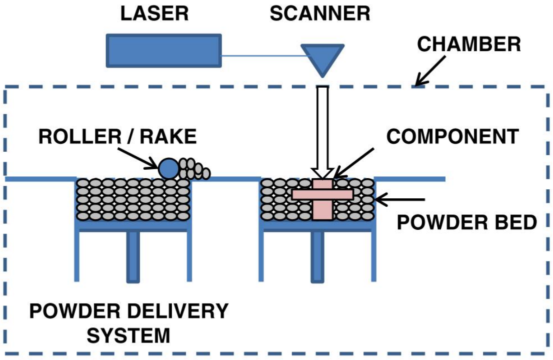

Figure 2.3: Schematic illustration of a possible AM powder bed system [64].

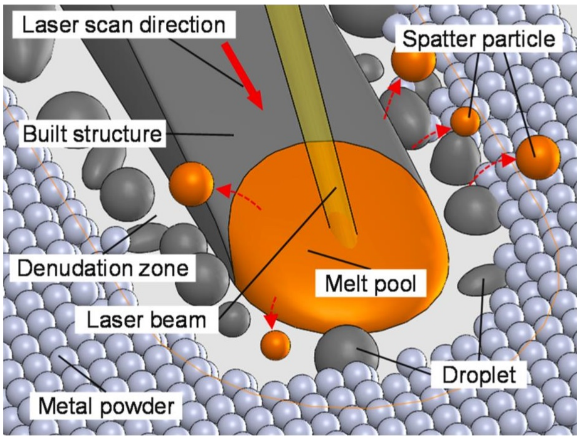

Figure 2.4: Model of the PBF-LB process with melt pool, spattered media, and powder denudation zone [65].

The beam melts a region larger than its own diameter and through Marangoni convection pulls the melt to the warmer regions, creating a zone around the melt-pool which is devoid of powder and matter, i.e. the denudation zone [65–68].

2.2.1 Process parameters

According to Rehme & Emmelmann [69], there are over 130 parameters potentially influencing the PBF-LB process, of which 13 would be crucial to the quality of the built part. These include laser beam characteristics (power, size, focus position), scanning characteristics (speed and laser path strategy), powder bed characteristics (flowability of the powder, temperature of the bed, thickness of each layer), and gas characteristics (pressure, composition, flow direction and intensity). Generally, and especially in the case of this work, the following settings can most easily be varied: laser output power, speed of the laser scanning, distance between neighbouring lines (called hatch or hatching distance), laser path, speed of powder layer deposition, thickness of the powder layer, and composition of the gas atmosphere. These are the parameters that will be addressed in this work. Which of these is most influential is open to active debate and research, but the literature mostly agrees that the following are the most significant with respect to the quality of the final part: laser power, laser scanning speed, and powder layer thickness [70–73]. Some of the parameters mentioned above are often combined to form overarching parameters.

Energy density is often introduced as a parameter that would provide a correlation between process parameters and quality of the final part. However, even the very definition of energy density (or energy input) is not as straightforward as one might first assume. There are various definitions provided in the literature:

A linear energy density in $\mathrm{J\,mm^{-1}}$ from [74] based on [75]:

$$E_l = \frac{P}{\sqrt{v}} \tag{2.1}$$

with P the laser power in W, so $\mathrm{J\,s^{-1}}$, and v the laser scanning speed in $\mathrm{mm\,s^{-1}}$. A surface energy density in $\mathrm{J\,mm^{-2}}$ [76]:

$$E_s = \frac{P}{v \times \sigma} \tag{2.2}$$

with σ the laser beam diameter. A volumetric energy density in $\mathrm{J\,mm^{-3}}$ [22, 59]:

$$\overline{E_V} \propto \frac{P}{v \times h \times S} \tag{2.3}$$

with h the powder layer thickness in mm and S the hatch spacing (or hatching distance) in mm. And a differently defined volumetric energy density [77]:

$$E_{V2} = \frac{P}{v \times \sigma \times h} \tag{2.4}$$

Most authors try to compare final part properties (mostly density, which is a defining feature in the evaluation of the final part quality, see section 2.3.1 on page 11) in relation with their definition of energy density. However, it has been shown that the correlation is far from obvious [70, 78–80]. If the energy density is too high, it can lead to keyhole mode (see below) and therefore gas porosity, while if it is too low, it can result in insufficient melting of the feedstock material, inducing lack of fusion porosity [66].

Conduction mode refers to when the energy is enough to melt the feedstock and heat the underlying matter by conduction for both parts to wet sufficiently to connect. The name for the keyhole mode refers to the depression appearing in the melt-pool due to vaporisation of the material and plasma formation in the laser beam and ensuing recoil pressure when the energy input is higher. This depression focuses the beam deeper into the material, enhancing laser absorption and making the melt-pool much deeper than in conduction mode (where a large part of the beam energy is reflected). This mode is however also more likely to cause spatter and trap bubbles in the final part when the cavity collapses [67, 75, 81, 82]. The difference is shown in cross-sections in fig. 2.5 and the advantages and disadvantages of each mode are described in table 2.1 on the next page.

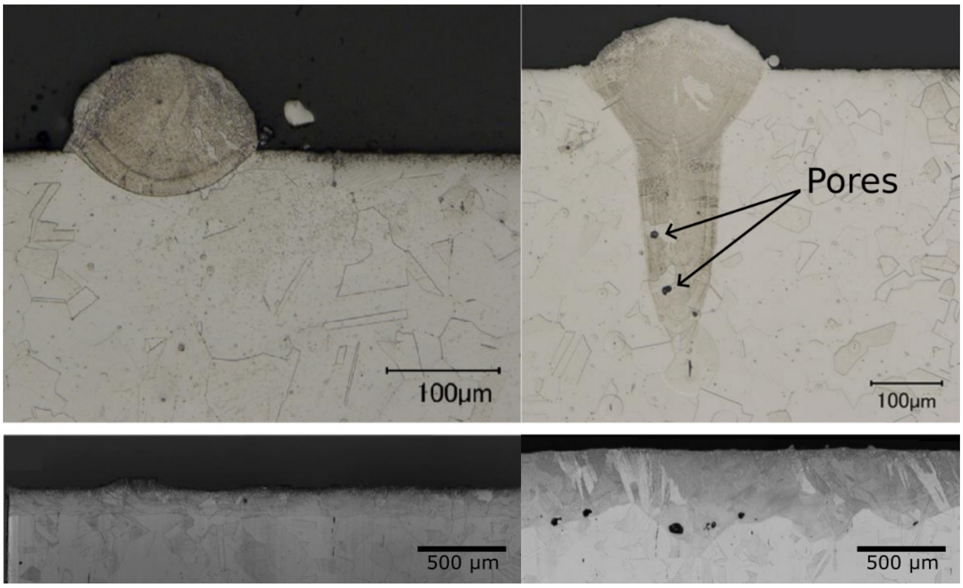

(a) (b)

Figure 2.5: Metallographic cross-sections of single-track experiments conducted in (a) conduction mode and (b) keyhole mode using stainless steel 1.4404 in PBF-LB. Pores are visible at the bottom of the solidified melt-pool in (b) and the track depth varies along its length. Adapted from [75].

Still another complication in the use of energy density rests on the changes in absorptivity of the laser energy depending on the phase within the process

Mode	**Conduction**	**Keyhole**
Advantages	Smoother melt-pool, less variation in melt-pool depth, less spatter, no pores from melt-pool collapse	Stronger bond to the substrate and matter below the new track
Disadvantages	Portion of the beam energy is reflected off the surface	More spatter, more pores within the material, less predictable track depth

Table 2.1: Advantages and disadvantages of conduction and keyhole mode

[83], so that the effective energy absorbed does not increase linearly with laser power: the (unmelted) powder bed has high absorptivity (and the smaller the grain size, the higher the absorptivity [84]), while the flat surface and surface coated by the melt reflect some amount of the energy and have comparable absorptivity values to each other, then the absorptivity increases again in keyhole mode.

It has also been shown that the higher the energy density, the lower the chemical homogeneity in the melt due to the Marangoni convection, leading to local microstructural heterogeneities [22]. Additionally, the higher the energy density, the larger the cooling rate within the melt-pool, and the higher the resulting residual strains [85]. The inadequacy of the energy density to determine the optimal settings is assumed to be due to these various quantities not taking into account the threshold from conduction to keyhole mode as well as taking scanning strategy into account only in a limited way (such as in eq. (2.3) on page 8 which uses hatch spacing) or not at all. In the following, we will use energy density following eq. (2.3), i.e. only to describe the proportionality between energy density, power, and inverse speed, layer thickness and hatch distance.

Scanning strategy is another broad parameter which includes the order and direction in which the lines required to fill a layer are built, and how these change over subsequent layers (see fig. 2.6 on the next page). Scanning strategy greatly influences residual stress distributions in the produced part [70, 86, 87].

2.3 Potential/typical defects

In this section we will focus on the defects most discussed in the literature on PBF-LB: porosity, cracking, surface roughness, and microstructural heterogeneity. Though the first three apply equally well to crystalline and glassy materials, for the fourth we will focus on glassy alloys.

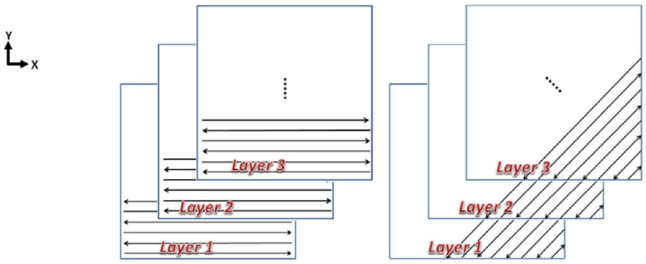

(a) Line scanning (b) 45° line scanning

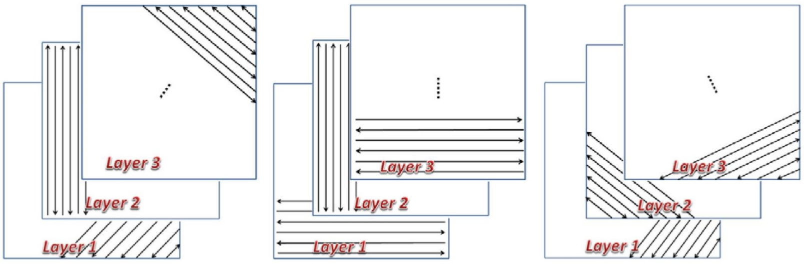

(c) 45° rotate scanning (d) 90° rotate scanning (e) 67° rotate scanning

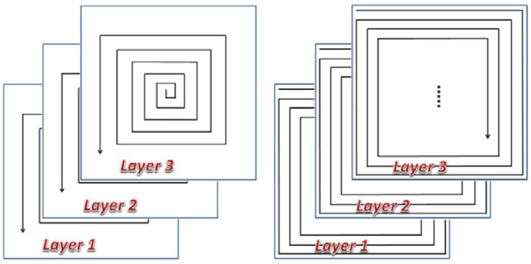

(f) In-out scanning (g) Out-in scanning

Figure 2.6: Different scanning strategy possibilities, adapted from [87].

2.3.1 Porosity and lack of fusion defects

Pore formation has been of great concern for PBF-LB as pores can very strongly affect the mechanical properties of the final part by acting as stress concentrators [54, 88, 89]. The morphology of the pores helps distinguish their origin [52, 90]. Spherical pores, usually a few µm in size, are usually gas inclusions in the bulk. They either already exist in the powder (see example in fig. 2.7 on the following page) due to the powder atomisation process, or are from process atmosphere trapped in the bulk during the melting, such as during keyhole mode melting [57, 67, 75, 91] as shown in fig. 2.5 on page 9. On the other hand, non-spherical (usually acicular) pores tend to appear between layers or between lines, and seem to stem from a lack of fusion and lack of adherence between layers or between lines within a layer because of a lack of powder/matter resulting from the denudation zone [57, 92] represented in fig. 2.4 on page 7. There pores are generally larger than 10 µm (equivalent diameter), and act as stress concentrators because of their shape [57, 93]. Lastly, surface porosity which describes the presence of pores at the surface arising due to Marangoni convection, coalescence and possible collapse of bubbles in the melt [91] as shown in fig. 2.8.

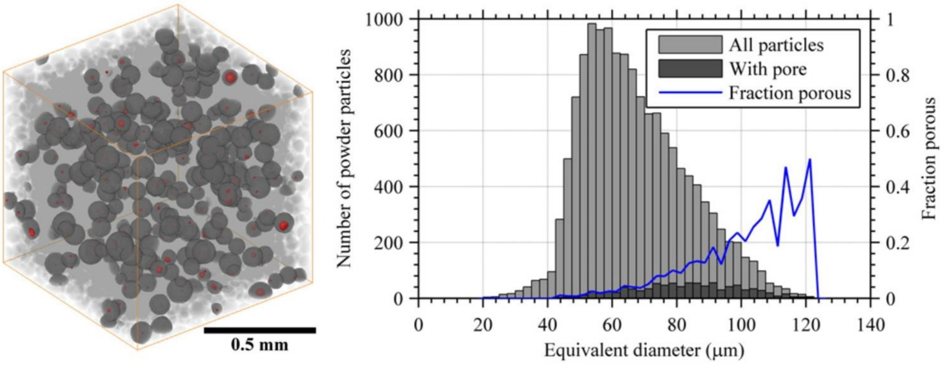

(a) *(b)*

Figure 2.7: (a) Computer Tomography (CT) image revealing gas-pore-containing Ti–6Al–4V powder particles (pores in red) and (b) size distributions of all the particles versus the particles containing porosity with the fraction of particles containing pores for each size range [90]. The equivalent spherical diameter refers to the diameter of a sphere of the same volume as a given particle, as it is not necessarily spherical.

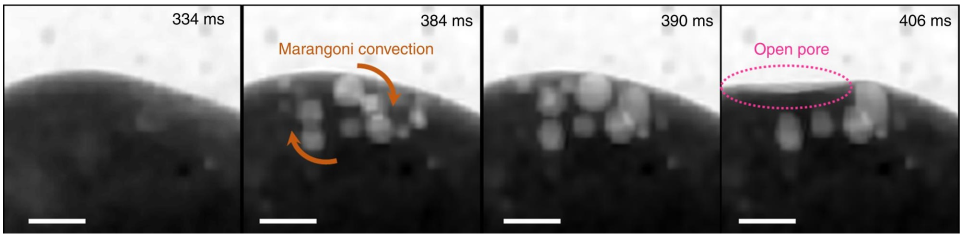

Figure 2.8: Time-series radiographs made during PBF-LB near the front of a melt-pool, scale bars represent 250 µm. *Some pores are seen to nucleate, coalesce and collapse, resulting in an open pore. Taken from [91], which also provides the supplementary videos from which these images are extracted (and they're great to watch!).*

2.3.2 Cracking

In their review, DebRoy *et al.* [57] describe three types of cracking: solidification cracking which occurs at grain boundaries within the build when the tensile stress generated in the solidifying layer exceeds the material's yield strength, liquation cracking which is observed in the mushy or partially melted zone, and layer delamination (where the part cracks into or along layers or detaches from the build-platform) which is caused by residual stress. Residual stress is defined as Withers & Bhadeshia as "that which remains in a body that is stationary and at equilibrium with its surroundings" [94]. It is a common issue for additively manufactured parts and a big impediment to their widespread application [87]. During the PBF-LB process, large temperature gradients are at play: firstly, because of the very rapid heating of the surface around the laser spot and secondly, because of the cooling, solidification, and shrinkage of the latest layer which leads to tensile stress in that layer, but compressive stress in the layers or substrate below [86]. An interesting aspect is that the more porous, i.e. less dense, the material, the lower the level of distortions due to residual stresses, as pores seem to help relax these by compensating for material shrinkage [70, 95]. Nonetheless, producing fully dense parts is critical for the broader use of additively manufactured parts due to the impact of pores as stress concentrators on the mechanical properties.

2.3.3 Surface roughness

Surface quality is an important aspect of PBF-LB, as the roughness of a given layer determines the local thickness of the next powder layer being spread over it. Though surface roughness due to step effect in 3D parts is an non-negligible issue for PBF-LB, here we will focus on the quality of flat horizontal/top surfaces. Variations can lead to stark localised differences in quantities of remelted material, but also to the portion of laser intensity being reflected off the surface [96] and therefore to differences in local temperature and local microstructural properties. Both the choice of feedstock material and building parameters can lead to increased surface roughness.

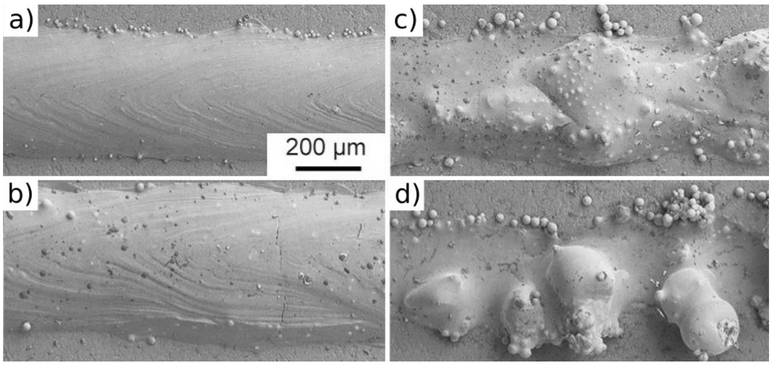

Figure 2.9: Effect of Tungsten powder grain size on the aspect of a single track. (a) $D_{50} = 5.7\,\mu\text{m}$*, (b)* $D_{50} = 22.47\,\mu\text{m}$*, (c)* $D_{50} = 37.26\,\mu\text{m}$*, and (d)* $D_{50} = 47.63\,\mu\text{m}$*. Adapted from [84].*

As seen in fig. 2.9, increasing the grain size can lead to increased surface roughness [57, 84]. This is understood to be due to an increase of the portion of unmelted powder for a given laser power, as well as a less stable melted track [84].

Surface roughness caused by laser power and scanning speed can also be described as arising from insufficiently melted powder, or from balling which in the literature refers either to small balls of solidified material remaining on the edges of a built track [97] or to the melted material solidifying into spheres instead of a line [52, 57, 98, 99]. These effects are dependent on those building parameters [52, 54, 100] as shown for example with stainless steel 1.4404 powder in fig. 2.10.

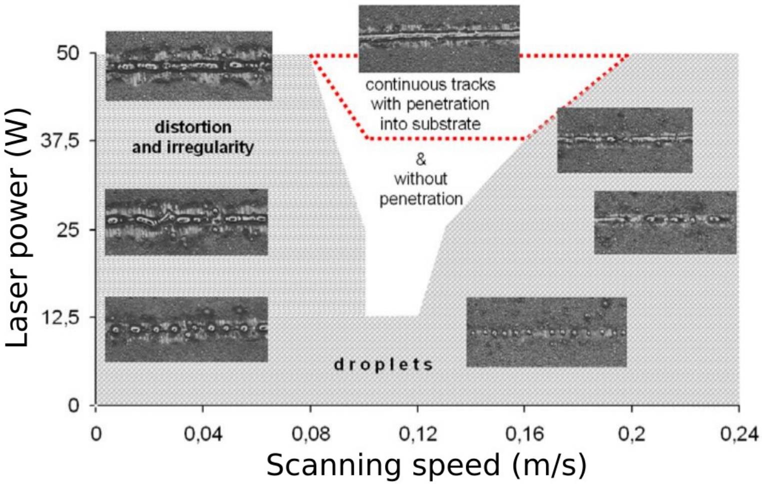

Figure 2.10: Process map for a single track of the first layer of stainless steel 1.4404 powder with layer thickness equal to 50 µm*, from [54].*

In the case of balling – the melt pool/track separating into spheres, this is described as being due to Plateau-Rayleigh instability: balling is predicted when the melt-pool length to diameter ratio is greater than π [57, 98]. The melt-pool is assumed to be cylindrical, but one can imagine the melt-pool to be flatter than a cylinder and therefore to have a smaller equivalent “real” diameter, lowering the required pool length to fit within the prediction. Though the physical foundation for Plateau-Rayleigh instability can be seen as surface tension, this is not an easy parameter to deal with when optimising process variables. Empirically and in a more generalising fashion however, when recalling the various definitions of energy density in section 2.2.1 and putting these in parallel with increasing melt-pool temperature leading to lower surface tension as well as comparing with the process map shown in fig. 2.10, one can deduce that increasing the speed, increasing the layer thickness, or lowering the laser power leads to lower energy densities and average melt-pool temperature, increasing the surface tension and therefore leading to increased balling.

Another phenomenon detrimental to surface quality is spatter, which describes either liquid or solid metal ejected from the laser spot and its direct environment and which lands on the surrounding powder or already solidified matter. Spatter was thought to be caused by laser-induced recoil pressure, however evidence from high-speed imaging on PBF-LB of stainless steel 1.4404 by Ly *et al.* seems to show that it occurs mostly from *"vapour-driven entrainment of micro-particles by the ambient gas flow"* [101]. The authors concluded that while some spatter was indeed caused by recoil pressure, it amounted to only 15% of the spatter compared to 60% being due to hot ejections from entrainment. Meanwhile the work of Nakamura *et al.* [102] with high-speed camera observation of keyhole-mode in the welding process of pure titanium points to the dependence of the main spatter origin on the scanning speed (at constant laser power): high speeds led to most of the spatter originating from the molten pool just behind the keyhole, while low speeds meant that it came from the front or sides of the keyhole [102]. Because of their reactive nature, these droplets or high-temperature particles are prone to oxidation and can thereby contaminate the powder bed [103, 104], whilst leading to greater process-induced porosity [105]. As they are often of larger sizes than the unprocessed powder particles, they locally increase the powder layer height [104], thus changing the optimal energy necessary for the process (according to the equations in section 2.2.1).

This vapour entrainment is parenthetically also responsible for extended denudation zones around the laser beam spot and the melt-pool [92], contributing to the lack-of-matter pores mentioned previously in section 2.3.1.

2.3.4 Microstructural heterogeneities

As mentioned, BMG are traditionally produced by casting, which sets a size limitation of the final part depending on the GFA and therefore the critical cooling rate required to vitrify the alloy. AM was found to circumvent this rather limiting factor by demonstrating that, by building layer upon glassy layer, one could produce a glassy alloy larger than by casting [21, 106–109]. However, it is not as straightforward as one might hope. Generally, AM parts experience during their creation/production repeated melting and rapid solidification, and typically go through several solid state transformations, making the process more complex than conventional manufacturing processes [52, 64, 93]. As mentioned in section 2.2.1 on page 8, high energy density can lead to chemical heterogeneity / element segregation in the melt-pool and therefore the final part. While this might mostly result in texture and anisotropic mechanical properties for crystalline alloys [57, 93, 110], it is particularly detrimental to BMG as these materials are metastable and rely on very precise compositions in a way that local segregation may lower their local GFA and cause them to crystallise [22]. Furthermore, when adding a new layer, the previous one will (partly) experience an increase in temperature. Returning to the TTT-curve in fig. 2.1 on page 4: it is usually used for examination of the behaviour upon cooling, but it is important to note that the behaviour upon heating can differ from that at cooling [111] and that this is especially relevant for BMG in AM. Indeed, the temperature at which nucleation reaches its maximum is below that at which crystal growth is highest [26]. This means that when a new line is added and the previous layer (and neighbouring line) experiences heating (as shown in fig. 2.11a), heat-affected zones may therefore form nuclei, and these will grow if more heat is provided to them, as seen in fig. 2.11b. Therefore the cooling rate is not the only deciding factor in the glass-forming ability of additively manufactured BMG parts, but the (re)heating rate also [112]. If the heat is enough to melt these affected zones, then the cooling rate is once again relevant. In this case, the scanning speed (and heat dissipation) have to be quick enough to reach a cooling rate greater than R_c.

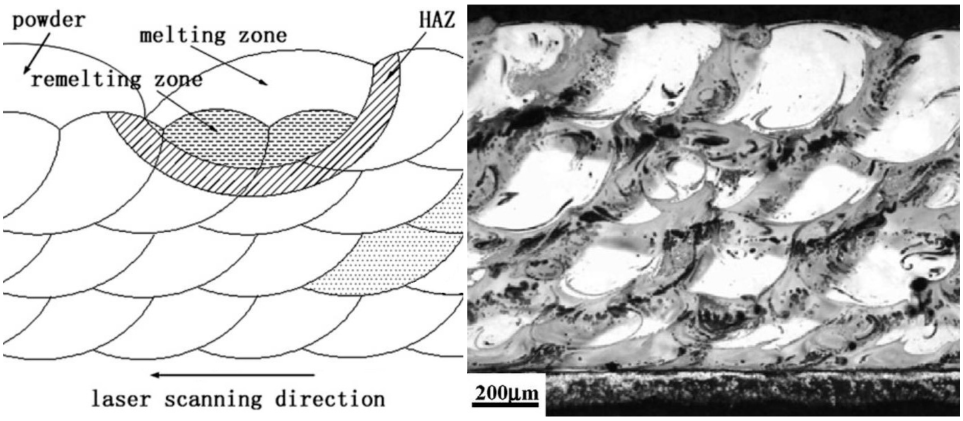

(a) *(b)*

Figure 2.11: (a) Schematic representation of the PBF-LB process and the heat-affected zone, adapted from [60]. (b) Optical microscopy of a $Zr_{55}Cu_{30}Al_{10}Ni_5$ BMG built over five layers showing crystallisation in the heat-affected zones described in the left image, adapted from [113].

Another common issue with PBF-LB of BMG is oxygen contamination. Because the feedstock is in powder form (high surface to volume ratio), it is more likely to take oxygen in as surface oxides [23]. Indeed, the oxygen content was determined by Marattukalam *et al.* to be circa 1 at-% (0.2% by weight) in AMLOY-Zr01 when produced by inert gas fusion [106]. In BMG, this oxygen contamination is found to induce lower GFA and therefore increased crystallisation [41, 106, 114–117]. Oxygen contamination is also found to affect melt properties such as viscosity and surface tension [98]. These would then affect the behaviour of the melt during the process.

2.4 Powder handling in microgravity

In PBF-LB a powder is spread over a build-platform and a laser melts the powder layer in the configuration required to create the desired part. The layer deposition usually relies on gravitational forces. However, in space or on satellites, these reduced or absent gravitational forces must be compensated for. The key feature of PBF-LB in space, therefore, is the powder handling and stabilisation in weightlessness. To achieve this, the Gas Flow Assisted Powder Deposition developed by the Bundesanstalt für Materialforschung und -prüfung (BAM) [4] was used and expanded to fit the current platform (the original system developed by the BAM was designed and built for parabolic flight). This deposition system relies – as the name indicates – on gas to stabilise the powder layer (see fig. 2.12a).

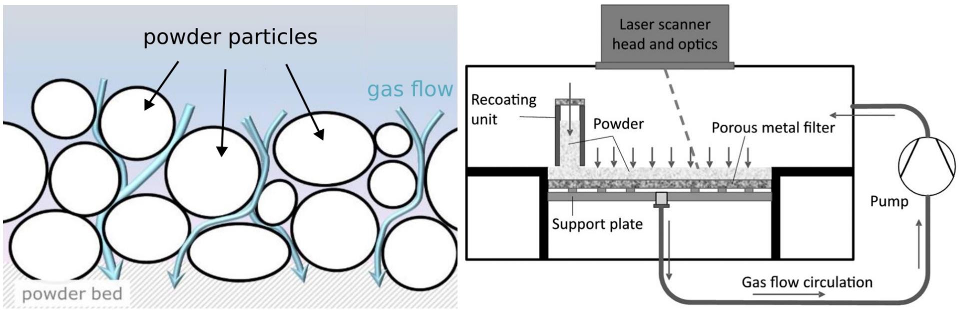

(a) (b)

Figure 2.12: (a) Physical basis for the gas-flow assisted deposition, adapted from [2]. (b) Gas-flow assisted powder deposition as developed by Zocca et al. *and using the phenomenon described in (a).*

This is done by using a porous build-platform and establishing a gas flow though the powder bed and this platform. This modified build-platform acts as a filter for the powder particles under the force of a vacuum pump below the platform. A schematic representation of the setup is presented in fig. 2.12b. This design was successfully tested during DLR and ESA zero-g parabolic flight campaigns [4].

Chapter 3

Experimental hardware

3.1 Microgravity experiments

The experiments described in this thesis were performed using MARS-M (Multi-material Additive manufacturing for Research in Space), a payload developed to fit onboard the MAterialPHysikalische Experimente Unter Schwerelosigkeit (MAPHEUS) sounding rocket.

3.1.1 Microgravity experimentation platforms

When it comes to performing tests in microgravity, several options are available and the afforded microgravity durations as well each methods' ease of access vary.

A drop tower provides a relatively cheap alternative to space laboratories for conducting short (less than ten seconds long) experiments under microgravity conditions. As the name indicates, it relies on a tower containing a drop tube, the height of which determines the free-fall time. The tube is evacuated to 1 Pa to reduce air drag in order to approach microgravity conditions [118]. It is relatively easy to obtain experimental time and the time between experiments is the shortest of all options.

Parabolic flights rely on planes to perform short-term (around twenty seconds long) experiments under microgravity conditions. The aircraft follows a parabolic trajectory, starting from horizontal flight with a hypergravity phase (pull-up) followed by a microgravity phase (parabolic ballistic free-fall) and another hypergravity phase (pull-out) back to horizontal flight. Several such parabolae are performed per campaign day. These flights are often used to qualify and validate experiments destined for prolonged microgravity experiments, such as on a sounding rocket or a satellite [119, 120]. This was the case for MARS-M, which was tested during parabolic flights for calibration of gas flow and powder recoating speed [1]. After this first set of qualifications, the device was successfully qualified during environmental testing under vacuum conditions and ready to be used onboard the MAPHEUS sounding rocket.

Sounding rockets are unmanned rockets (in some cases repurposed military rockets) travelling on a suborbital trajectory to perform measurements or experiments in microgravity in high atmosphere [121]. The experiment time offered can reach up to 13 min. They are a flexible and cost-effective platform to perform research in space. Since the MAPHEUS-1 rocket was launched in May 2009, these sounding rockets' capabilities have increased. Launched from the Esrange Space Centre in Jukkasjärvi, Sweden, the rockets used for experiments during this work are circa 12 m long and offer microgravity durations around 6.5 min on a suborbital flight with an apogee around 260 km. Residual acceleration levels are measured to be as low as 10^{-4} to 10^{-6} g. A bi-directional data communication interface and a live video downlink are supplied to the scientific payload by MAPHEUS payload support systems by DLR's Mobile Rocket Base [122–124], thus allowing the operators at the ground station to oversee the automated manufacturing process live and use telecommand to intervene in the process if required.

The platforms offering the longest microgravity times are satellites, whether manned like the International Space Station (with its Materials Science Laboratory [125]) or unmanned, but these are much harder to access and qualify for. Therefore, sounding rockets were the selected platform.

3.1.2 Campaigns onboard MAPHEUS

The MARS-M payload was flown onboard the MAPHEUS-11 (M11), M10, and M9 rockets which were launched in May 2021, November 2021, and January 2022, respectively, from the Esrange Space Centre in Jukkasjärvi, Sweden. The flight characteristics are given in table 3.1.

The brief time between launches – especially considering payload and equipment transportation time to and from the Space Centre by road – permitted neither big improvements in the MARS-M hardware nor much testing at the institute. Additionally, work on site was made more complicated by the COVID-19 pandemic and team-members not being permitted to work in the same room at the same time for several days upon arrival for fear of infection prior to travelling to Sweden. Pre-flight testing was performed mostly on-site in the few – but intense – days before countdown. In the case of M10, extreme temperatures (−28 °C) and the presence of biological samples

Campaign	**Apogee (km)**	**Microgravity time (s)**
M11	221	345
M10	259	370
M9	254	358

Table 3.1: Apogee and µg-time data for the different launches [1].

onboard the payload made special care necessary: heating was installed in the launch-building and the rocket was covered in thermal insulation material, as shown in fig. 3.1, left.

Figure 3.1: Left: M10 rocket on launch ramp with insulation. Right: M11 rocket launch [1].

3.2 MARS-M

The contents of this chapter were published by Neumann *et al.* [1]. MARS-M and its modifications were designed and constructed by Dr. Christian Neumann and Mr. Johannes Thore of the Institute for Materials Physics in Space, DLR.

3.2.1 Design criteria

In order to function aboard the MAPHEUS sounding rocket, MARS-M had to fulfil several strict criteria, most notably concerning autonomy, environment, and accessibility.

The first environmental criteria are given by the dimensions and motion of the rocket itself: the device should not exceed a certain mass and size, while it must also be able to resist the rocket launch induced dynamic loads and vibrations. Furthermore, the device must be able to function in vacuum and microgravity during the flight. As most items making up the device are off-the-shelf, they are not designed to function under these conditions, and therefore require some adaptations. The powder stabilisation must also be mastered under microgravity conditions.

Accessibility criteria refer firstly to the possibility of accessing the device and especially the powder container and build-platform once they are integrated into the rocket on the launcher, and secondly to the requirement for data communication and potential process interruption between the device and the user at the ground station before and during the flight.

Lastly, in order to be fully autonomous, the device requires a hermetically sealed process chamber and an own energy source powerful enough to build a part without user intervention.

3.2.2 Payload description

MARS-M is presented in fig. 3.2. It measures 700 mm in height, 438 mm in diameter, and weighs 44 kg not counting the rocket payload's outer structure of 12 kg. As per the aforementioned criteria, MARS-M possesses [1]:

- a PBF-LB unit including powder stabilisation
- data acquisition and handling
- control computing
- a electrical power supply

The manufacturing process is integrated to MAPHEUS payload support systems and the ground station according to the schematic in fig. 3.3.

3.2.3 Experiment chamber and gas flow

Inside the payload, the PBF-LB process in MARS-M requires a hermetically closed experiment chamber to not only guarantee a constant pressure during the entire flight but also to ensure a low oxygen atmosphere during the manufacturing. Because of the flushing of the chamber with the chosen gas composition and of the experienced inside over-pressure when in space, the processing chamber is built to resist differences of up to 2 bar of differing pressure between the outside and the inside.

The manufacturing process itself takes place in a removable cartridge which the user can access through a hatch. As shown in fig. 3.4, the cartridge contains the build-platform, the powder container, and the E- and Z-axes. Thanks to the ease of access, the user can conveniently/efficiently exchange the build-platform, powder, or the whole cartridge before lift-off while MARS-M is joined in the payload.

In weightlessness, the gas flow-assisted powder deposition described in 2.4 is used in order to stabilise the powder in the powder bed on the build-platform and at the same time to enable it to flow during recoating. To achieve this, under-pressure is generated below the build-platform by attaching a hose to its mounting adapter, inducing a gas flow perpendicularly

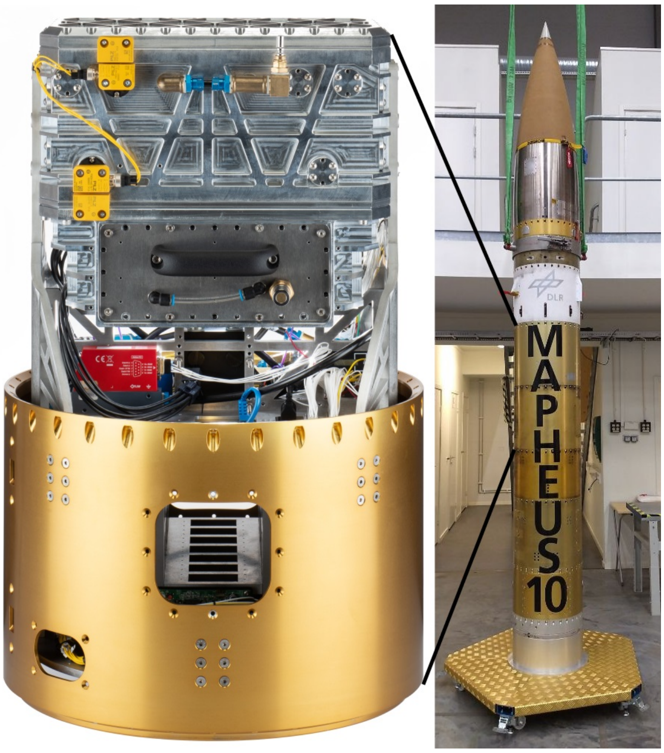

Figure 3.2: MARS-M (left) integrated into the MAPHEUS-10 scientific payload (right)[1].

to its surface. As the build-platform is porous, the powder particles are pushed towards it by the gas flow. Beyond the cartridge, the gas flow moves through several 10 µm pore sized particle filters and a mass flow sensor (Red-Y series, Vögtlin Instruments GmbH) and into two type 3111.610 (Boxer GmbH) diaphragm pumps which are installed inside the chamber to avoid pressure differences, while the filters and flow sensor are located outside the experiment chamber. The pump outlet is led back into the chamber and left open.

3.2.4 Motion mechanics

In addition to providing laser scanning, powder layer application, and build-platform displacement, the device must withstand the various static and dynamic loads experienced during the flight. For this to be possible, the following mechanical set-up was chosen [1]:

- a cartesian assembly of X- and Y-axes moves a focused laser spot parallel to the build-platform, using Ø 8 mm carbon-reinforced polymer and hard-anodized aluminium shafts, a stepper drive and a timing belt, as well as self-lubricating dry-running polymer bearings so that powder

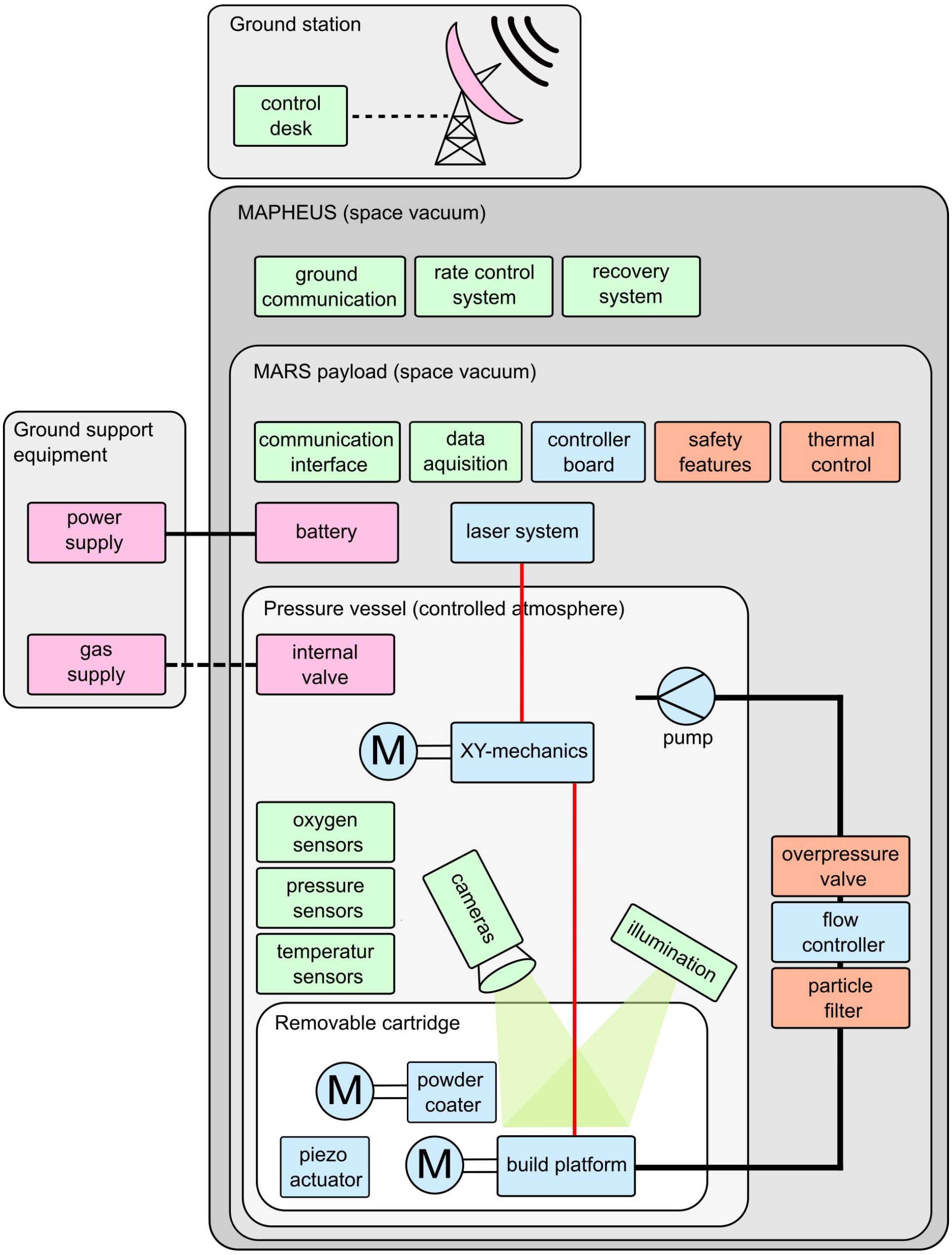

Figure 3.3: Schematic overview of MARS-M integration within the MAPHEUS rocket as well as the communications and Ground support [1].

particles will not stick nor block movements. The Y-axis moves the X-axis which bears the fibre-coupled laser optics.

- a vertical Z-axis moves the build-platform up or down (see fig. 3.4) thanks to three fine-thread shafts synchronised by a timing belt and

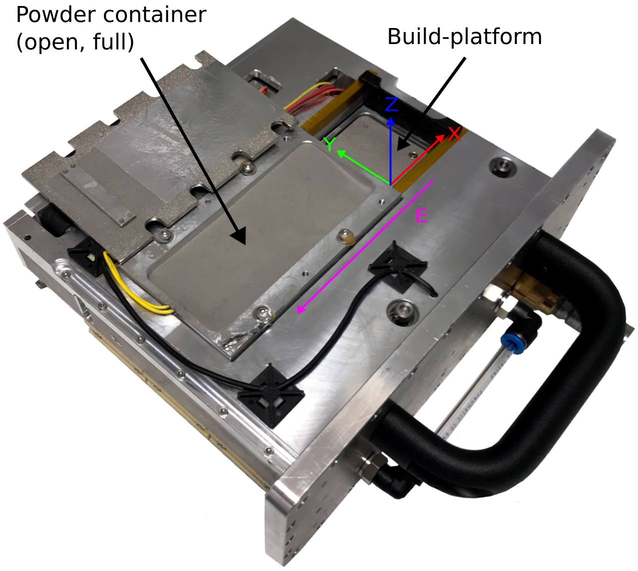

Figure 3.4: Insert bearing the build-platform (without powder in this image) and the powder container. The X-, Y-, Z-, and E-axes are shown. The X- and Y-axes are parallel to the build-platform, so that the Z-axis is perpendicular to it. The platform is carried below the powder container along the E-axis to apply each new powder layer [1].

driven by stepper drives.

- an additional E-axis – oriented parallel to the X-axis – is responsible for powder recoating (see fig. 3.4), and uses similar components to the X and Y-axes, with two threaded shafts and a timing belt.

All axes possess optical end switches.

3.2.5 Laser system

Like the rest of MARS-M, the laser system must withstand the forces experienced during the flight and must additionally possess a cooling system independent of air convection. The laser system is built of [1]:

- a laser diode bar module (type Coherent IS58, with max. 283 W optical power at centre wavelength of 976 nm into a 100 µm fibre core),
- a laser diode driver MESSTEC type MSM 100-25,
- laser optics from standard C-mount lens adapters, a SMA-type fibre adapter, and plano-convex $\lambda/10$ grade uncoated Fused Silica lenses,
- a temperature sensor to detect overheating,

- a cooling system in which the excess heat is alleviated via a cooling liquid loop connected to a custom-built heat sink made of finned pipes and Rubitherm RT28 HC, a phase change material.

Thanks to this heat sink, the laser can be used in vacuum at full power for 10 min, by far exceeding the available microgravity time. When experimenting in the lab, an external cooling system is used to allow for longer laser operation.

3.2.6 Process control

The stepper drives for the X-, Y-, Z-, and E-axes, their end stops and position switches, as well as the laser power are controlled via a user interface by a Smoothieboard 5XC V1.1 (open hardware project Smoothieware.org). This controller board allows to automate several of the subprocesses required for the manufacturing, thereby making the whole process smoother. Furthermore, the set point for laser power, gas flow, and the piezo-actuator are output as pulse width modulated signals to digital output pins. Additional digital in- and output pins are used to communicate individual events to and from the data recorder. The hardware required modification to resist launch loads and environmental vacuum. The board runs the latest firmware version, adapted to the device by editing the configuration file only. Individual commands are listed in appendix B on page 101.

3.2.7 Build-platform and layer application

As mentioned above, MARS-M was tested in microgravity during parabolic flights for calibration of gas flow and powder recoating speed before flying onboard MAPHEUS [1]. This was done during 62 parabolas over two separate days on a Novespace Zero-G aircraft (circa 20 s of microgravity per parabola). Because of the short microgravity times, only the powder handling procedure and control algorithm were calibrated during the parabola. After each flight the powder bed was investigated. From these experiments, suitable gas flow settings were chosen and applied to later lab experiments and sounding rocket flights. With the current calibration, spreading a new powder layer requires 15 s.

As previously mentioned, the MAPHEUS sounding rocket offers approximately 6.5 min of microgravity, which is long compared to other platforms and enough to serve as proof of feasibility, but still short in terms of typical PBF-LB process: the time permits to spread and laser-melt circa 8 layers of powder on a platform of dimensions 45 mm × 45 mm machined from a 5 mm-thick porous sintered plate (pore size: 8 µm) of stainless steel 1.4404.

In order to apply a layer of powder to the platform, the following sequence is applied [1] (the gas flow is active through the build-platform at all times during the sequence, and increases in importance as the gravity decreases):

1. in case of first layers, the Z-axis is “homed”– which refers to moving the axis to its endstop making sure the reference position indicated by the software is correct – then calibrated to the thickness of the plate,
2. the build-platform is lowered parallel to the Z-axis by the desired layer thickness,
3. the platform (together with the adapter holding it) is moved along the E-axis to fit beneath the powder container,
4. a pause (a couple of seconds) is initiated and the piezo-actuator below the container is activated, making it vibrate, helping the powder to flow onto the platform by unblocking potential powder clusters (at this point, the gas flow also passes through the container, also forcing powder transport to the platform),
5. the piezo-actuator is stopped and the platform moves back along the E-axis to its original position below the laser optics, and the seal around the opening of the powder container scrapes back the powder exceeding the layer thickness, producing a (ideally) smooth surface and leaving the rest of the powder in the container.

It is important to note that in microgravity, for the gas flow to maintain the powder bed around and on previously built layers, any part built has to be a framework of single lines (curved or straight) to allow passage of the gas [4, 126].

3.2.8 Power management

The device necessarily contains a power source when integrated into the rocket, but in the lab it is powered externally via an umbilical connector (16 –20 Vdc). For safety reasons, MARS-M cannot be started from the batteries but only the umbilical. When this happens, the only device to boot automatically is an Ethernet communication interface, which then awaits remote user interaction. The batteries used for flight are $LiFePO_4$-type batteries (type ANR26650M1A by A123Systems, Inc., two packs in 6S3P configuration, previously qualified for MAPHEUS-payloads [127]) with a nominal capacity of 13.8 A h (i.e. 273 W h). Each one is inserted into its own hatch and can be independently switched on and off. They allow for 30 min of processing time at full power.

3.2.9 Data Acquisition and Communication Interface

Maintaining a clear overview of the many parameters (temperatures, axes positioning, gas flow velocity, etc.) and operations taking place at the same time during the process is critical. Additionally, keeping a log of these values and events is important in order to be able to find sources of error during post-processing. For these tasks a data recorder is used: a single board computer (type Gigabyte GA-SBCAP3450) operating a LabVIEW virtual instrument (National Instruments Corp.). Two cameras and two analogue and digital interface cards are connected to it as peripheral hardware. Below is a list of the sensors connected to the data recorder, directly taken from [1]:

- *high definition camera for overall view of the build-platform,*
- *microscope for detailed view of the Z-movement,*
- *recording batteries and external power source voltages,*
- *pressure transducer to measure inside the experiment chamber, measuring over a range of* $0 - 5\,\mathrm{bar}$*,*
- *mass flow sensor for measurement of the gas stream through build-platform, range* $0.3 - 15\,\mathrm{NL/min}$*,*
- *Pt1000 temperature sensors i. e. attached to laser diode, laser optics, and build-platform,*
- *tilt sensor reads within a range of* $\pm 1\,\mathrm{g}$ *along the Z-axis, and can be used for microgravity detection,*
- *O_2-sensor Roßmann Electronic O2S-FR-T2 to measure inside the experiment chamber, range* $0.1 - 25\,\%$ *O_2,*
- *digital inputs read flight events for lift-off and begin or end of microgravity, as reported by MAPHEUS service system.*

A file on the device keeps a log of *all sensor data, machine states, telemetry and telecommand data,*[1] *as well as potential errors* at a user chosen rate between 10 and 100 Hz, while video recordings are run at 30 fps [1]. These telemetry data and TV-signal is sent by the data recorder, which receives, checks, interprets and executes telecommand packages. The TV-signal allows the user to view the process chamber through two cameras, as well as important sensor and system data.

3.2.10 Ground Station and Ground Support Equipment

In order to prepare the device for testing or launch, some larger equipment is used externally so as to save weight in the payload. This equipment is detached from MARS-M prior to or during lift-off. The Ground Support

---

[1] Telemetry refers to data collected from the device and sent to the ground-station for monitoring, while telecommand data refers to commands sent from the ground-station to the device.

Equipment (GSE) provides external power supply, Ethernet interface, and contains necessities for the process atmosphere: gas bottle, pressure transducer, valves and vacuum pump. Before the launch, the vacuum pump and gas bottle are connected to a gas connector in a hatch, and used to flush the experiment chamber with a defined gas atmosphere. Meanwhile, the ground station consists of a desktop computer connected to the GSE by Ethernet and running LabVIEW virtual environment which communicates to and from the payload (telemetry data, TV downlink, telecommand packages).

3.2.11 Programming and machine limits

Within a given experiment, all the previously introduced software, set-up, and configuration involved can be used universally for additive manufacturing with MARS-M. In contrast, the machine instructions defining an individual manufacturing process in terms of laser power, scanning speed, layer thickness, and scanning strategy, are unique to each part to be manufactured. This variability is handled in MARS-M using standard G-code, Smoothie flavour, and an additional set of M-commands specific to this machine. Any code can be run either from the internal memory card, by a telnet connection from the ground station, or through individual commands typed into the user-interface. During a MAPHEUS flight, a specifically named file will be called from the memory card automatically on start-up (and reboot) to operate independently from the ground station, meaning that the device can still operate in case of communication breakdown.

Most of the G- and M-commands run in MARS-M are to be found in the firmware documentation[2].

These commands are used to generate software scripts (called G-codes) to adapt and optimise the laser speed, scanning velocity, hatching distance, and layer thickness when using a new powder composition. Computer-aided design models can be translated to G-codes adapted for FFF-type printers thanks to a “slicer”[3] to build complex 3D geometries. These G-codes must then be adjusted to the device settings by running it through a LabVIEW software[4] which will remove FFF-specific commands but maintain the information concerning geometry, as well as add commands for laser processing, gas flow, and powder application sequence. Another important task for this software is to make sure the code does not exceed machine limits (maximum axes ranges, for example).

---

[2] `http://smoothieware.github.io/Webif-pack/\documentation/web/html/supported-g-codes.html`, last consulted 21.08.2024

[3] See UltiMaker Cura, `https://ultimaker.com/de/software/ultimaker-cura/`, or open source Slic3r, `https://slic3r.org/`, both last consulted on 21.08.2024.

[4] Written to purpose by Johannes Thore of the Institute of Material Physics in Space, DLR.

3.2.12 Process adaptations

Before being able to build quantifiable parts, i.e., parts that could be analysed for their quality in relation to their building parameters, some peculiarities of the newly built MARS-M device had to be discovered and addressed. These features include the following.

Firstly it was realised that moving the build-platform down in the Z-axis by 0.1 mm did not produce repeatable displacements. The solution to this was to go down by 1 mm and then up by 0.9 mm. This was first written manually in the G-code then was later implemented in the LabView GUI code.

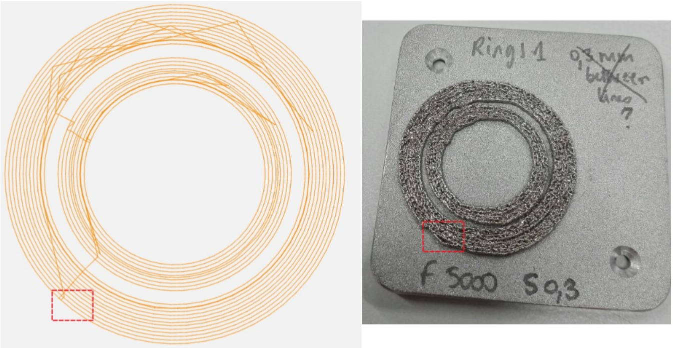

Figure 3.5: An example of rings that were meant to be perfectly circular and concentric according to their G-code (left) but because of differences in inertia/speed for the X- and Y-axes presented deviations (right). The red dashed squares show where the laser starts tracing the shape on the outer ring. For an example of improved circularity, see fig. 5.35.c [1].

Secondly, it was found by building circular items that the X- and Y-axes behaved differently in terms of speed linearity because of inertia (one axis carries the second as part of the construction of the device). This effect is visible in fig. 3.5 which shows two rings. The rings should be circular and the space between the rings should be constant, which is clearly not the case. These deviations were reduced by building half-circles at a time, starting at the lowest point and moving to the highest point (in Y). This way, the shape – though still not perfectly circular – was at least repeatable and symmetric. Later on, code was generally modified to have movements always going in the same Y-direction (here, positive), a procedure common for high-precision linear rails.[5].

Thirdly, one can also see from fig. 3.5 where the laser starts building the sample (red dashed squares), and that once again because of inertia the

---

[5] *Any application that requires high precision will use linear guide systems for their high accuracy and precision capabilities. With smooth and precise linear motion, allowing movement in only one direction, items can be accurately and precisely placed.* `https://www.nskautomation.com/linear-guide-systems/`, last viewed 29.08.2024

build deviates from its intended shape. A related issue was that the laser code by default does not switch the laser off immediately when the command is given to perform a movement with laser off, but powers the laser down linearly, causing a delay. This meant that the built shape deviated from plan. This is visible in fig. 3.6. These issues were solved by adding extrapolations to each end of any G1 command (called G0’ commands) as well as adding an M400 command after each G1 command (see fig. 3.7). A G0’ command is a linear extrapolation displacement from a given G1 command: it is a movement command but uses the same speed as the G1-command. These displacements are $l = 2\,\mathrm{mm}$ long and the positions of A’ and B’ (see fig. 3.7) in (x,y) coordinates are calculated within the code-generator.

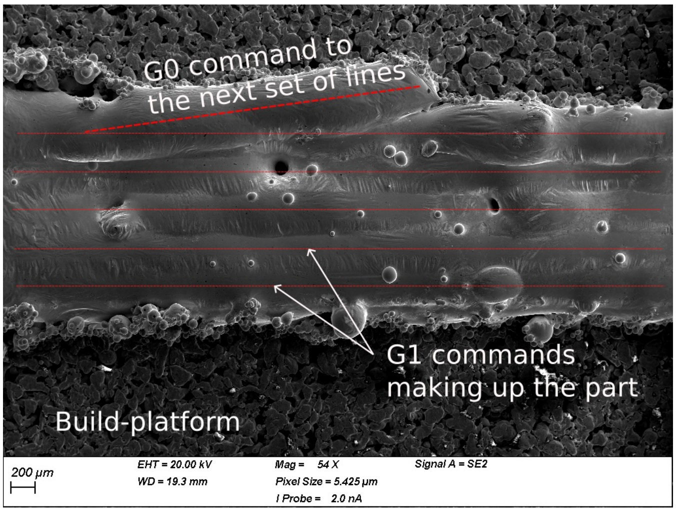

Figure 3.6: Deviation from intended part shape due to laser delay [1].

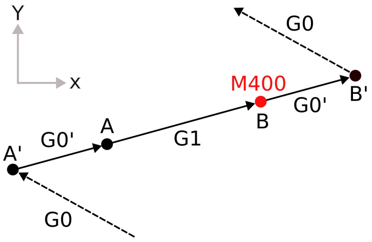

Figure 3.7: Schematic representation the implemented solution using extrapolation, M400 commands, as well as always going in the same Y direction (in this case, positive Y) [1].

The M400 command forces the device to wait until the laser is fully powered down before continuing to the next command in the G-code. The effect of these solutions are demonstrated in fig. 3.8: in (a) the lines are straighter than in (b) (effect of extrapolation) and they do not exceed their end positions such as in (c) (effect of M400 command).

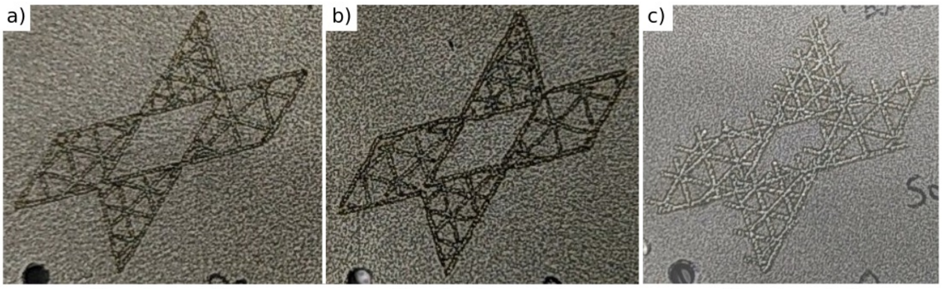

with extrapolation
(G0 to G0' to G1)
with M400 command

without extrapolation
(G0 to G1)
with M400 command

with extrapolation
(G0 to G0' to G1)
without M400 command

Figure 3.8: Comparison of laser markings (no powder used) on the build-platform with or without extrapolation and/or M400 commands [1].

Chapter 4

Methods

This chapter introduces the methods used for this thesis to characterise the feedstock materials in their received form, optimise their AM process on MARS-M, as well as characterise the parts built from them. It details the evolution and results of the building optimisation process, as well as the results of in-depth characterisation of built parts.

4.1 Powder characterisation

The powder characterisation methods were performed together with (and under guidance of) Dr. Janka Wilbig at the BAM, Berlin, Germany.

4.1.1 Flowability

The measurements of powder flowability were performed (or attempted) according to several standards. Throughput rate was measured according to DIN EN ISO 4490:2018 (only applicable for the steel powder, as the others were not flowable enough), while bulk density was measured according to DIN EN ISO 3923-1:2018, and tap density according to DIN EN ISO 3953. With these, the Hausner ratio was calculated according to Carr [128] which outputs a number that is correlated to the flowability of a powder or granular material and is calculated as the ratio between bulk density and tapped density. Finally, a measure of the flowability and cohesion were obtained using a Granudrum[1], see fig. 4.1.

4.2 Built parts characterisation

Microstructural characterisation is probably the most important element in order to judge and improve a new production process. Microstructure is at the root of all other material properties, such as mechanical properties,

---

[1] (Granular Material Flow Analyser, `https://www.granutools.com/en/granudrum`)

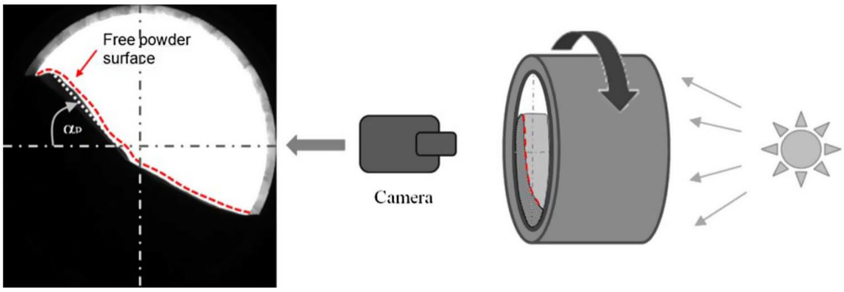

Figure 4.1: Schematic representation of the mode of operation of the Granudrum [129].

chemical, magnetic, etc. It is therefore of utmost importance to perform extensive characterisation of the microstructure. This is done thanks to the following methods.

4.2.1 Sample preparation

First of all, different characterisation techniques require different levels of sample preparation, from simply taking the as-built part (still on the build-platform) for Light Microscopy (LM) to cutting, embedding and polishing for Scanning Electron Microscopy (SEM), to extracting with Focused Ion Beam (FIB) a micron-sized sample for Transmission Electron Microscopy (TEM). For the inner microstructure of a sample to be at all observable using some of the techniques detailed below (microscopy and X-ray diffraction), it is imperative for the surface to be well-prepared. To this end, samples may be cut to access the inner microstructure either using a diamond wire saw (Type DWS.100, Diamond WireTech GmbH & Co.KG) or a diamond disc cutter (IsoMet High Speed Pro precision cutter, Buehler Ltd., ITW Test & Measurement GmbH). The selected separated parts of the sample are then embedded in an electron microscopy compatible resin (PolyFast, Struers S.A.S.) using a hot mounting press (LaboPress-1, Struers S.A.S.). Once embedded in epoxy, the surface must be ground and polished to a mirror-finish, which is achieved on a grinder-polisher (MetaServ 250, Buehler Ltd.) using SiC abrasive paper (CarbiMet, Buehler Ltd.) down to P4000 grain size, followed by polishing on a cloth disc using a polishing suspension at 0.05 µm grain size (MasterPrep, Buehler Ltd.) and finally an oxide polishing suspension with grain size 0.05 µm (OPS Endpoliermittel, Schmitz Metallographie GmbH).

4.2.2 Light Microscopy

A first step towards microstructure observation is LM, which was performed on a AXIO Imager.A2m (Carl Zeiss AG). It allows a simple and quick view of the sample as well as its preparation quality: for SEM, the sample surface has to be adequately prepared (flat, smooth, even, without scratches). Using dark-field view allows to observe surface defects, while polarised light makes the different phases more visible.

4.2.3 Scanning Electron Microscopy

SEM was performed on a Merlin (Carl Zeiss AG). The SEM has a Schottky emitter, which produces a highly monochromatic electron beam. At the location of the sample the beam has a diameter down to $0.8-2\,\mathrm{nm}$ depending on the respective conditions (accelerating voltage of the electrons, beam current, working distance). When the electron beam hits the sample, multiple interactions take place, which are detected by various detectors. The SEM is equipped with detectors for backscattered electrons (AsB, angle selective backscattered electrons), for secondary electrons (SE, Everhart-Thornley with optically coupled photomultiplier), for secondary electrons with low energy (in-lens detector, annular scintillator detector in the column with optically coupled photomultiplier), for backscattered electrons with low energy (ESB, column mounted detector with grid for energy filter), for X-rays (Energy Dispersive Spectroscopy (EDS), energy dispersive X-ray analysis), for diffracted electrons (Electron Backscatter Diffraction (EBSD), electron backscatter diffraction) and for electrons diffracted in forward direction (FSD) in the 70° tilted EBSD geometry. The EBSD measurements were performed with Dr. Matthias Kolbe, Institute for Materials Physics in Space, DLR, Cologne, Germany. The EDX-detector is the Silicon Drift detector (SDD) X-MaxN50 operated under AZtec software by Oxford Instruments, and it was used for compositional analysis. The EBSD-detector is a HKL Nordlys 2 type operated with Channel V software by Oxford Instruments, and was used to study particular crystallographic structure. The secondary electron and backscattered electron detectors were used with energies ranging from $7\,\mathrm{kV}$ to $20\,\mathrm{kV}$ and a probe intensity of $2\,\mathrm{nA}$.

4.2.4 Transmission Electron Microscopy

The TEM samples were extracted from the side of the samples by means of FIB using a Strata 400 (FEI, Inc.) with Ga Liquid Metal Ion Source. These FIB lamellae are approx. $17\,\mu\mathrm{m} \times 4-7\,\mu\mathrm{m}$ (height × depth) in size. Scanning transmission electron microscopy (STEM) was performed in bright-field mode using a JEM-F200 (JEOL GmbH) operated at an acceleration voltage of $200\,\mathrm{kV}$ and equipped with a OneView camera (Gatan, Inc.) for high-resolution imaging. The amorphicity was investigated by Selected Area Electron Diffraction (SAED), while additional information on the chemical composition of the phases was obtained in STEM mode by EDS (Oxford Instruments). These measurements were performed by Chijioke Kenneth

Akuata and Dr. Christoph Altenbach of the RWTH Aachen.

4.2.5 Synchrotron X-ray Micro-Diffraction

X-ray Micro-Diffraction (μXRD) measurements were performed with Dr. Olof Gutowski at the P07 High Energy Materials Science Beamline at the Deutsches Elektronen-Synchrotron (DESY), Hamburg, Germany on AMLOY-Zr01 and AMLOY-Zr02 additively manufactured with MARS-M. The samples were built with the parameters shown in table 4.1.

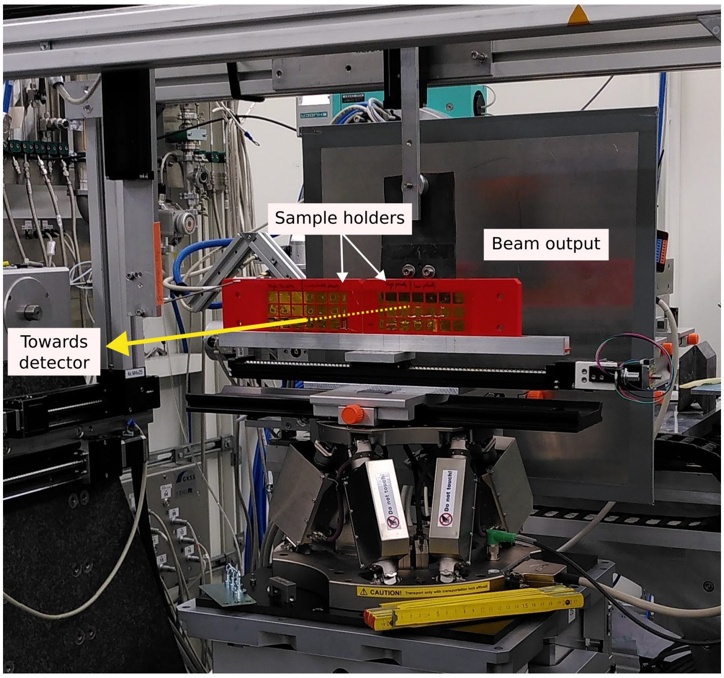

Figure 4.2: An example of samples in a custom-built sample holder. The samples are held between two layers of Kapton tape. The holder is then placed perpendicular to the beam.

The samples were set in the “windows” of a custom-made sample holder (see fig. 4.2) by having them held by two layers of Kapton tape on either side of said windows. They were analysed/observed in transmission by scanning from the top downwards (in Z, down the stack of layers), 2 scans per sample. Most measurements were conducted so that the beam was parallel to the

Laser power (W)	80		170		115	135
Speed (mm min^{-1})	4000	5500	4000	5500	5500	4000

Table 4.1: Parameters for samples of AMLOY-Zr01 and AMLOY-Zr02 examined under synchrotron μXRD.

building-XY (i.e. the horizontal) plane, perpendicular to the X-axis (i.e. to the longest dimension). Some of the samples were afterwards rotated along their longest dimension to also observe changes along the YZ-plane. Measurements were carried out in transmission geometry with an incoming X-ray energy of 103 keV using a $2\,\mu m \times 30\,\mu m$ beam and a Pilatus flat panel detector at about 350 mm downstream from the sample position, in order to ensure sufficient transmission and an accessible q-range of $1 - 15\,\text{Å}^{-1}$. To achieve a spatial resolution of 2.5 µm, the measurements were done in continuous scanning mode (at $2\,\mu m\,s^{-1}$) along the direction shown in fig. 4.3a, and the sampling rate was set to 0.25 s per frame (4 Hz).

The raw data produced are frames showing diffraction rings, which are to be calibrated and integrated using PyFAI (Python Fast Azimuthal Integration) software [130, 131]. The calibration is required because the alignment of the beam, sample and detector can never be perfect. It allows to adjust for the distance from the samples to the detector, the angles to the detector, as well as to define a so-called mask taking into account the gaps between the different panels constituting the detector and any damaged pixel they might possess. The calibration is run on a measurement

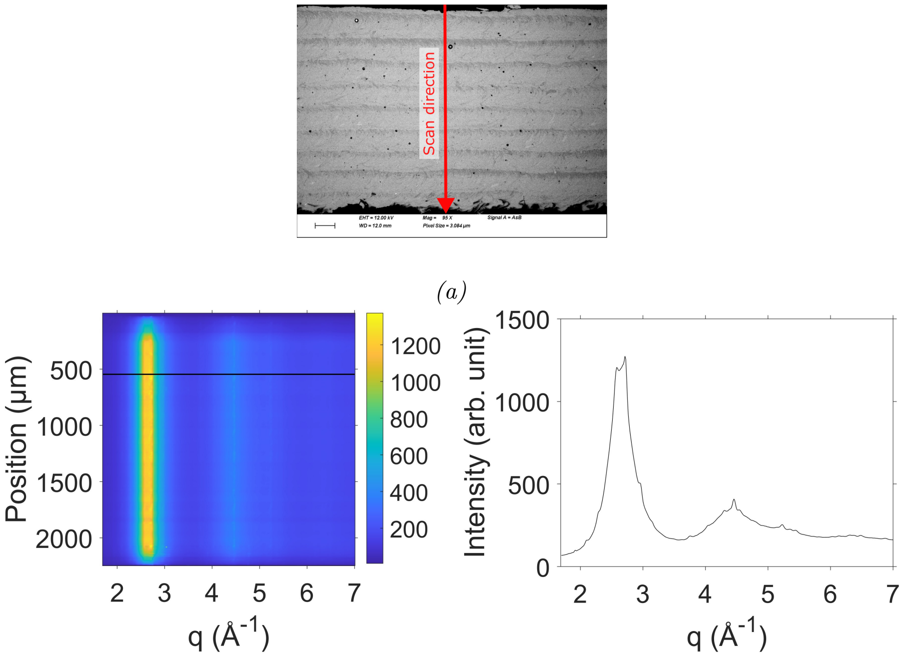

(a)

(b) *(c)*

Figure 4.3: (a) SEM micrograph of a sample with an arrow indicating the diffraction scan direction (the scalebar represents 20 µm *and the contrast was increased for clarity). (b) Example of result of the integration of micro-diffraction scans along a sample build height, where the diffraction pattern extracted at the black line is shown in (c).*

of a reference material (CeO_2) and produces a .poni file which is used for the next step: integration of the data, that is to say, binning in a polar coordinate system and integrating the detector intensity so as to obtain a one-dimensional plot of intensity versus q or 2θ (such as in fig. 4.3c). The data is then concatenated over the build height as shown in fig. 4.3b. The data processed at the beamline was output as .h5 files which were analysed using custom-made code in GNU Octave [132] and Matlab [133].

4.2.6 Synchrotron X-ray Diffraction Tomography

In CT, a 3D-object is usually cut into 2D-slices, obtained by analysing absorption or phase contrasts within the object. The produced images are then compiled to reconstruct a 3D-model of the object. Here, a 2D-slice is instead reconstructed from 1D-cuts/beams by measuring the X-ray Diffraction (XRD) of the synchrotron beam while rotating the object. The third dimension is represented in the intensity of diffraction data.

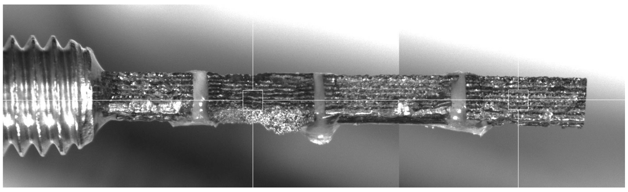

Figure 4.4: Samples prepared for CT scans, with example locations of two scans on sample 2 and sample 4.

XRD-CT measurements were performed by Dr. Olof Gutowski at the P07 High Energy Materials Science Beamline at DESY on AMLOY-Zr01 and AMLOY-Zr02 additively manufactured with MARS-M with $4750\,\mathrm{mm\,min^{-1}}$ and 80 W or 170 W. Here the photon beam energy was reduced to 73.3 keV in order to have higher flux and detection efficiency. Similarly to the micro-diffraction experiments, the beam size is set to be as small as possible: also $2\,\mu m \times 30\,\mu m$. The samples were glued end to end in a line to a screw (see fig. 4.4) and placed on a sample holder. Each sample is then “scanned” by the beam over an angle of 360 deg. The diffracted beam is collected by a DECTRIS Eiger4m CdTe detector placed at a distance of 400 mm covering a usable q-range of $0.5 - 8\,\text{Å}$ running at 500 Hz (2 ms exposure time). The reconstructed datasets consist of 800 projections distributed over an angle of 360 deg (a projection per 0.45 deg). Furthermore, for each projection a range of 3.6 mm (height of the sample plus margin) was scanned in the vertical direction at a constant speed of $1\,\mathrm{mm\,s^{-1}}$. At a frame-rate of 500 Hz, this yields 1800 frames. In total, for one CT scan, $800 \times 1800 = 1.44$ million frames are produced, with a resulting voxel-size of $2\,\mu m \times 2\,\mu m$. The data structure is described in fig. 4.5 on the following page. These frames are then translated to calibrated diffraction patterns through the same process

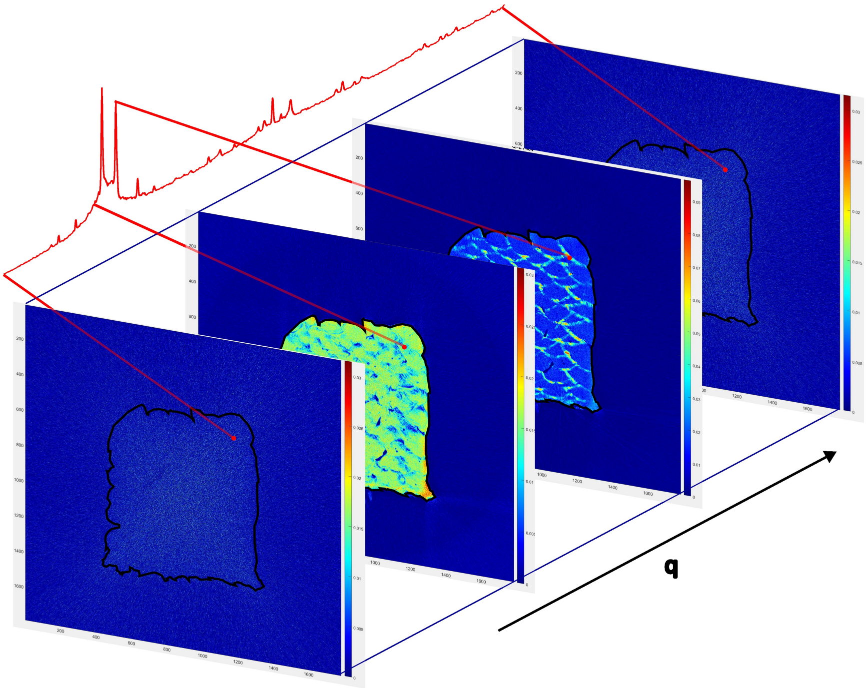

Figure 4.5: Schematic representation of the data structure of XRD-CT files, and the diffraction pattern extracted from one pixel (same red dot position on all images) over the whole q-range.

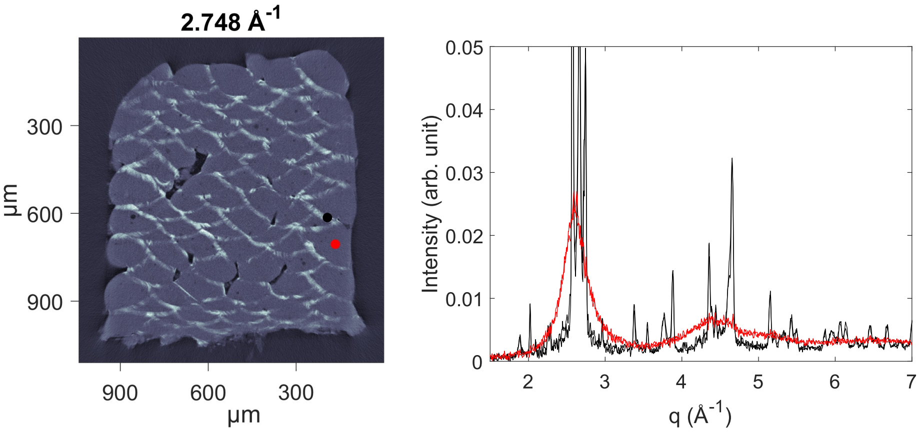

(a) *(b)*

Figure 4.6: (a) Arbitrary slice (arbitrary q-value) of XRD-CT data with two selected points (in red and black) for which the diffraction patterns (over slices covering a q-range of $1.5 - 7\,\text{Å}^{-1}$*) are given in (b).*

described earlier. The data is then reconstructed into a series of 2D images (one image per q-value) using Matlab. These steps were performed by Dr. Olof

Gutowski (DESY).

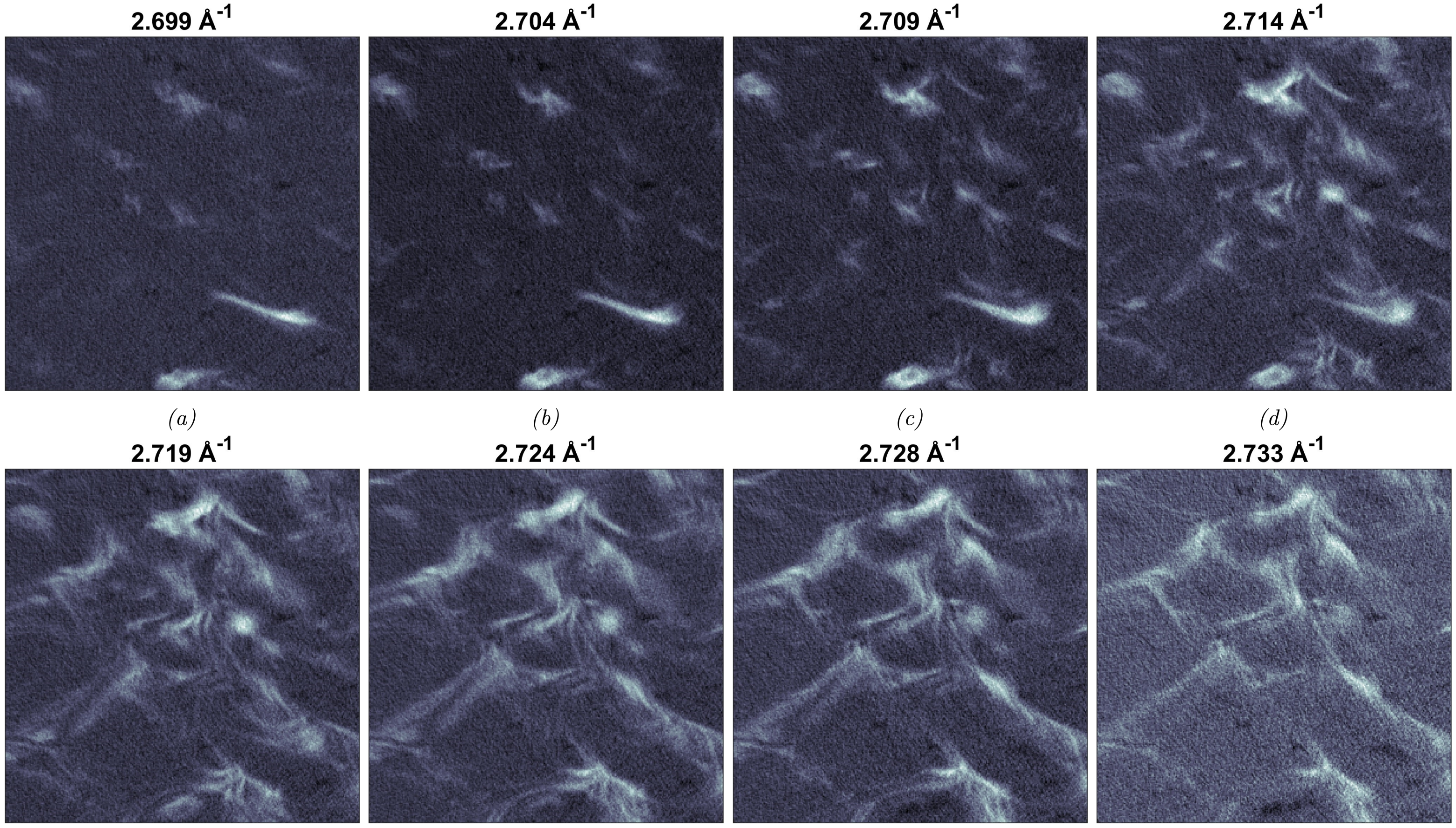

(a) (b) (c) (d)

(e) (f) (g) (h)

Figure 4.7: Crystalline wave seeming to spread through AMLOY-Zr02 from (a) $q = 2.699\,\text{Å}^{-1}$ *to (h)* $q = 2.733\,\text{Å}^{-1}$. *The dimensions of the cut are* $600\,\mu\text{m} \times 600\,\mu\text{m}$.

In total, at least two scans per sample were performed. The result of each scan is saved as a .h5 file containing two sub-structures: the diffraction intensity data for each pixel of the image given in a matrix, and the q-values in a vector. For each 2 µm-sized pixel, a diffraction pattern is therefore available. Figure 4.7 shows a cropped part of an image over several consecutive slices (i.e. q-values). The variation in local pixel intensity is visible with varying q-range and provides information as to the locality of present phases.

Some of the data was modified so that no data point would be negative. Generally, negative data can arise when the dark image of the detector (necessary for calibration) is performed before the detector has completely "quieted down" from the last exposure. This simple correction involved adding the absolute value of the minimum data point to all points of the matrix.

4.2.7 Differential Scanning Calorimetry

Two samples each of AMLOY-Zr01 and AMLOY-Zr02 were evaluated using a power-compensated DSC, PerkinElmer, DSC8500, by Lucas Ruschel of the Saarland University. This type of DSC possesses two identical furnaces held inside a thermostatic chamber, one containing the sample to be examined and the other being the reference, as shown in fig. 4.8. Each furnace has a temperature sensor and a heating wire, so that when the sample undergoes a thermal reaction and a temperature difference appears, heating of the sample will be adapted to return to the reference temperature [134]. Samples between 20 and 30 mg in mass were first heated at 20 K min^{-1} from approx. 300 K to 850 K (30 °C to 580 °C) reaching beyond the crystallisation temperature. A second heating cycle was then performed in order to establish the crystalline baseline. The measurements were corrected for instrumental drift between the samples by following the recommendation of Slipenyuk & Eckert to match

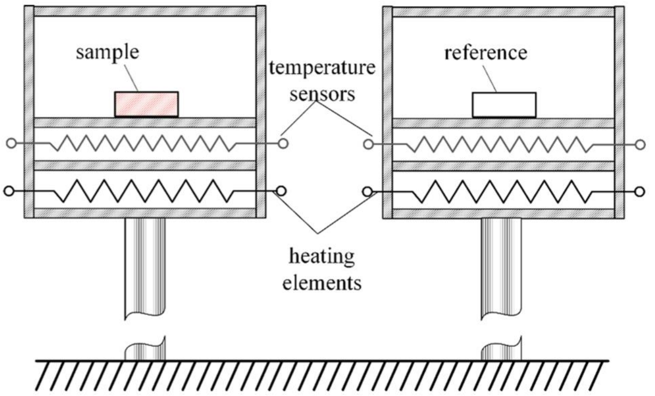

Figure 4.8: Schematic representation of power-compensating DSC. Taken from [134].

the supercooled liquid regions [135], defined as being between T_g and T_x.

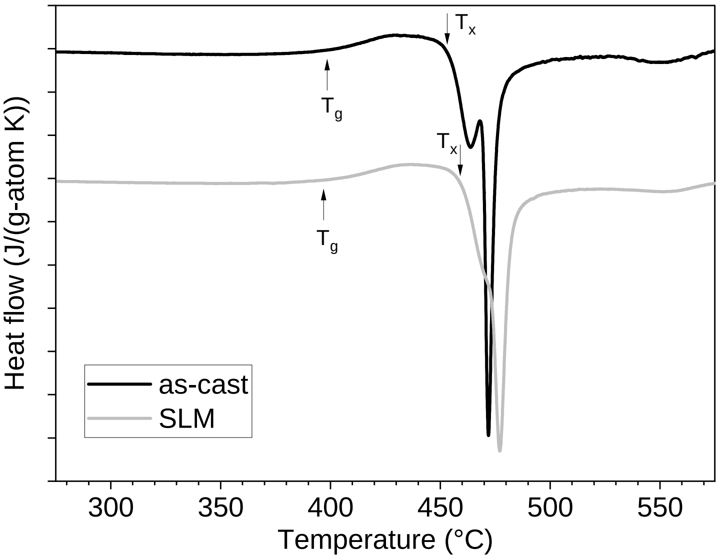

Figure 4.9: DSC scans at $20\,\mathrm{K\,min^{-1}}$ *of cast and PBF-LB AMLOY-Zr02 samples.*

A measurement of AMLOY-Zr02 is plotted in fig. 4.9. It shows a difference in the onset of the glass-transition between cast and additively manufactured AMLOY-Zr02. The shape of the DSC curves provides information on T_g, T_x, and the crystallisation enthalpy (the area between the curve and the baseline at the crystallisation peak). From these, an estimation of the amorphous fractions of the various samples is determined.

The samples measured were built at $4750\,\mathrm{mm\,min^{-1}}$ with 80 W and 170 W, for both AMLOY-Zr01 and AMLOY-Zr02.

4.2.8 Nanoindentation

The mechanical properties were touched upon using nanoindentation according to the method developed by Oliver & Pharr [136]. The tests were performed by Katarzyna Mulewska and Edyta Wyszkowska at the Materials Science laboratory, at the National Centre for Nuclear Research (NCBJ), Swierk-Otwock, Poland, on a NanoTest (MicroMaterials Ltd.) using a Berkovich indenter on samples embedded parallel to the laser direction, built with the following parameters: (1) 80 W and $5500\,\mathrm{mm\,min^{-1}}$, (2) 80 W and $4000\,\mathrm{mm\,min^{-1}}$, (3) 170 W and $5500\,\mathrm{mm\,min^{-1}}$, (4) 170 W and $4000\,\mathrm{mm\,min^{-1}}$.

The geometry of the indenter is shown in fig. 4.10 on the facing page. The measurements involved approaching the three-sided pyramid shaped diamond to the surface and following the loading and unloading sequence presented in fig. 4.11a on the next page. Before the measurements, calibration was

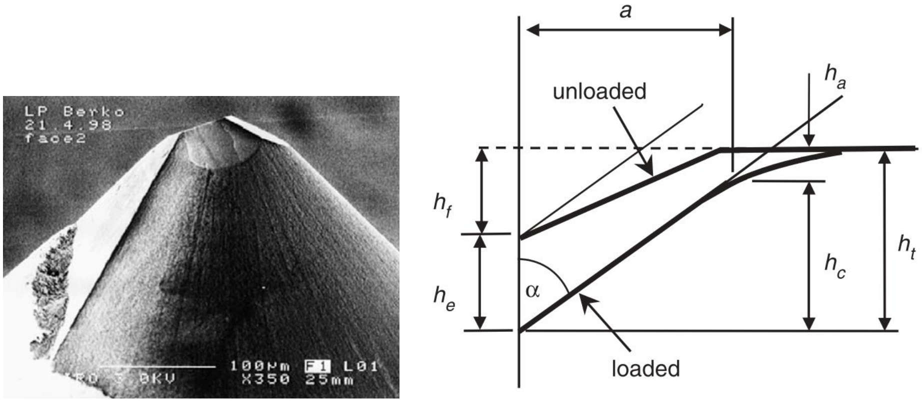

(a) (b)

Figure 4.10: (a) SEM view of a Berkovich diamond indenter, (b) cross-section of specimen surface at upon complete loading and unloading load for an elastic–plastic indentation [137].

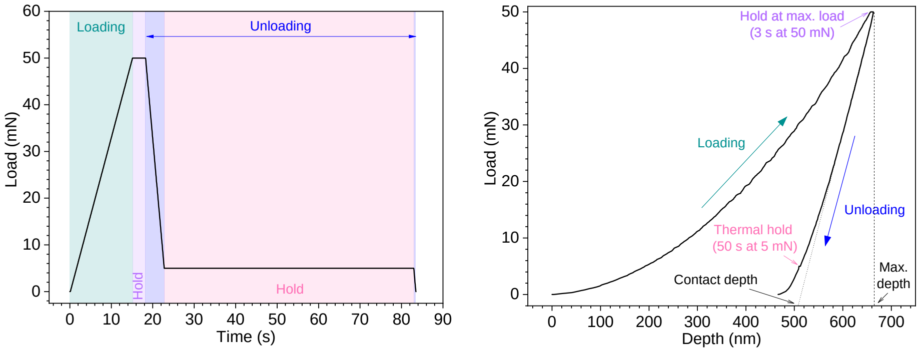

(a) (b)

Figure 4.11: (a) Loading sequence applied and (b) typical example of load-displacement curve obtained from this sequence in nanoindentation.

performed on a flat polished fused silica surface. This allows to determine the wear of the indenter and adapt the future measurements accordingly. A distance of 30 µm was set between the indents. In total, after removal of the measurements that had to be deleted due to bad surface contact (pores, local height differences), approx. 50 indents (between 48 and 56 depending on the sample) were performed on each embedded polished sample. Results are extracted from load-displacement curves such as the one shown in fig. 4.11b. The curve consists of a loading section (with constant loading rate of 3.33 $\mathrm{mN\,s^{-1}}$) where both elastic and plastic deformation take place, then of a 3 s hold at a maximum load of 50 mN, then an unloading section (constant unloading rate of 10 $\mathrm{mN\,s^{-1}}$) interrupted by a thermal hold of 50 s at 5 mN and finally the last part of the unloading. It is assumed that only elastic deformation occurs during unloading. The hold at max. load reveals whether creep is an issue with the material, which was not the case here. The thermal hold is performed to reveal whether there is a temperature difference between the indenter and the material surface. At the length-scales involved, thermal expansion can have drastic effects on the mechanical results obtained. Here however, the load-displacement curve in fig. 4.11b reveals very little displacement over the 50 s hold, meaning that the sample and indenter were close enough to the same temperature to obtain accurate results. After sample retrieval, the indents were observed in SEM.

Chapter 5

Results and Discussion

This chapter presents the results obtained from the methods introduced previously, starting with the characterisation of the powder feedstock, then moving on to describe the evolution and results of the building optimisation process with MARS-M, as well as the results of in-depth characterisation of built parts. The influence of various parameters and phenomena on the amorphicity of the samples is discussed. A large portion of this chapter is reported in a paper currently under review [3].

In this part, two different types of samples are mentioned: lab-samples produced on ground and microgravity (µg) samples produced during the sounding rocket flights. The lab-samples were required to determine the influence of various parameters on the quality and therefore to choose the parameters to use during the few (and short) microgravity campaigns with the MAPHEUS sounding rocket. Much more time was therefore spent on evaluating the effect of different parameters on lab-samples.

5.1 Powder characterisation

The powders used as feedstock were compared in their properties with stainless steel 1.4404 (also known as X2CrNiMo17-12-2 or 316L) which is a commonly used composition for PBF-LB.

5.1.1 Morphology

The powder size distributions were analysed by laser diffraction, the results of which are detailed in table 5.1 and fig. 5.1 on the following page. The manufacturers' information: 15 – 45 µm for AMLOY-Zr01[1] and AMLOY-Zr02, 20 – 53 µm for stainless steel 1.4404. However, the experimental results on the selected portions of powder are partly different. First of all,

---

[1] Originally, AMLOY-Zr01 powder of size 45 – 100 µm was used, but it was soon replaced by the smaller grain size, for reasons detailed further on.

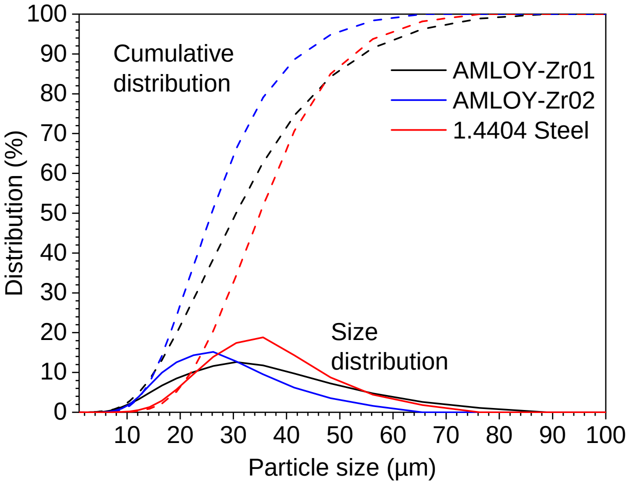

Figure 5.1: Powder size distributions for AMLOY-Zr01, AMLOY-Zr02, and stainless steel 1.4404.

Material	Mean diameter	D(0.1)	D(0.5)	D(0.9)
AMLOY-Zr01	32.85	15.13	30.48	54.21
AMLOY-Zr02	27.58	15.19	25.91	42.64
1.4404 Steel	36.23	22.08	35.04	52.11

Table 5.1: Powder size properties in µm *for AMLOY-Zr01, AMLOY-Zr02, and stainless steel 1.4404.*

AMLOY-Zr01 and AMLOY-Zr02 have different size distributions. AMLOY-Zr01 powder has a broader spread that expected, while AMLOY-Zr02 and stainless steel 1.4404 are within the specified ranges. This could be explained by the AMLOY-Zr01 powder having been acquired up to two years earlier than the AMLOY-Zr02 powder. This could lead to more oxidation occurring in AMLOY-Zr01. However, the powders were examined in synchrotron diffraction and no clear oxidation peaks were observed. It is assumed that if the differences in size were due to oxidation, the effect would be visible in diffraction. Another consequence of the earlier purchase date is that the powder will have travelled more than the others. Indeed, travelling back and forth by road transport from Cologne to Kiruna in the north of Sweden for MAPHEUS campaigns could have caused the larger particles to migrate upwards in the container, changing the size distribution along the container axis. In this case a potential remedy for the next campaigns would be to turn the container upside down when travelling back to Germany. It is also possible that the differences are due to statistical variations in the manufacturing process and the size of our measured batch.

Nevertheless, differences in size distribution are expected to affect the

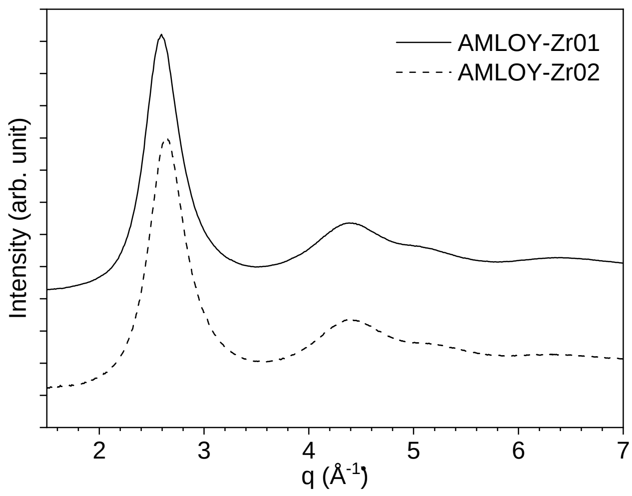

Figure 5.2: Synchrotron diffraction results for AMLOY-Zr01 and AMLOY-Zr02 powders. The main Bragg peak for AMLOY-Zr01 can be described as sharp but this could be due to data resolution, as no other peaks are visible.

flow properties [138] detailed next.

5.1.2 Flowability

None of the standardised methods mentioned in chapter 4 on page 32 allowed for measurements of the flowability of AMLOY-Zr01 and AMLOY-Zr02, as these powders were too cohesive. Because the low flowability of AMLOY-Zr01 was initially attributed to absorbed humidity, the powder was dried before a second measurement. The flowability did not seem to vary, as the standardised methods were still inapplicable. The tapped packing density (determined as the ratio of tapped density to theoretical density) was measured before and after drying at 105 °C for 4 h and the results showed that the density was virtually unchanged (0.60 before and 0.59 after drying).

However, Granudrum measurements provided more insight into the powder flow properties[2] (detailed reports are provided in the appendix C on page 103). Some visual results are presented in figs. 5.3 and 5.4. In the first figure, flow angles for the different powders are shown silhouetted in the Granudrum, overlayed with a band showing average heap position and standard deviation. stainless steel 1.4404 powder has the smoothest heap aspect no matter the rotation speed (given in rotations per minute). A drastic increase in the chaotic aspect of the heap is seen for AMLOY-Zr01 at the highest speed, and to a lesser extent, AMLOY-Zr02. Except at the highest speed, the flow angle of AMLOY-Zr01 is the steepest among all

---

[2] The powders were not dried prior to the measurements.

powders. This is confirmed by the data in the second figure, which compares the powders in terms of flow angle and cohesion. In this figure, it is shown that the AMLOY-Zr02 and stainless steel 1.4404 powders have similar flow angles, and both increase with angular speed, while AMLOY-Zr01 powder is less flowable but does not seem affected by angular speed. Up to (and including at) 20 RPM AMLOY-Zr01 has both higher cohesion and higher flow angle than stainless steel 1.4404. The switch at high speeds may be deduced as originating from the high noise.

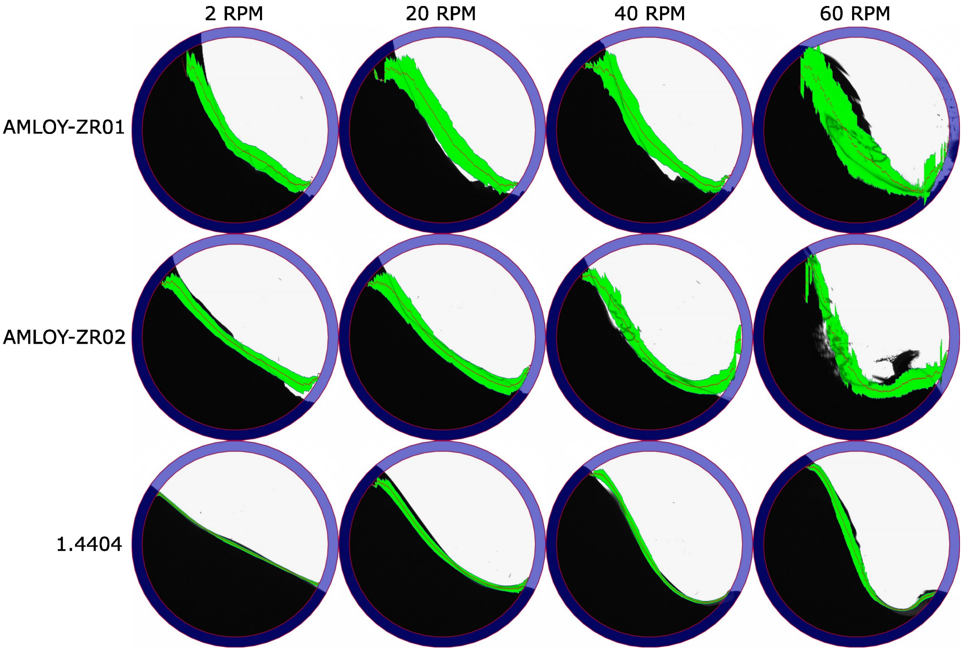

Figure 5.3: Comparison of flow angles for BMG AMLOY-Zr01, AMLOY-Zr02, and steel stainless steel 1.4404 at 2, 20, 40 *and* 60 RPM.

The literature suggests that smaller particle sizes lead to higher cohesiveness, however we see here that despite having smaller particles, AMLOY-Zr02 still shows lower cohesion and better flowability than AMLOY-Zr01. This can possibly be explained once again by the earlier purchase date of the latter, which may have absorbed more humidity over time (though initial tests with dried powder did not show any difference). Humidity would indeed increase cohesive forces between the particles and negatively impact flowability [139]. The cohesiveness of AMLOY-Zr01 is expected to affect its spreadability during the recoating process of PBF-LB, as higher cohesiveness results in a decreased powder layer quality [140, 141]. It was indeed observed that AMLOY-Zr01 was more difficult to spread into an even layer than stainless steel 1.4404 powder, as it tends to clump together. On the other hand, smaller powder grain sizes lead to lower surface roughness, fewer pores frozen into the melt-pool, and better microstructural homogeneity in general, as discussed in chapter 2 on page 3.

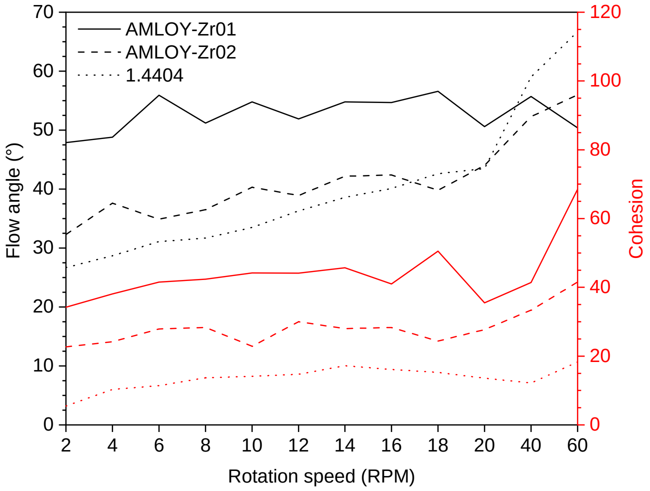

Figure 5.4: Comparison of GranuDrum results of flowability and cohesion of AMLOY-Zr01, AMLOY-Zr02, and stainless steel 1.4404 steel.

In practice, because of its higher flowability, stainless steel 1.4404 powder was found to leak more within the device, causing more losses than when using AMLOY-Zr01 or AMLOY-Zr02.

5.2 Parametrisation of the building process

As this work's main focus is AMLOY-Zr01, the following optimisation process pertains to this material. When a narrower set of parameters was found to produce higher density samples, this set was also applied to AMLOY-Zr02 and was found to be satisfactory. Both materials are then investigated in terms of characterisation of the effect of that selected set of parameters.

In order to find the parameters deemed optimal for the use of AMLOY-Zr01 with MARS-M, a variety of tests were run in the lab to better grasp the functioning of the device and how to obtain samples that could be analysed at all. These tests started as simple lines (beginning on the left-hand side, see fig. 5.5a, b, and c) of different laser powers using a single layer of powder. The initial power and scanning speed ranges were chosen to be around those of prior parts built to test the device hardware, however, these turned out to be quite far from optimal settings.

Figure 5.5a shows the first lines built with MARS-M still in their powder bed, with increasing laser power for each line. These lines are mostly made up of separate droplets due to balling and were found to not be attached to the build-platform owing to the too large thickness of the first powder layer. It is not possible to distinguish any coherent dependence on laser

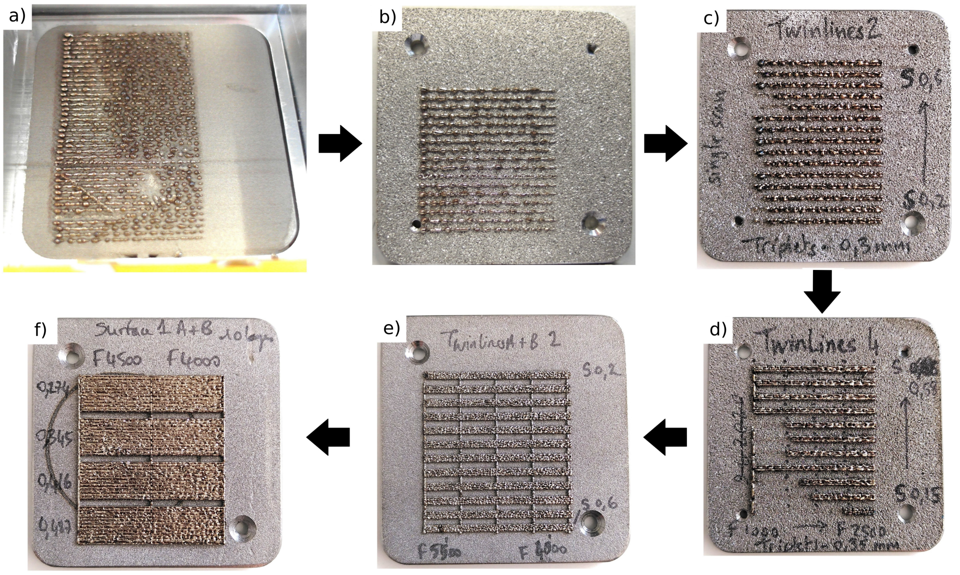

Figure 5.5: Overview of the milestones in the improvement of parameters and scanning strategy. The arrows indicate the chronological order.

power. Large balls of solidified material are visible at the beginning of the lines. These effectively stopped any attempt to apply a second layer, as they would detach and get caught in the mechanism, at best scraping lines into the powder layer, at worse blocking the mechanism completely. The first powder layer is the most inconsistent as its evenness depends on how the user tightened the screws holding the build-platform in place, and the layer thickness depends on what the initial Z-position was estimated – by sight and touch – to be. This was only improved by accumulating experience with MARS-M (i.e. a lot of trial and error).

Figure 5.5b shows a more limited amount of lines where it is – still – very difficult to find any particular difference between the lines, but all lines are welded to the platform thanks to a thinner first powder layer. Figure 5.5c shows patterns made up of three lines with 300 µm hatch distance.[3] The reason for increasing the width (in Y) of these lines was that until then, any characterisation other than optical of the samples had been difficult. More material meant more to characterise and qualify.

Figure 5.5d shows a progression with a vertical line (along Y) in an attempt to remelt the balling at the beginning of the lines, which proved mostly successful. Between figs. 5.5d and 5.5e, there is significant change and improvement: reduction in porosity size of the build-platform, reduction in the powder grain size, and changes in the scanning strategy.

---

[3] The first test with lines made up of two lines were named “Twin lines” and this denomination was kept for any such segments made up of two or more lines.

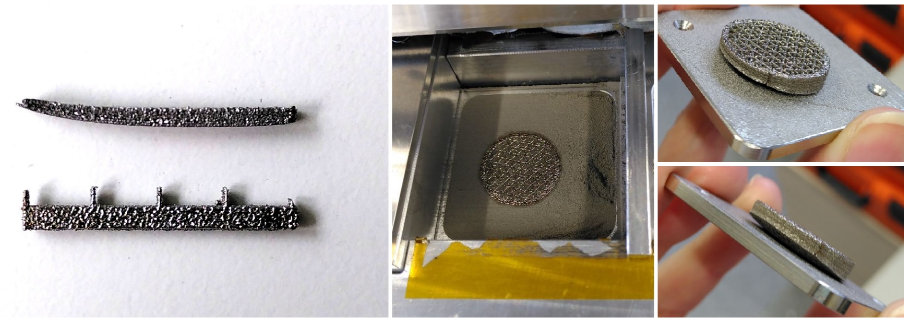

Figure 5.6: Example of distorted samples. When viewed from above, the distortion is not visible.

Distortion and delamination due to residual (thermal) stress was a big problem during the optimisation process. As shown in fig. 5.6, a part could seem “normal” but actually be distorted and detached from the build-platform within the powder bed. At worse, some parts would distort so much as to block and damage the powder recoating mechanism. In cases where the parts did not detach, they would “take the build-platform with them” and cause it to bend (this was especially true for the thinner build-platforms used first, see below). In an attempt to alleviate residual stresses, the scanning strategy was changed from using identical codes for each layer to using an alternation of code A and code B, where the lines in each are displaced by half a hatch-distance to each other and are produced in opposite directions: left-to-right (A) vs right-to-left (B), as shown in fig. 5.7. This improved the density but only seemed to affect the residual stress in that samples then detached from both ends less than a single end would, as seen in fig. 5.8 on the following page. Though flowability decreases with decreasing grain size [140] thus reducing the quality of the powder layer, the grain sizes were reduced from 45 – 100 µm down to 15 – 45 µm which resulted in parts with (1)

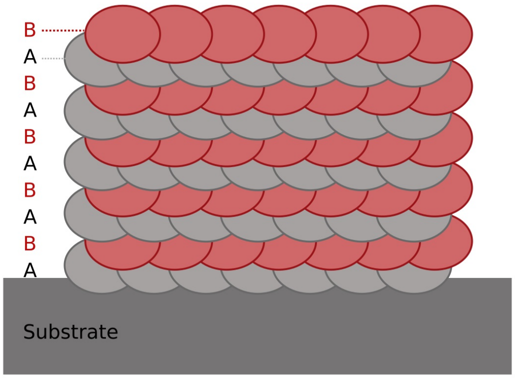

Figure 5.7: New scanning strategy employing two alternating layers A and B.

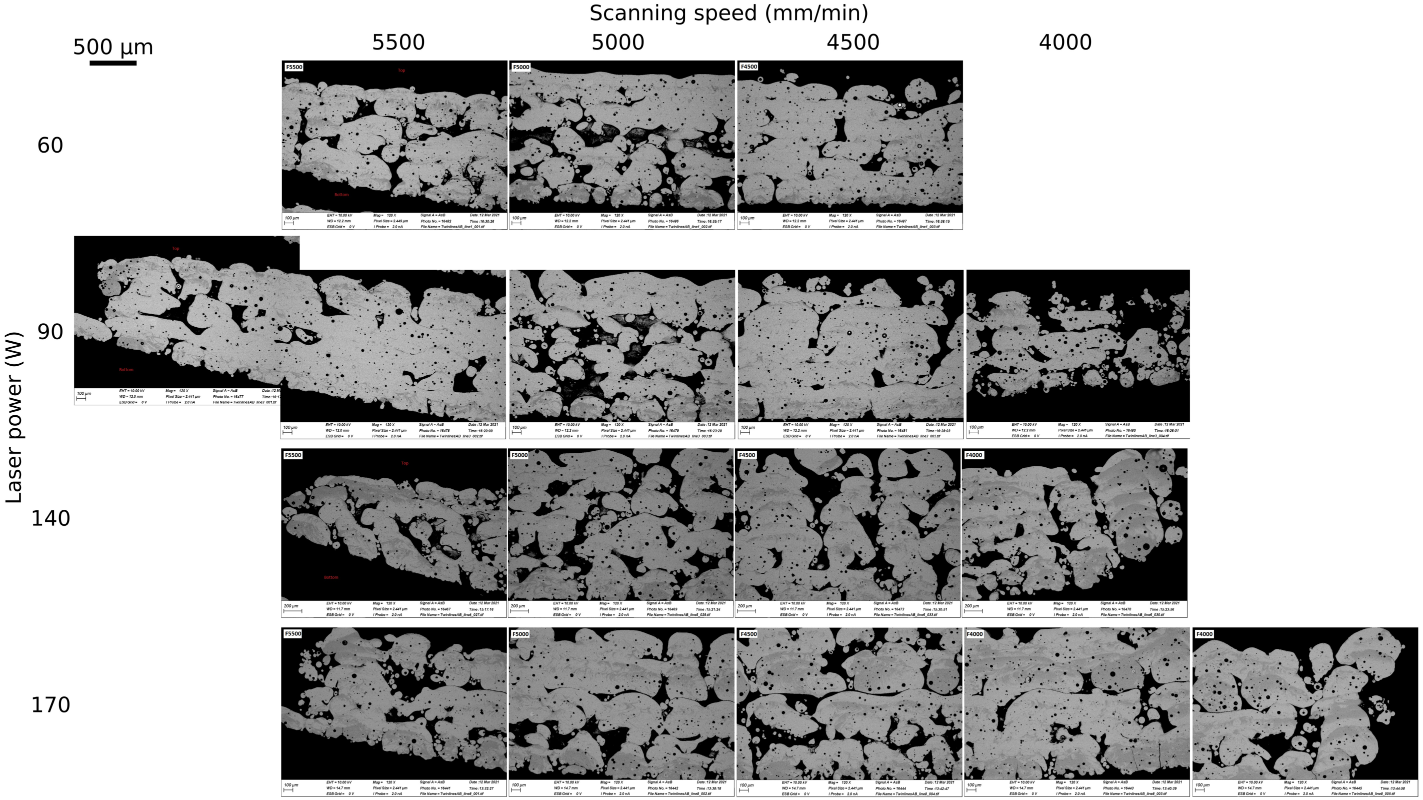

Figure 5.8: Cross-sections of TwinlinesAB (such as those shown in fig. 5.6 on the preceding page, left) with varying powers and scanning speeds. These samples all detached partly from the build-platform and are far from fully dense.

a better outer appearance, (2) fewer pores, and (3) less crystallisation than 45 − 100 µm grain sizes. (1) is thought to be due to the effect presented in section 2.3 on page 10: larger grains lead to increased surface roughness. For (2), as also previously mentioned, smaller particles are expected to contain fewer pores, and (3) is probably due to better heat conduction and so higher cooling rates due to lower porosity and better connection between different lines within a segment. Furthermore, larger AMLOY-Zr01 powder grains were found to be partly crystalline [141], which in parallel with a decreased absorptivity of the laser power could mean these particles are not all fully melted, retaining their crystalline fraction (see fig. 5.9, which shows an unmelted powder grain within a built sample). The smaller sized particles were indeed measured in synchrotron beam diffraction to be amorphous, and a bed made of smaller particles will more readily absorb energy from the incoming the laser beam [84].

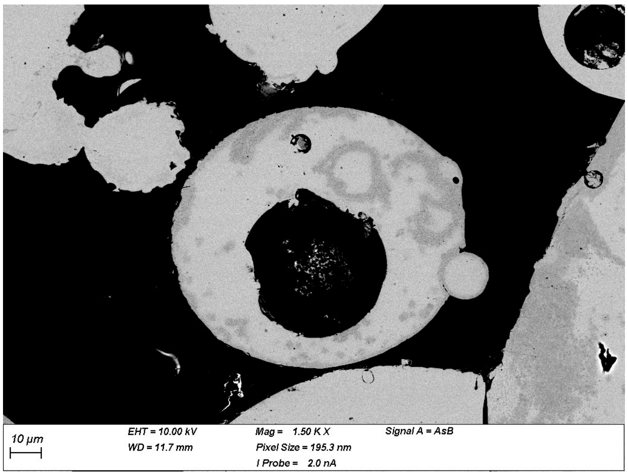

Figure 5.9: Example of unmelted powder particle containing one large and one small pore, as well as crystals (darker regions). This particle was found in a large hole within a built sample.

Further changes were to the build-platform. Firstly, its porosity: the pore size was decreased from 25 to 8 µm. This is understood as having led to much more even flow behaviour of the melt as the holes in the surface were smaller and more even, and therefore to higher repeatability between parts produced from identical code. Secondly, the build-platform thickness was increased from 3 mm to 5 mm. It was found that the samples deformed less, which corresponds to findings in the literature indicating that increasing the build-platform height leads to less stress in the platform itself and a more homogenous residual stress distribution in the sample [86]. Finally, the plate was changed to be fixed by four screws instead of two. This lead to less bending after the process, possibly from increased heat conductivity to the rest of the device.

All these changes together proved helpful in improving the building process and better quantifying the effect of varying parameters on the density and amorphous content through various characterisation methods.

LM was instrumental in the first stages to see which building parameters were improving density of the parts, as seen in fig. 5.10. Images like these were then analysed using ImageJ [142] to determine the density. Results are shown in fig. 5.11. This in time led to the moderately improved builds seen in fig. 5.12 on the next page. It was from early on clear that crystallisation was occurring, as seen in fig. 5.8 on page 52, where the dark areas are crystalline. What can be considered as the "final form" of the samples produced for parameter optimisation is shown in fig. 5.13 on the next page: segments of different parameters, delimited by vertical (along Y) lines. Once these mostly dense samples were obtained, more effort could be put into understanding how this crystallisation occurred and how different building

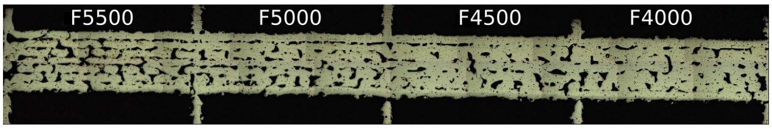

Figure 5.10: LM of Twinlines of AMLOY-Zr01 built with 72 W *and* 5500 *to* 4000 mm min^{-1}*, polished down to a flat surface. The density is visibly affected by the scanning speed.*

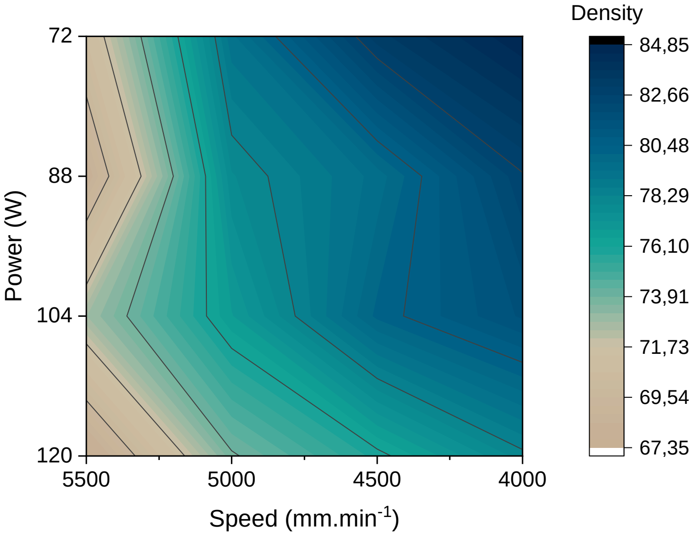

Figure 5.11: Density measurements depending on scanning speeds obtained from analysis of images like fig. 5.10, from samples built with different powers. The axes are reversed to match orientations in figs. 5.12 and 5.10.

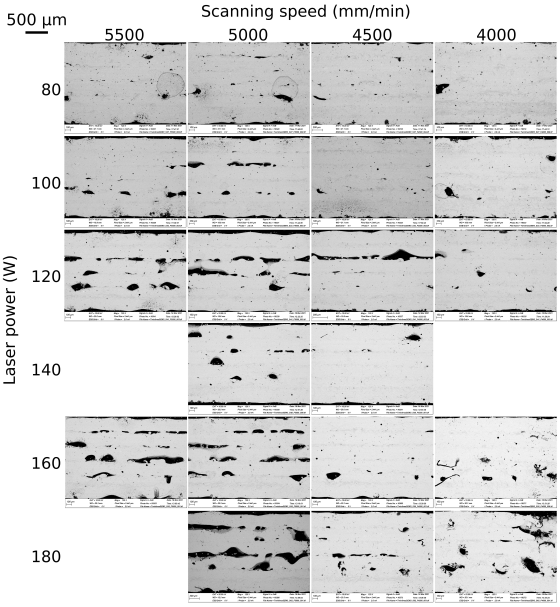

Figure 5.12: SEM cross-sections of TwinlinesAB (from above, still attached to the build-platform) with varying powers and scanning speeds.

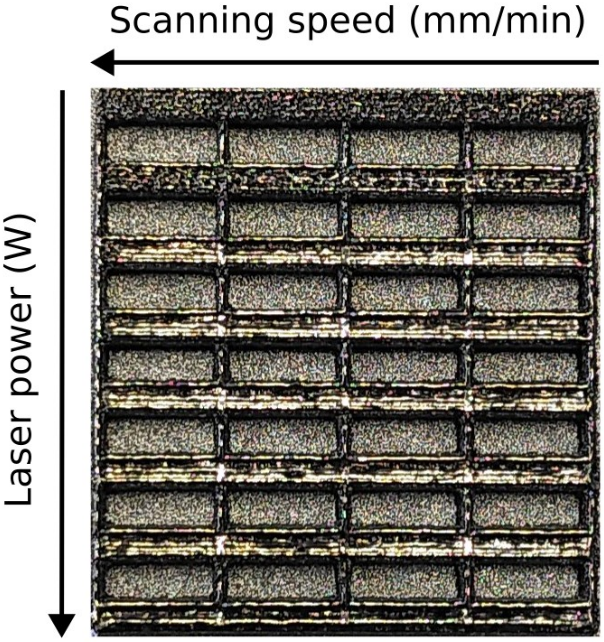

Figure 5.13: Final form of TwinlinesAB (from above, still attached to the build-platform) where each segment was built with varying powers and scanning speeds. These samples are used for parameter effect characterisation and optimisation.

parameters influenced the crystalline fraction of the built samples.

5.3 Presence of crystalline regions

The presence of crystalline phases mentioned above was confirmed in synchrotron measurements, as shown by the sharp peaks in fig. 5.14 which gives the average diffraction pattern over the entire height of the AMLOY-Zr01 sample with the highest energy density (i.e. 170 W and 4000 mm min^{-1}), with the beam scanning perpendicular to the laser scanning direction, and parallel to the build-platform. However, this average does not provide information on the exact location of the crystalline areas[4] in the samples and only begins to give us clues as to which crystals these are, and in which amounts. These points will be discussed in the following.

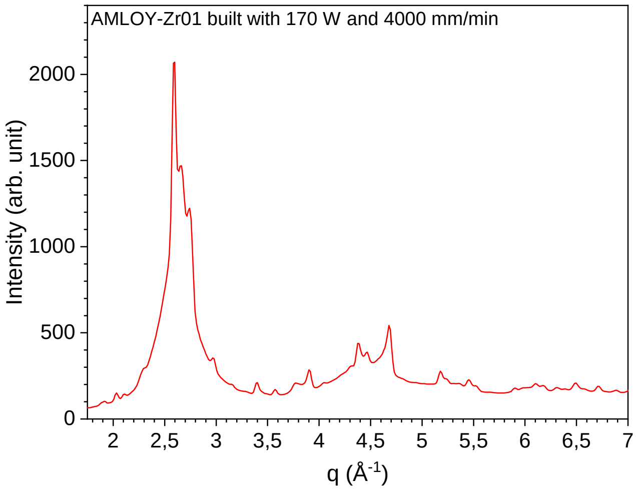

Figure 5.14: Diffraction pattern resulting from averaging the scan over the height of the AMLOY-Zr01 sample built 170 W *and* 4000 mm min^{-1}. *Sharp peaks are visible, indicating crystalline content.*

5.3.1 Location of the crystalline regions

The average shown in 5.14 hides a periodic variation that was first partly visible in SEM micrographs, as shown in fig. 5.15a. However, depending on where one interrupts the polishing process (see fig. 5.15c), a different picture could appear. This is evidenced in figs. 5.15a and 5.15b which show SEM micrographs of samples built with 80 W and 4000 mm min^{-1} and 80 W and

---

[4] Though the crystalline phases in this work are of nano- or micrometre size, the areas where they are found (within an amorphous matrix) are designated by the term “crystalline areas/regions”, despite these areas being in effect only semi-crystalline.

5500 mm min^{-1}. As shown schematically in fig. 5.15c, if one were to stop polishing at the white line, one would see dark lines in SEM at the white arrows' location – like in fig. 5.15b, while the black line could be where the polishing was interrupted for the cross-section in fig. 5.15a. Therefore, the samples were not only polished perpendicular to the laser scanning movement such as in fig. 5.15d but also brought for measurements in μXRD, where they were scanned over the build-height with a narrow beam, starting from the top according to the method discussed in section 4.2.5, producing results such as in fig. 5.16a. The variation along the main Bragg peak (in a q-range of $2.56 - 2.63\,\text{Å}^{-1}$ for AMLOY-Zr01) along the sample height is plotted for samples built with different process parameters in fig. 5.16b. A periodicity in the patterns can be observed for all the built AMLOY-Zr01 samples except the lowest energy input (80 W and 5500 mm min^{-1}). This periodicity

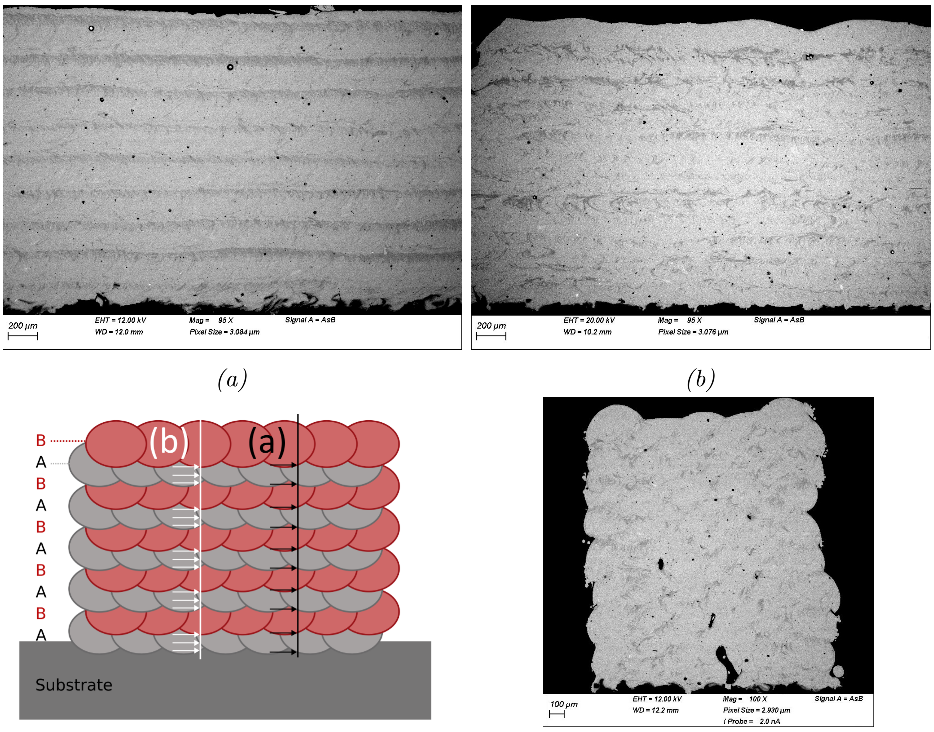

(a) *(b)*

(c) *(d)*

Figure 5.15: SEM micrographs of cross-sections parallel to the laser direction of samples with built (a) 170 W *and* 4000 mm min^{-1} *and (b)* 80 W *and* 5500 mm min^{-1} *(scale* 200 µm*, contrast increased for clarity using ImageJ). (c) Schematic representation of the A + B layer strategy, modified from section 5.2. The lines indicate planes where the polishing may have been interrupted for (a) and (b), with arrows showing the interlayer and interline regions one would see. (d) AMLOY-Zr01 sample embedded and polished perpendicularly to the laser scanning movement (scale* 100 µm*, contrast increased for clarity using ImageJ).*

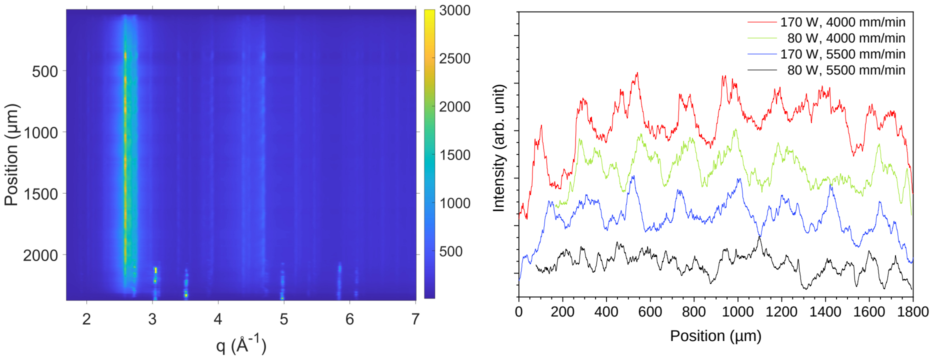

(a) *(b)*

Figure 5.16: (a) Synchrotron diffraction scan along the direction indicated in fig. 4.3a on page 36 for that same AMLOY-Zr01 sample (built with 170 W *and* 4000 mm min^{-1}*), with high intensity peaks corresponding to steel at the bottom of the sample. (b) Variation in peak intensity along the main Bragg peak (q-range of* $2.56 - 2.64$ Å^{-1}*) observed in the beam scan direction for AMLOY-Zr01 samples built with different process parameters.*

was not visible in any of the forcibly recrystallised AMLOY-Zr01 samples (maintained at 600 °C for 5 h, see examples of scan and patterns in fig. E.2 on page 110 in the appendix), meaning that it is not due to minor variations in sample thickness along the build height. When Fast Fourier Transforms are performed on the curves in fig. 5.16b using the data analysis software Origin (Version 2020b, OriginLab Corporation, Northampton, MA, USA), an approximate 200 µm periodicity is obtained.

If we take another look at the scanning strategy described in section 5.2 in fig. 5.7 on page 51, it involves the $A + B$ layering with each layer being 100 µm. This indeed leads to a spatial periodicity of 200 µm. According to the heat-affected zones (HAZ) described in section 2.3.4 on page 15, one could hypothesise that the crystallisation occurs when adding a new layer, by reheating and partly crystallising the top of the previous layer. In order to obtain a better spatially resolved view of the crystallised regions, XRD-CT was performed.

As shown in fig. 5.17a on the facing page, at the q-value corresponding to the highest Bragg peak in the AMLOY-Zr01 samples ($q = 2.57$ Å^{-1}), the intensity is mainly seen as a kind of fishnet structure in the direction perpendicular to laser scanning. This structure corresponds to the crystalline regions seen in fig. 5.15d, which also correspond to the interlayer boundaries as schematically represented in fig. 5.7. This would confirm the hypothesis of HAZ.

Additional information is provided by fig. 5.17b which shows the change in local intensity when changing q by a small amount (to $q = 2.659$ Å^{-1} from

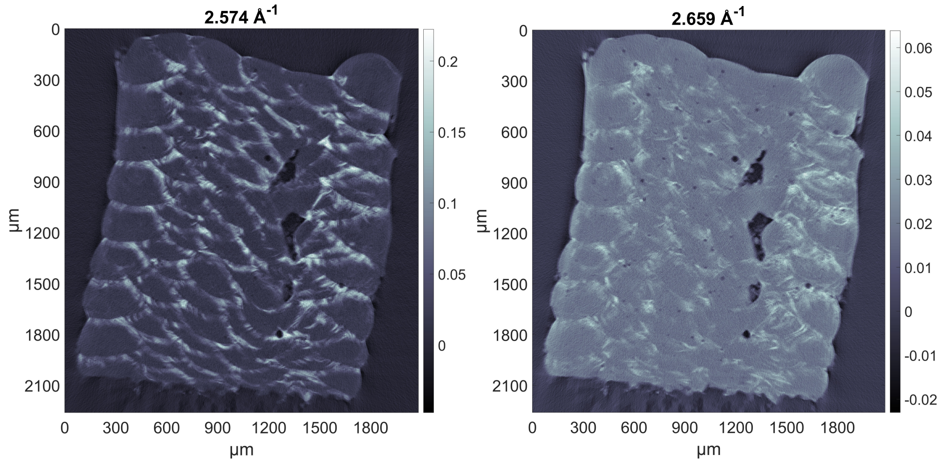

(a) (b)

Figure 5.17: Variation in distribution of crystalline fraction when changing the q-value by a very small amount ($q = 2.574\,\text{Å}^{-1}$ *to* $q = 2.659\,\text{Å}^{-1}$*).*

$q = 2.574\,\text{Å}^{-1}$ in fig. 5.17a). The highest intensity spots do not correspond one to one to those in fig. 5.17a, and generally the crystalline regions made visible at this q-value are slightly displaced downwards/away from the new layer compared to those at $q = 2.574\,\text{Å}^{-1}$. This could mean several things: there may be localised texture variations in the crystals, crystals at different relaxation states, or these could point to different crystals altogether.

5.3.2 Nature of the crystalline phases

A number of crystalline phases have been reported for additively manufactured AMLOY-Zr01: $Al_7Cu_{16}Zr_6$ ($Fd\bar{3}m$) [143, 144], $CuZr_2$ ($I4/mmm$) [115, 141, 144–147], Al_2Zr_3 ($I4/mmm$) [115], Al_3Zr_4 ($P6/mmm$) [115, 141, 147], Cu_2Zr_4O ($Fd\bar{3}m$) [74, 106, 115, 147–149], α-Zr ($P6_3/mmc$) [106] as well as CuO_X and ZrO nanoparticles [150]. Furthermore, several authors have reported quasi-crystalline structures in BMG alloys containing Ni [151], especially considering the effect of oxygen and hydrogen content on their formation [152–155]. Nevertheless, the crystallisation products most reported in the literature are $CuZr_2$, Al_3Zr_4, and Cu_2Zr_4O.

Close-ups to crystalline areas – visible in varying amounts in all samples of AMZ – are given in fig. 5.18. They are of various shapes and sizes, denoting different crystals. In fig. 5.18a, a local overview is shown: many crystal types are present closely packed. Figure 5.18b shows chains and smaller units of leafy/flowery crystals, the edges of which are well-defined. Dark star-shaped specks are seen in fig. 5.18c, of smaller dimensions than the previous crystals and possessing six-fold symmetry. Another seemingly different type of crystal is seen in fig. 5.18d: while those in fig. 5.18b have clear boundaries/edges,

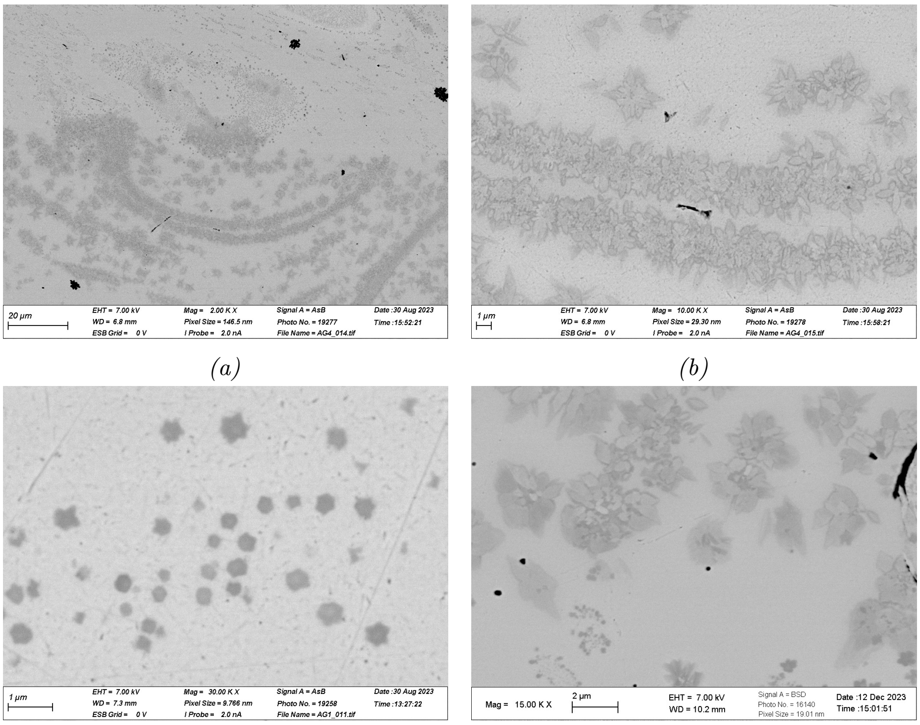

(a) *(b)*

(c) *(d)*

Figure 5.18: (a and b) SEM close-ups in a dark grey area of fig. 5.8 on page 52. (c and d) SEM close-ups of other crystals found in the regions with high crystalline fraction in different AMLOY-Zr01 samples.

these fade into the matrix, or are only faintly visible. Using EBSD in SEM, some analysis of crystalline structures could be performed. The analyses revealed the presence of $CuZr_2$ (crystals in figs. 5.18b and 5.19) and a larger crystal structure which was later identified as Cu_2Zr_4O (crystals in figs. 5.18c and 5.19) (CIF: 1220324, $SG = 227$, $a = 12.28\,\text{Å}$) using the Crystallographic Analysis of the Lattice Metric (CALM) software [156] and the Pearson crystallographic database[5]. A further crystal was matched to hexagonal Al_3Zr_4 (crystals in figs. 5.18d and 5.19). All these are coherent with the literature.

In order to gain an overview of the spatial distribution of these various crystals in the samples, a deeper look into the XRD-CT results was performed. The strongest Bragg peaks of $CuZr_2$ and Al_3Zr_4 approximately overlap, so that one must use peaks of lesser intensity for comparison (see fig. E.1 on page 109). For $CuZr_2$, $q = 2.748\,\text{Å}^{-1}$ and for Al_3Zr_4, $q = 2.649\,\text{Å}^{-1}$ were

---

[5] P. Villars, K. Cenzual, Pearson's Crystal Data: Crystal Structure Database for Inorganic Compounds (on DVD), Release 2020/2021, ASM International®, Materials Park, Ohio, USA.

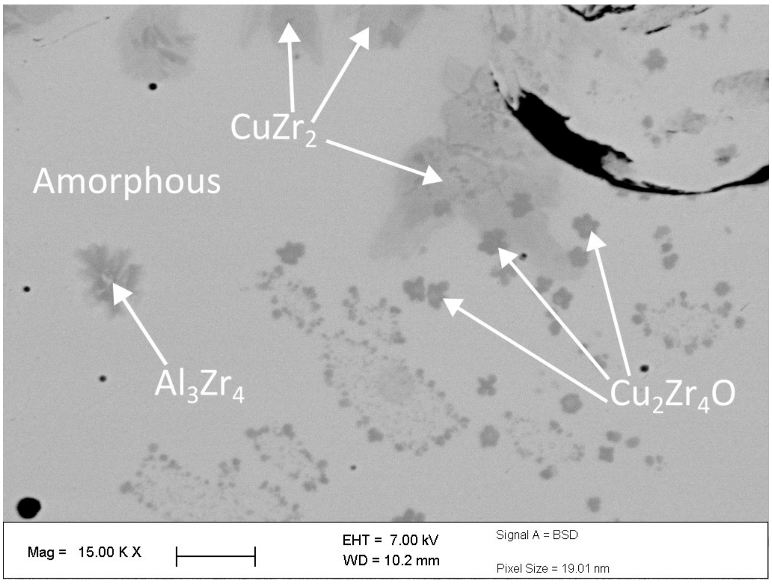

Figure 5.19: SEM of an area containing different crystals in close proximity. The crystals were determined by EBSD. The scalebar represents 2 µm

selected.

Influence of the build-platform

As the build-platform is made of steel, some mixing is expected in at least the first layer of the built samples. This is seen for example in fig. 5.20, which gives diffraction patterns over the first two and the last layer of the built sample, where the first layer displays peaks from steel, whereas the other layers do not. This was confirmed from SEM (EDX) and further XRD-CT synchrotron measurements. An example of EDX mapping is presented in fig. 5.21 on the next page. One can see that though the majority of Zr is in a different area than Fe, there is some overlap corresponding to the darker crystalline regions at the interface. SEM (EDX) and synchrotron XRD-CT measurements show that there is not only physical mixing of two phases but also formation of new crystals, though these could not (yet) be identified in EBSD. Indeed, in figs. 5.22a, 5.22c and 5.23, EDX measurements were performed on different areas represented by squares. The results are given in table 5.2 on the facing page. No Nb is detected in zone *B* of fig. 5.22b; its concentration is assumed to lie below detection range. Meanwhile, fig. 5.24 on page 65 shows that the interlayer crystalline regions (a), the steel build-platform (b), and the interface region between the platform and the built part (c) all show peak intensities at different q-values for the same sample.

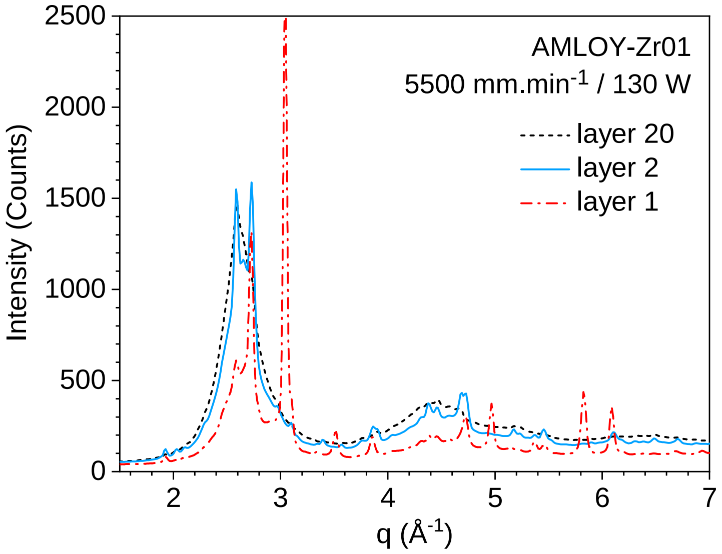

Figure 5.20: Diffraction patterns of first two and last layer of AMLOY-Zr01 built with 170 W *and* 5500 mm min^{-1}.

It is indeed shown that the influence of pure steel is visible only in the first layer, as portrayed in figs. 5.20 and 5.24 where no peaks or intensities betraying the presence of pure steel are visible in the second layer. The products of mixing between the steel plate and the AMLOY-Zr01 melt

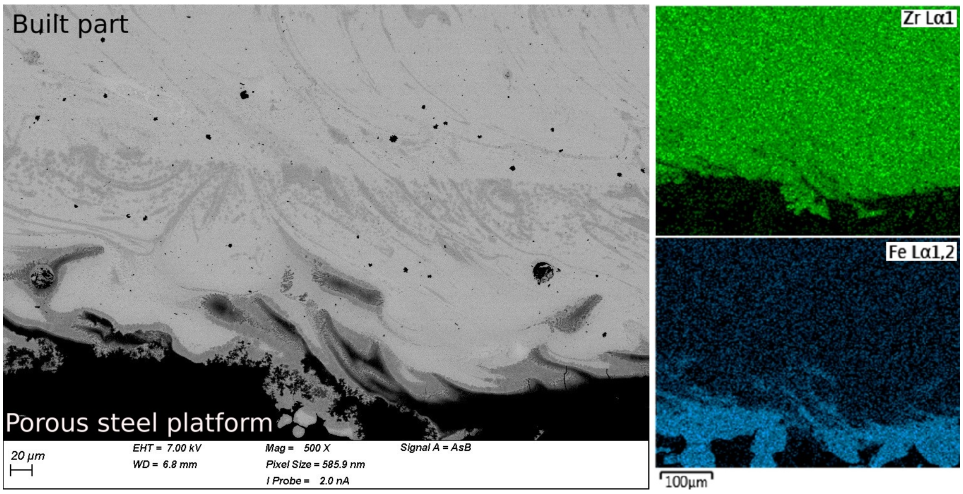

Figure 5.21: (Left) SEM micrographs of the interface region at the bottom of the sample undetached from the build-platform. (Right) EDX mappings of the region shown on the left for Zr and Fe.

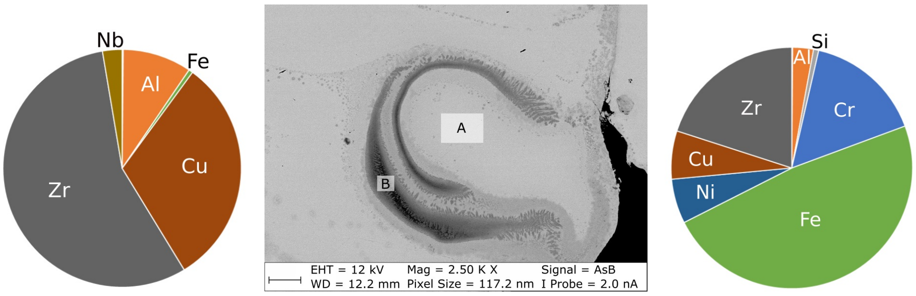

(a) *(b)* *(c)*

Figure 5.22: EDX compositional analysis results in at-% from (a) the matrix region A and (c) the dark crystalline region B, in the SEM image in (b) (the scale represents 10 µm*). The exact numerical results are provided in table 5.2.*

Region	Zr	Cu	Al	Nb	Fe	Cr	Ni	Si
A	56.1	31.2	9.3	2.6	0.6	0	0	0
B	20.0	6.5	2.8	0	48.2	15.8	6.0	0.7

Table 5.2: Measured concentrations in at-% at regions A and B of fig. 5.22b.

seem to stay within the first two layers. This allows us to ignore the compositional influence of the build-platform by ignoring the first one or two layers, depending on the energy input. Indeed, a high energy input will melt more of the build-platform into the first layer. Let us now take a look at the influence of the process parameters in general.

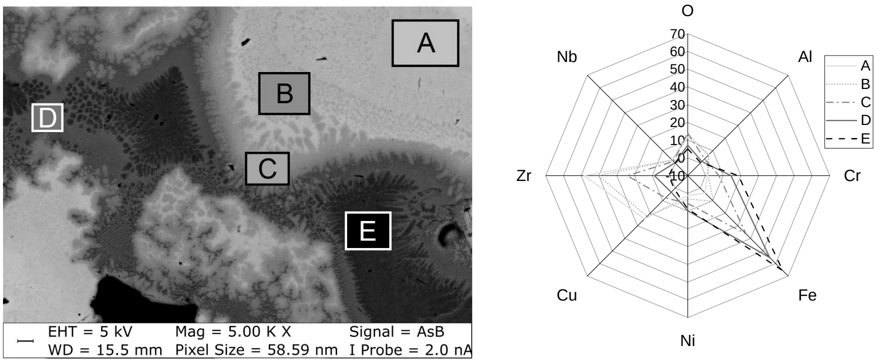

(a) (b)

Figure 5.23: (a) SEM micrograph of the interface region (scale 2 µm*) with EDX analysis represented performed over different areas, (b) at-% results at the areas marked in (a).*

5.3.3 Crystalline fractions

Process parameters are always an important part of PBF-LB. In the case of metallic glasses one might say even more so, as they affect the amorphicity of the build which has dramatic consequences on the microscopic and macroscopic properties. Therefore, investigating how the process variables affect the crystalline fraction in the final part is crucial, and this is how the optimal settings with MARS-M for AMLOY-Zr01 were chosen.

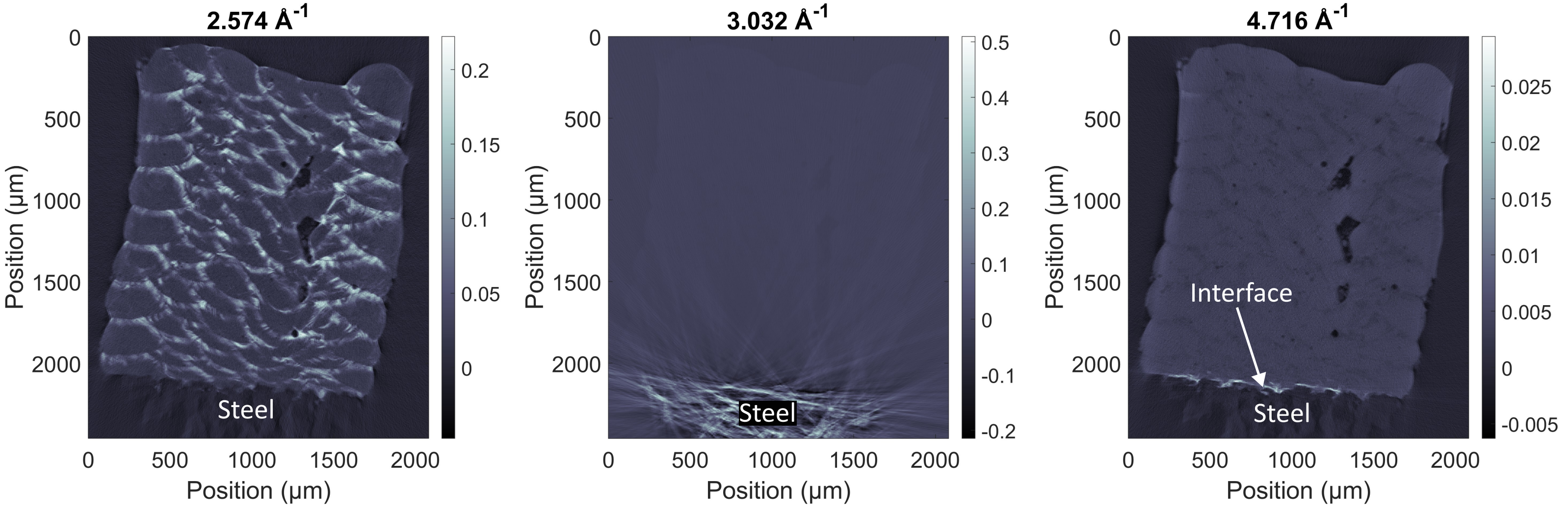

Figure 5.24: High intensities appearing at different q-values for crystallised AMLOY-Zr01, the steel platform (a piece of which is still attached to the part), and the crystals from mixing at the interface.

Influence of process parameters

Differences in the fractions of crystalline areas were first noticeable in SEM (backscattered electron detector), as seen in fig. 5.25, which compares two samples of AMLOY-Zr01 built with 170 W, one with 4000 mm min^{-1} (fig. 5.25a) and the other with 5500 mm min^{-1} (fig. 5.25b). Though both show visible darker (crystalline) lines, the ones in fig. 5.25a are more clear-cut. As mentioned in section 5.3.1, analysing the crystalline fractions in SEM depends on the embedding direction as well as the duration of the polishing. For this reason, the next samples were embedded both parallel and perpendicular to the laser direction, as shown in fig. 5.26 on the next page, which also provides a comparison with AMLOY-Zr02 for the same process parameters. The dark lines so visible in figs. 5.26a and 5.26c for AMLOY-Zr01 can only be guessed at for AMLOY-Zr02 in figs. 5.26b and 5.26d.

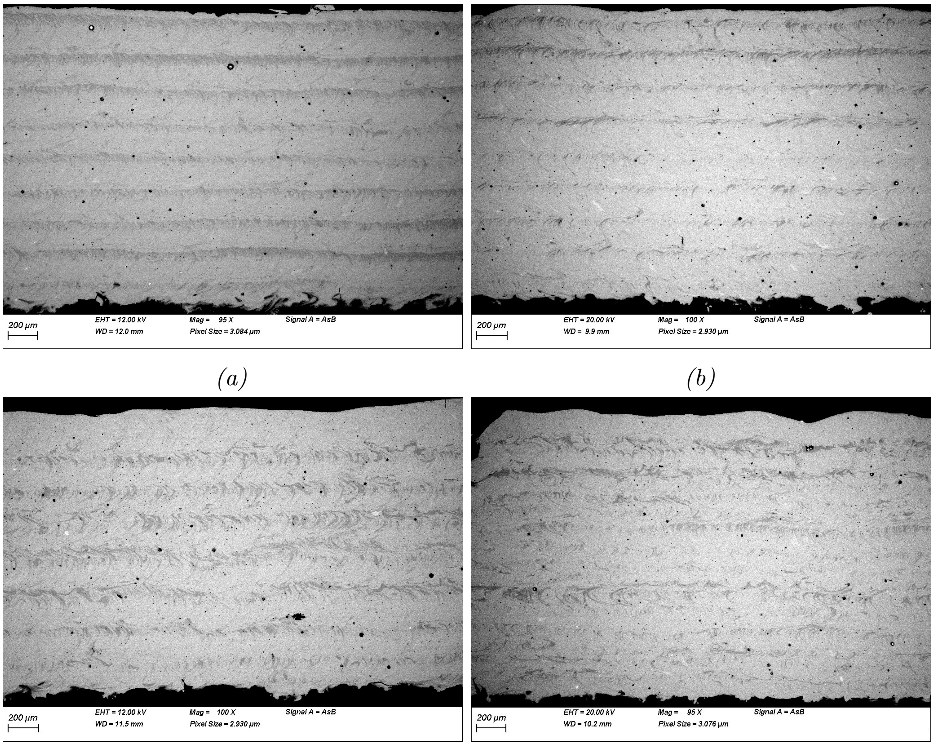

(a) *(b)*

(c) *(d)*

Figure 5.25: SEM micrographs of cross-sections parallel to the laser direction of samples with built (a) 170 W *and* 4000 mm min^{-1}*, (b)* 170 W *and* 5500 mm min^{-1}*, (c)* 80 W *and* 4000 mm min^{-1}*, and (d)* 80 W *and* 5500 mm min^{-1} *(scale* 200 µm*, contrast increased for clarity using ImageJ).*

In order to more readily quantify the varying crystalline fractions with process parameters as well as the influence of composition, other methods were applied. Synchrotron micro-diffraction was performed first, followed

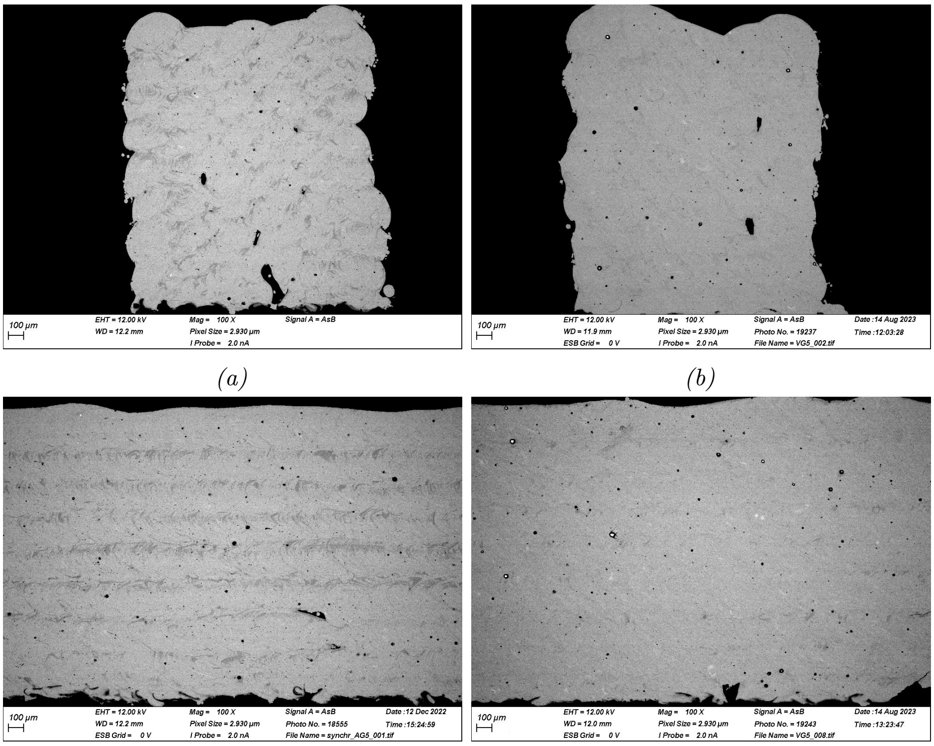

(a) *(b)*

(c) *(d)*

Figure 5.26: SEM micrographs of cross-sections of AMLOY-Zr01 (a and c, respectively transversal and longitudinal) and AMLOY-Zr02 (b and d, respectively transversal and longitudinal) built with $5500\,\mathrm{mm\,min^{-1}}$ *and* $115\,\mathrm{W}$. *A higher proportion of dark (crystalline) regions is visible in the micrographs of AMLOY-Zr01 compared to those of AMLOY-Zr02 (scale* $100\,\mathrm{\mu m}$, *contrast increased for clarity using ImageJ).*

by synchrotron XRD-CT, and finally, DSC (see methods in section 4.2 on page 32). All methods compared AMLOY-Zr01 and AMLOY-Zr02 samples built with the same parameters.

For micro-diffraction, typically plotted results are presented in fig. 5.27, each horizontal line corresponding to a diffraction spectrum like that in fig. 5.14 on page 56. In figs. 5.27a and 5.27c, some peaks from the steel platform are visible at the bottom of the plots, as parts of the platform were detached along with the samples (in the case of fig. 5.27a, the presence of steel dimmed the lesser peaks from crystallised AMLOY-Zr01, so the maximum displayed intensity was capped for clarity). This effect is not visible for AMLOY-Zr02. More vertical lines are visible in fig. 5.27d compared to fig. 5.27b, indicating higher intensity peaks, therefore more crystallisation. In order to obtain a clearer overall view, these scans were averaged over the

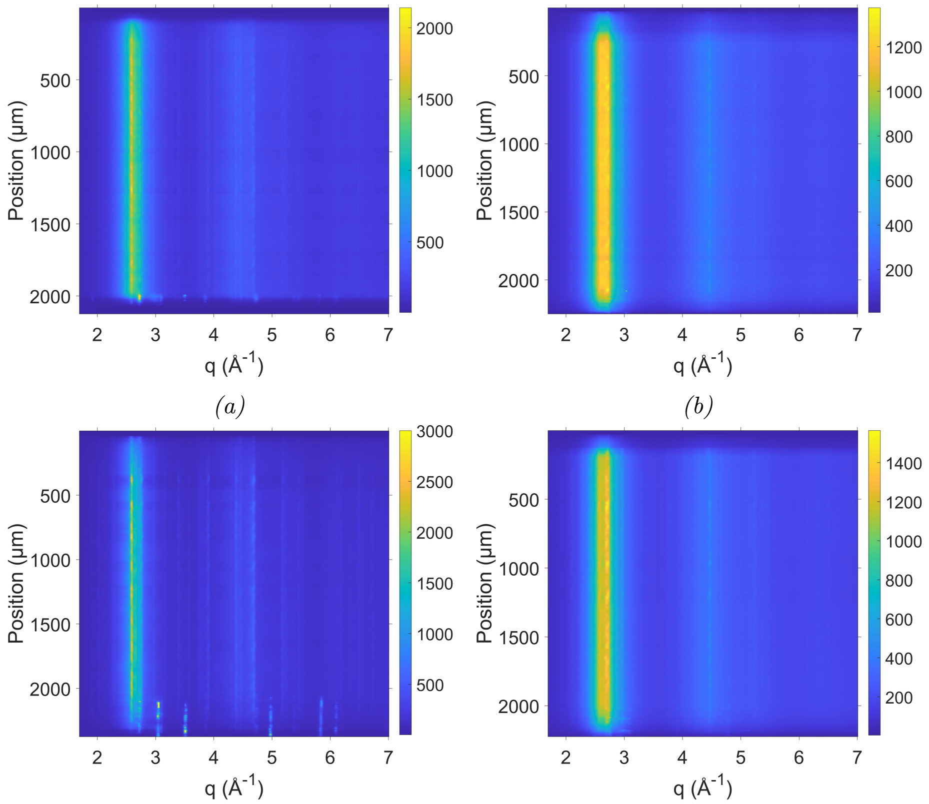

(a) *(b)* *(c)* *(d)*

*Figure 5.27: Synchrotron diffraction scans along the height of AMLOY-Zr01 samples built with (a) lowest (*80 W *and* 5500 mm min^{-1}*) and (c) highest energy density (*170 W *and* 4000 mm min^{-1}*), and AMLOY-Zr02 samples similarly with (b) lowest and (d) highest energy density. The colourbar gives the intensity in counts. The intensity was capped for (c) to render the low intensity amorphous signal more visible among the high intensity steel peaks.*

height of the samples (if steel was present, the first layer containing the steel peaks was removed from analysis), and the resulting graphs are given fig. 5.28 with the standard deviation given by the bands around the mean (middle) curve. More peaks are visible for AMLOY-Zr01, confirming the higher GFA of AMLOY-Zr02, and there is barely any visible difference between both curves of AMLOY-Zr02. The changes in process parameters affect AMLOY-

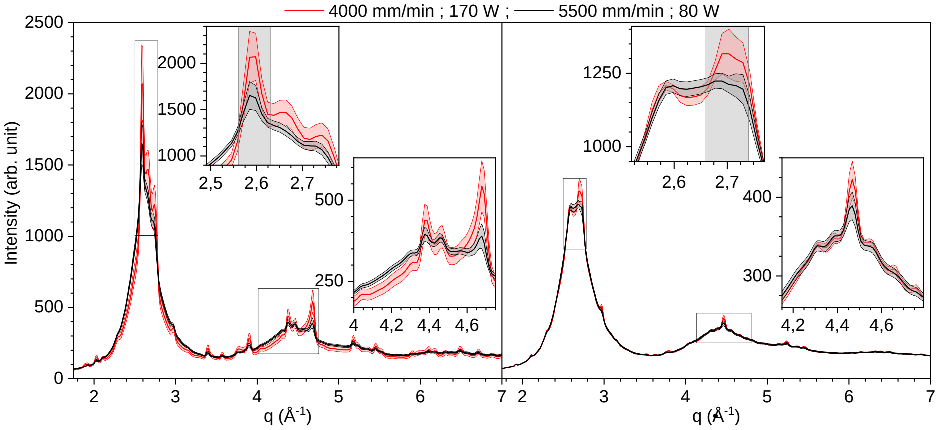

Figure 5.28: Average diffraction patterns and standard deviation from synchrotron diffraction of samples built with the lowest and highest energy density for AMLOY-Zr01 (left) and AMLOY-Zr02 (right), identical scales. The inserts show magnified sections of the curves. The greyed q-ranges indicate the ranges of interest for peak periodicity observation in fig. 5.29. AMLOY-Zr01 shows larger standard deviation as well as more and higher peaks.

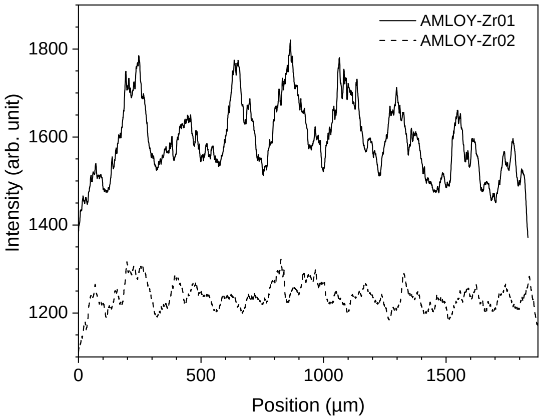

Figure 5.29: Variation along the main Bragg peaks (ranges greyed over in fig. 5.28) observed along the scan direction shown in fig. 5.16 for samples produced at medium energy input ($115\,\mathrm{W}$, $5500\,\mathrm{mm\,min^{-1}}$*) of AMLOY-Zr01 (q-range of* $2.56 - 2.63\,\text{Å}^{-1}$*) and AMLOY-Zr02 (q-range of* $2.66 - 2.74\,\text{Å}^{-1}$*).*

Zr01 more strongly than AMLOY-Zr02, while in terms of the periodicity mentioned in section 5.3.1 for AMLOY-Zr01, AMLOY-Zr02 does not display an obvious periodic variation in main Bragg peak intensity, as shown in fig. 5.29. Indeed, this higher resistance to crystallisation during the PBF-LB process is also seen in synchrotron XRD-CT, as shown in fig. 5.30. The shape or aspect of the crystalline regions in AMLOY-Zr02 looks less defined than those of AMLOY-Zr01, with the ones in AMLOY-Zr02 appearing more fluid-like. This could mean that the crystallisation does not occur at the same time during the process as for AMLOY-Zr01. There are also fewer voids – only small pores are visible, in contrast to the large voids in AMLOY-Zr01.

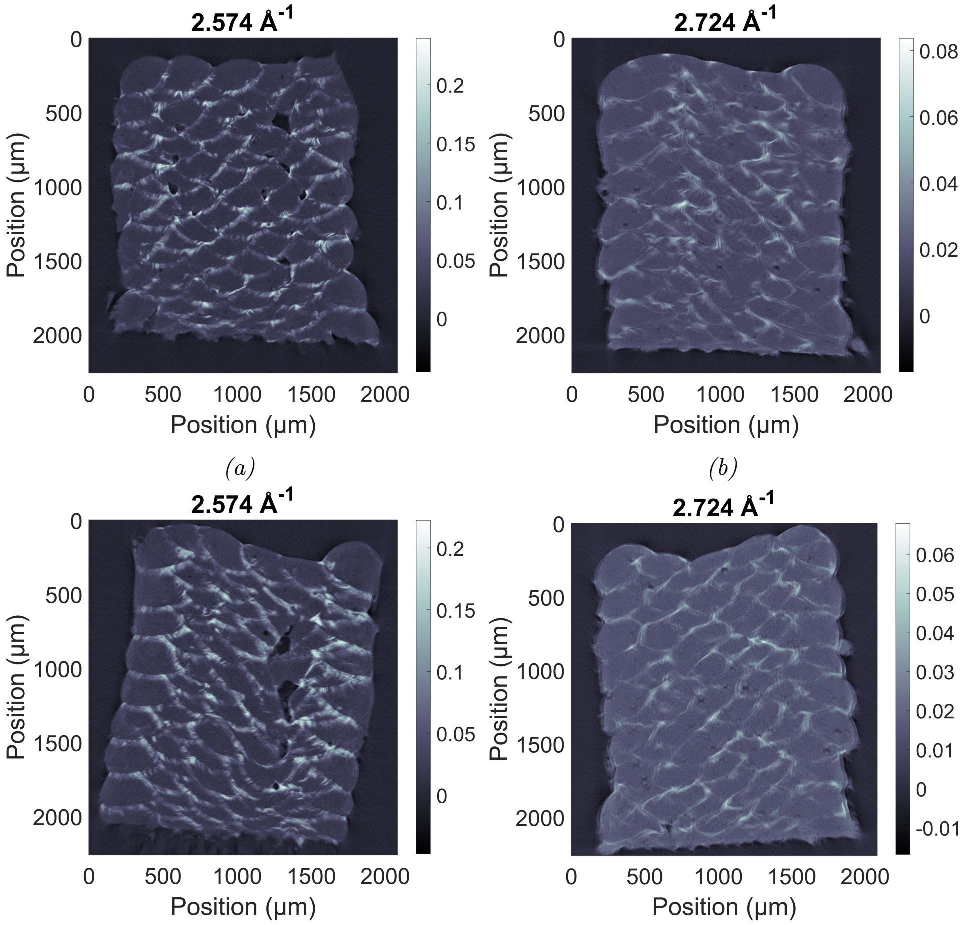

(a) *(b)*

(c) *(d)*

Figure 5.30: XRD-CT cross-sections of (a, c) AMLOY-Zr01 at $q = 2.574\,\text{Å}^{-1}$ *and (b, d) AMLOY-Zr02 at* $q = 2.724\,\text{Å}^{-1}$*, built with (a, b)* $4750\,\text{mm}\,\text{min}^{-1}$ *and* $80\,\text{W}$ *and (c, d)* $4750\,\text{mm}\,\text{min}^{-1}$ *and* $170\,\text{W}$*. The q-values correspond to the strongest peaks in the diffraction patterns for each material.*

In order to determine the amorphous ratio for each material for both sets of process parameters, two methods were used on the same samples: AMLOY-Zr01 and AMLOY-Zr02 built at 4750 mm min^{-1} with 80 W and 170 W. DSC was performed according to the procedure described in section 4.2.7. The results are provided in table 5.3 (the plots can be found in appendix E.2 on page 111.).

The results are first compared to those provided by the manufacturer in appendix A. For AMLOY-Zr01, the values provided by the manufacturer for T_g and T_x are 400 °C and 475 °C, respectively. On average, T_g of the built samples are lower by $\sim 10°$, while T_x corresponds exactly. In terms of the enthalpy of crystallisation ΔH, the manufacturer's value[6] is 47 J g^{-1}. As the measurements are performed at 20 °C min^{-1}, our data has to be divided by 20/60 K s^{-1} to compare it to this value (second line of ΔH in table 5.3). The value for the cast sample is much larger than that provided, which poses the question as to whether the manufacturer's data is comparable at all, as there is no indication of how the value was obtained. Therefore, the data for the as-cast samples are used as reference (i.e. fully amorphous value). Returning to the values of T_g and T_x, the values for the built samples are higher than those for the as-cast samples (within 3° for T_g and $\sim 10°$ for T_x). The literature on AMLOY-Zr01 provides cases for T_g of additively manufactured samples being both lower (in the work of Marattukalam *et al.* [106]) and higher (in the work of Bordeenithikasem *et al.* [21]) than of cast samples. In the work of Bordeenithikasem *et al.*, the lower T_g of the amorphous powder samples (compared to additively manufactured) is justified by the correspondence between ΔT (undercooling) and better thermal stability, so that – considering the liquidus temperature to be equal in both cast and built samples – the cast sample is more thermally stable and therefore should possess a larger ΔT and therefore a lower T_g. From a different perspective, one can also consider that in our case the built samples have experienced higher temperatures for extended periods of time due to the PBF-LB process so that some relaxation has already taken place, and therefore require a higher temperature to produce an effect on their microstructure than in the

---

[6] The manufacturer provided the enthalpy in negative value.

Sample	AMLOY-Zr01			AMLOY-Zr02		
	As-cast	80 W	170 W	As-cast	80 W	170 W
T_g (°C)	388.7	391.5	390.1	398.8	396.9	397.1
T_x (°C)	467.8	472.6	478.1	453.1	458.4	459.3
ΔH (J × K/(g × s))	21.12	14.58	13.14	19.27	17.89	17.45
ΔH (J g^{-1})	63.37	43.73	39.43	57.82	53.67	52.35
Amorph. ratio (%)	100.0	69.0	62.2	100.0	92.8	90.5

Table 5.3: Results from analysis of DSC measurements of AMLOY-Zr01 and AMLOY-Zr02 built with 4750 mm min^{-1}. ΔH *is the crystallisation enthalpy.*

cast sample. This is the case with AMLOY-Zr01 in the work of Sohrabi *et al.* [157], which compares an as-built sample with a thermally relaxed one (the last of which also contains a higher crystalline ratio). The lower T_g of the built samples is not explained in the work of Marattukalam *et al.*. Meanwhile, for AMLOY-Zr02 – using the as-cast sample as reference – T_g of the built samples are *lower* by $\sim 2°$, in opposition to what was observed for AMLOY-Zr01. If these differences are statistically relevant, this would suggest in light of the previous explanations that the built samples are more thermally stable and/or that the microstructure was frozen in quicker than in the cast sample (in a less relaxed state). More measurements would be necessary to draw more educated conclusions from the T_g values. Next, taking a look at the values of T_x and ΔH, they are observed to respectively increase and decrease in magnitude along the following order: as-cast sample, lowest laser power (80 W) sample, and highest laser power (170 W) sample. This means that increasing fractions of the samples are already in a crystalline state, as this would indeed lead to a pushing back of T_x and a decreasing magnitude of ΔH [36, 157]. This is coherent with observations in SEM and synchrotron micro-diffraction. In terms of precise ratios, when using the as-cast sample as reference, the ΔH values yield the amorphicity ratios given in the last row of the table (with $amorphous fraction = \Delta H^{sample}/\Delta H^{cast}$). As expected from SEM and synchrotron diffraction, AMLOY-Zr01 samples have higher ratios of crystalline phases than AMLOY-Zr02, and a higher laser power leads to a higher crystalline content whatever the composition.

In order to evaluate the crystalline ratios from the XRD-CT results, a threshold intensity I_{thresh} is set to examine what surface area of the sample cross-section diffracts with an intensity higher than this threshold. Because there are many Bragg peaks and that they correspond to different crystalline phases which – as we have seen above – are spread differently through the sample, it was clear that taking only one slice (i.e. one q-value) would be insufficient. Therefore, a new image was produced by overlapping two slices corresponding to the two highest Bragg peaks, i.e. each pixel of the new image receives the sum of the intensities at that pixel of the two slices[7]. As I_{thresh} is an arbitrary value, it was first set to approximately reflect the values obtained in DSC for each sample. This led to I_{thresh} values given in table 5.4 and the resulting images in fig. 5.31. In the case of AMLOY-Zr02, because the Bragg peak intensities are lower (as shown in fig. 5.28 on page 69), I_{thresh} is also lower. The values are all different, though those for AMLOY-Zr01 are close, as are those for AMLOY-Zr02. Indeed, when one calculates the ratio of I_{thresh} to the maximum intensity following the sum of the slices (*Intensity ratio* in the table), one finds that the values for AMLOY-Zr01 are equal, as are those for AMLOY-Zr02. This means that, though initially arbitrary,

---

[7] This might not suffice *alone* in determining the crystalline ratios as there are more peaks present, but it serves to confirm the DSC results.

I_{thresh} has a basis in fact and is proportional to the maximum intensity following the summing of the slices. Comparing the values of I_{thresh} to the laser powers used, one would have expected the thresholds to be higher for

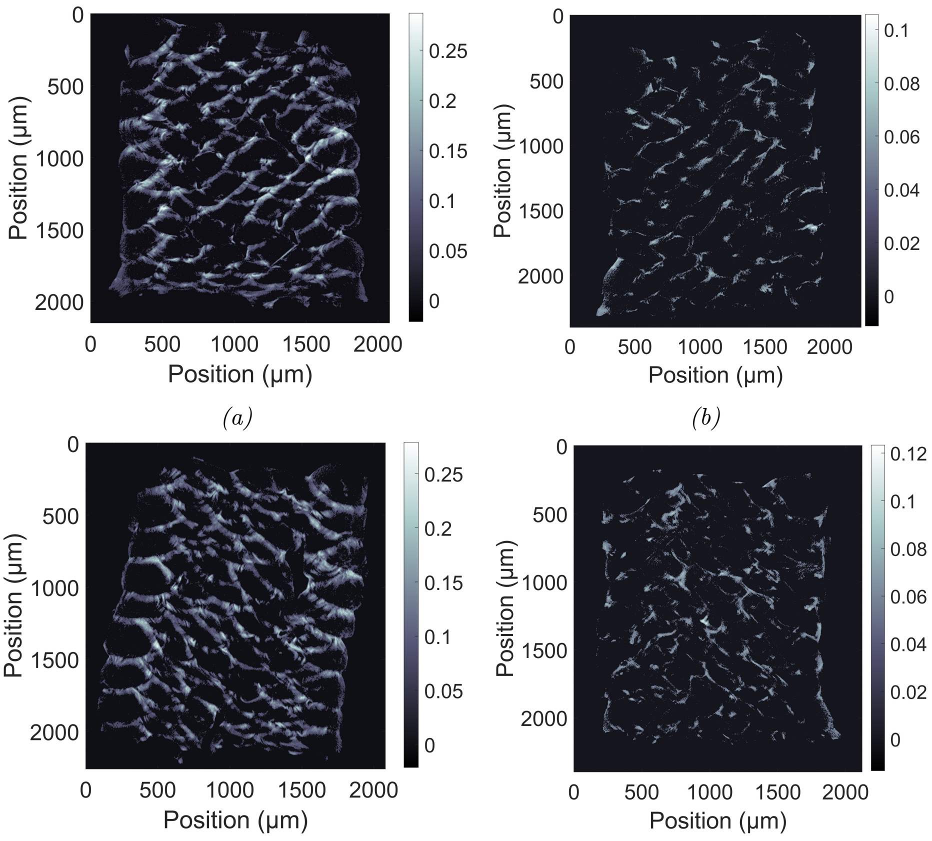

(a) (b)

(c) (d)

Figure 5.31: Comparison of filtered XRD-CT images of AMLOY-Zr01 built with 4750 mm min^{-1} *and (a)* 80 W *or (b)* 170 W*, and of AMLOY-Zr02 built with* 4750 mm min^{-1} *and (c)* 80 W *or (d)* 170 W*, only displaying pixels with an intensity above a certain threshold (see* I_{thresh} *values in table 5.4) in an effort to single out crystalline fractions. The approximate ratios of crystallinity over the sample cross-sections based on these thresholds are given in the same table.*

Feedstock	AMLOY-Zr01		AMLOY-Zr02	
Laser power (W)	80	170	80	170
Amorph. ratio (%)	69.1	62.3	92.8	90.4
I_{thresh}	0.0645	0.063	0.045	0.0495
Intensity ratio (%)	0.23	0.23	0.44	0.44

Table 5.4: Amorphous fractions as determined by threshold method on XRD-CT results for samples of AMLOY-Zr01 and AMLOY-Zr02 built with 4750 mm min^{-1}.

samples built with 170 W. However, that is only the case for AMLOY-Zr02. To explain this, attention is drawn to the particular quality of the images of AMLOY-Zr02 in figs. 5.30b, 5.30d, 5.31b and 5.31d. The images are in fact blurry compared to the images of AMLOY-Zr01 (though this is perhaps not as easily visible in print dimensions). This is explained by the fact that these samples' positions during the measurement (an image of which was shown in section 4.2.6, fig. 4.4 on page 37). Because the samples are rotated along their axis, this axis has to be as straight *as possible*. Despite the best care, the end result is not always perfectly aligned. And so, the further one moves from the fixation point, the more deviation there is. The samples were ordered in the following manner from the fixation point: AMLOY-Zr01 80 W, AMLOY-Zr01 170 W, AMLOY-Zr02 170 W, AMLOY-Zr02 80 W. Looking at the values for I_{thresh}, we notice that the height of the threshold correlates with the position along the axis. We see therefore that the threshold is dependent not only on the composition, but also on the measurement procedure itself. For this reason, though the data obtained from XRD-CT is a rich source of information, when it comes to the determination of amorphous fraction it does not – in this case – compete with DSC.

We have seen with SEM that the crystals forming are nanosized. The reason for the presence of nanocrystalline phases in the HAZ of AMLOY-Zr01 was explained by Sohrabi *et al.* (using finite element methods) in the following way: during the adding of the new layer, "the incubation time [in the previous layer] at temperatures close to the melting point is very short, but [the] cooling is not fast enough to avoid any crystallization" [107]. This is described graphically by Sohrabi *et al.* in fig. 5.32, which shows their simulation results. Compared to those described in this work, the experiments of Sohrabi *et al.* were performed at higher scanning speed (by a factor of ~ 7), lower power (60 W vs. $80 - 170$ W), narrower hatch distance (90 µm vs. 300 µm) and thinner layer thickness (20 µm vs. 100 µm). We would therefore assume that in our case the melt-pool is larger and the HAZ is deeper. While the SEM micrographs in [107] show an HAZ with a thickness of around $3 - 4$ µm[8] (see fig. 5.33a), the XRD-CT images give a thickness of the HAZ between 40 µm and 50 µm depending on the laser power used (see figs. 5.33b and 5.33c for AMLOY-Zr01 built with 4750 mm min^{-1}[9]. Therefore, we expect that reducing the energy density (i.e. increasing scanning speed and/or reducing laser power) is likely to reduce the thickness of the HAZ and the crystalline fraction of the builds.

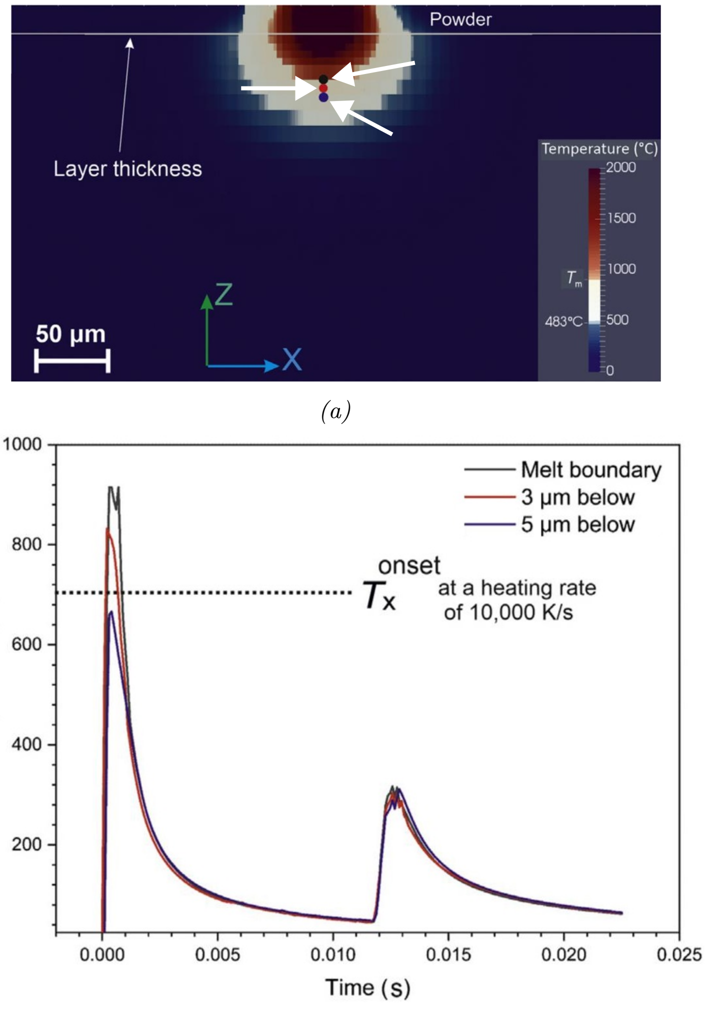

(b)

Figure 5.32: (a) Calculated thermal distribution of the built line of AMLOY-Zr01 at 30 W, 36 000 mm min^{-1}*, with a hatch distance of* 90 µm*, and a layer thickness equal to* 20 µm*. (b) Thermal history of the three points indicated by the thick white arrows in (a) (one at the bottom boundary of melt-pool, the others* 3 µm *and* 5 µm *below the first point). Modified from [107].*

Influence of voids

It became visible in CT measurements that within the same sample (built from the same powder and with the same parameters), some differences in crystallinity could be observed depending on position along the sample if there

---

[8] Though one could wonder why the authors did not choose to enlarge the HAZ to the neighbouring crystals in fig. 5.33a.

[9] The zoom location was arbitrarily chosen. However, as one can see in fig. 5.31 on page 73, the exact HAZ thickness seems dependent on the exact location in the sample.

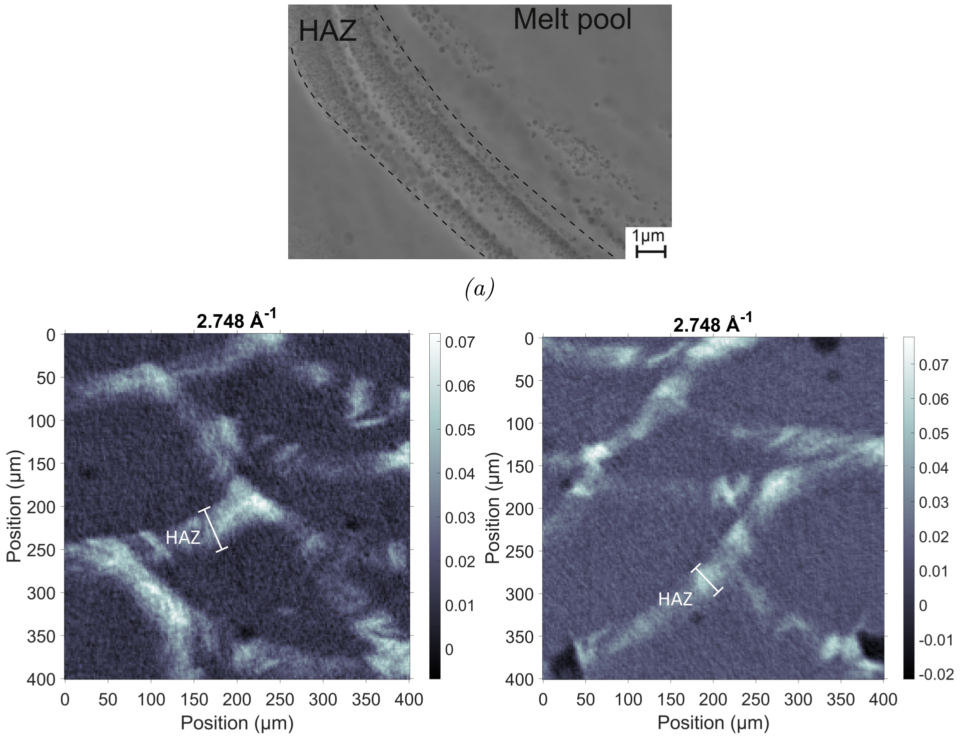

(a)

(b) *(c)*

Figure 5.33: (a) SEM micrograph showing the HAZ, modified from [107]. (b,c) Zoomed extracts of XRD-CT slices showing the HAZ at the q-value representative of $CuZr_2$ *of AMLOY-Zr01 built with* 170 W *and* 80 W*, respectively.*

are voids. This is seen in fig. 5.34 on page 78 which shows fused/overlapped slices of two different q-values at four different sections of the same sample (AMLOY-Zr01 at 170 W and $4750\,\mathrm{mm\,min^{-1}}$). In this figure, voids are clearly present – and at around the same location – but their sizes vary. There seems to be more Al_3Zr_4 ($q = 2.649\,\text{Å}^{-1}$, in red) crystalline areas when the voids are large. This could be explained by reduced thermal conductivity to the rest of the sample because of the void, and therefore a lower cooling rate, leading to increased time at higher temperature allowing increased crystallisation. The effect of voids on the amount of $CuZr_2$ ($q = 2.748\,\text{Å}^{-1}$, in blue-green) is not as pronounced. As discussed above, it seems likely that different crystals nucleate and/or grow at different moments of the process. It seems that Al_3Zr_4 forms during the creation of a line (within that same line), while $CuZr_2$ rather forms/grows at the boundary during re-heating by the next layer. This re-heating is more localised, and therefore would be less influenced by neighbouring voids.

Generally, the presence of voids decreases the repeatability of the sample production and the measurements performed later, as they seem to be at least in part due to chance (such as statistical variations in local layer thickness or porosity of the build-platform), and yet have a strong impact on the results extracted from the samples. This means that results presented are necessarily to be taken with a grain of salt (i.e. larger implicit error-bars).

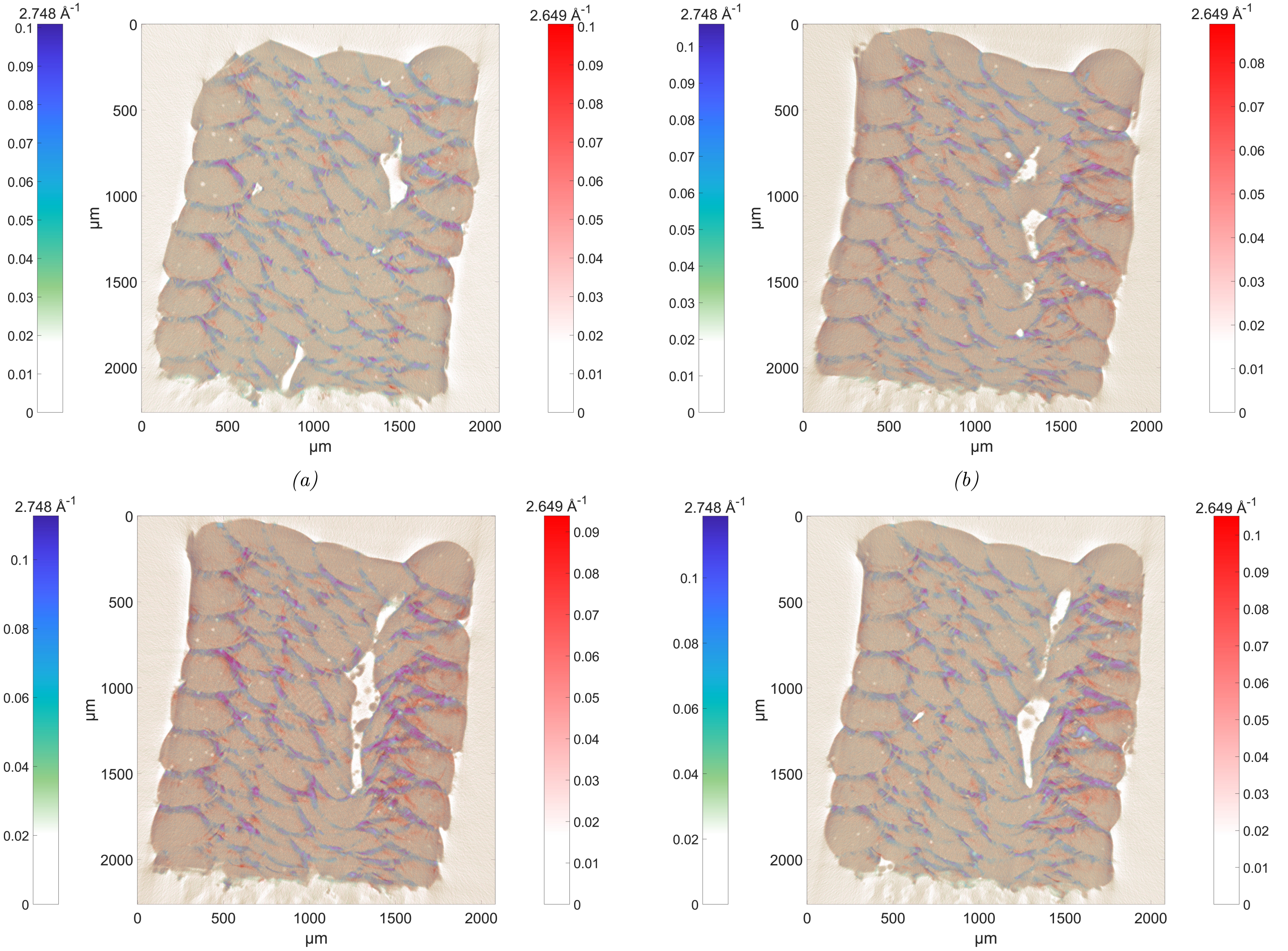

(a) *(b)* *(c)* *(d)*

Figure 5.34: Overlap of two XRD-CT cross sections of AMLOY-Zr01 built with $4750\,\mathrm{mm\,min^{-1}}$ *and* $170\,\mathrm{W}$ *at q-values corresponding to* $CuZr_2$ $q = 2.748\,\text{Å}^{-1}$ *(blue-green) and* Al_3Zr_4 $q = 2.649\,\text{Å}^{-1}$ *(red) crystalline phases.*

5.4 Influence of (micro)gravity

To observe the influence of microgravity on the microstructure, samples of AMLOY-Zr01 were produced using the same process parameters, half were built in the lab, half during MAPHEUS rocket flights. Each of the lab-samples was built within a short time of its flight-equivalent, so that the powder was in the same condition for comparability.

5.4.1 Campaign execution

The samples produced in microgravity onboard MAPHEUS are shown in fig. 5.35. Figure 5.35a shows the M11 µg-sample as first viewed after recovery of the payload. The powder-bed has noticeably left the plate and spread over the whole process chamber during re-entry, landing, and recovery. Figure 5.35b shows the M10 µg-sample, the most successful microgravity sample so far as the process did not require to be interrupted during the flight. This sample was first introduced in “Additive manufacturing of metallic glass from powder in space” [1]. The sample is thicker on the left-hand side than on the right, which could be due to the build-platform lifting up on one side in microgravity, and/or to the powder layer being unevenly spread. Figure 5.35c shows the M9 µg-sample (right) compared to the lab-sample (left). The circular parts of the pattern are absent: a software error during the flight made these sections a couple of orders of magnitude slower than intended

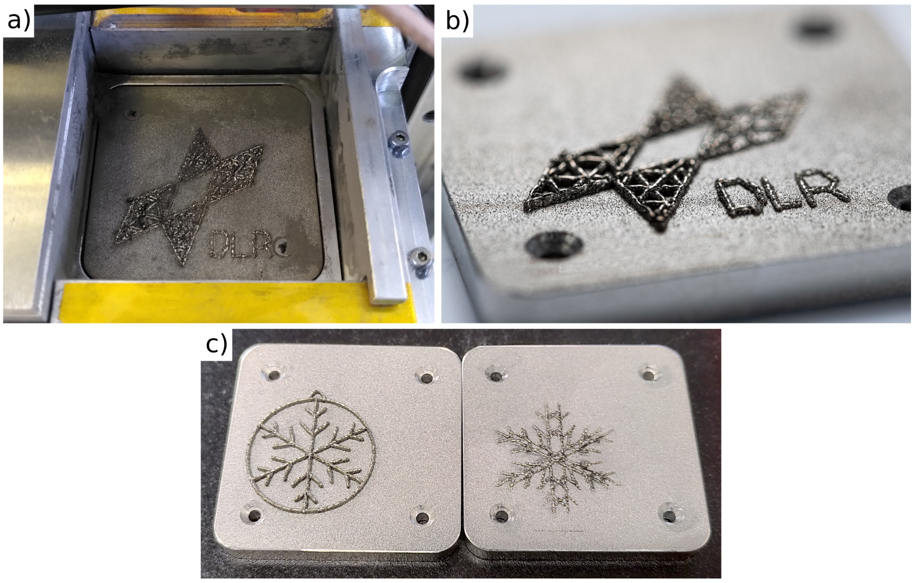

Figure 5.35: Samples produced in microgravity onboard MAPHEUS: (a) M11 µg-sample, (b) M10 µg-sample, (c) M9 µg-sample (right) compared to the lab-sample (left).

and the laser in effect did not turn on. Furthermore, the build-platform became blocked during recoating and didn't return to its original position, hence the displaced copy of the pattern.

The following characterisations were applied to the M10 µg- and lab-samples, and are under review [3].

5.4.2 Characterisation

A closer view of the M10-flight and lab samples is given in fig. 5.36. There are some differences in their appearance: the µg-sample displays more balling, originating from hydrostatic pressure and the absence of gravity of the melted alloy, most notably at the extremities of individual lines, while the lab sample is smoother in appearance and presents fewer partially melted particles on its edges.

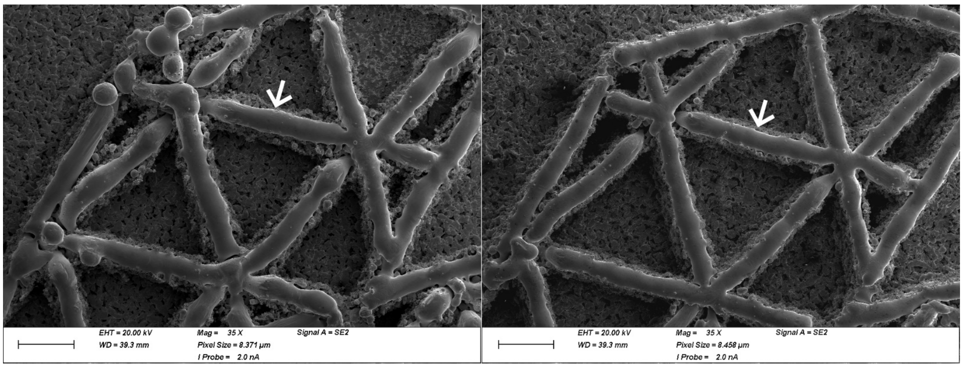

Figure 5.36: Comparison of (left) the M10 µg-sample and (right) the lab-sample. The arrows indicate where the TEM samples were extracted from.

As detaching the samples from their respective plates was not feasible (due to their thickness below one millimetre), they were placed in the synchrotron beam for micro-diffraction measurements *in transmission*, perpendicularly to the build-platform. Because of the size of the plate, the AMLOY-Zr01 lines were not easy to locate from the control room, scans were performed in different parts of the plate in order to be sure to scan across a line from the sample. An example of such scans is shown in fig. 5.37 on the facing page, while fig. 5.38 gives averaged diffraction patterns for the lab- and µg-samples for comparison. No significant difference is seen between the two samples. Therefore, at first glance we presume that for these sample dimensions neither the microgravity conditions nor the specially developed powder-handling method significantly influence the build. Both present Bragg peaks indicating crystallisation, and show a small difference in height of the amorphous broad peaks. The difference in height over the amorphous broad peaks is probably due to a minor difference in thickness, as the lab-sample is two layers thicker (i.e. approx. 200 µm). The influence of convection could have been expected,

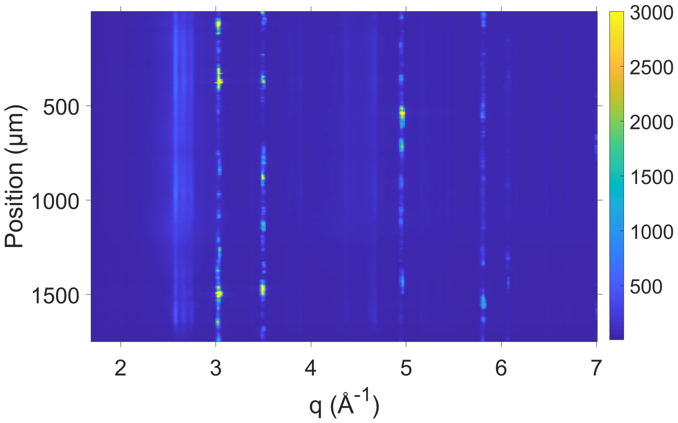

Figure 5.37: Diffraction scan over a built line of the M10-µg sample. The peaks for steel are clearly visible. Intensity was capped for better visibility of the lower intensity amorphous parts.

because it is known to impact crystallisation in metals on Earth but not in microgravity [158, 159]. However, as the cooling rates during the PBF-LB process were shown to be very high (from 10^3 to $10^8\,\mathrm{K\,s^{-1}}$ [84, 160, 161]) and that molten glass-forming compositions are relatively viscous [114], convection within the melt is supposed to be limited – in the lab and in microgravity.

As the diffraction experiments were limited by the thickness of the samples, TEM analysis was performed on lamellae extracted from the side of the M10 µg- and lab-samples (at positions marked by arrows in fig. 5.36 on the preceding page) in order to offer a more detailed analysis. The first results are shown in fig. 5.39 on page 83, bright-field examinations of both samples at the boundary region between the layers showing clusters of nanocrystalline phases of spherical or ellipsoidal morphology and well-defined phase boundaries, as well as the SAED patterns revealing significant diffraction spots next to the amorphous rings. In the HRTEM-BF images in fig. 5.40 on page 83, long-distance atomic ordered crystalline phases are visible in the amorphous, randomly ordered matrix. These therefore corroborate the findings of both SEM and synchrotron analysis. Meanwhile, no quasi-crystalline structures are detected in the extracted lamellae. The average sizes of the nanocrystalline phases in the region represented in fig. 5.39 were calculated and are given in table 5.5. The µg-sample possesses smaller nanocrystals compared to its on-ground equivalent. This is possibly due to a more homogeneous distribution of crystal nucleation under microgravity [158]. In the HRTEM-BF images in fig. 5.41a, 5.41d, and 5.41h, long-distance atomic ordering is visible in the crystalline phases while the atoms seem randomly ordered in what is considered to be the amorphous matrix. FFT and inverse FFT processing of HRTEM images of spherical particles in the

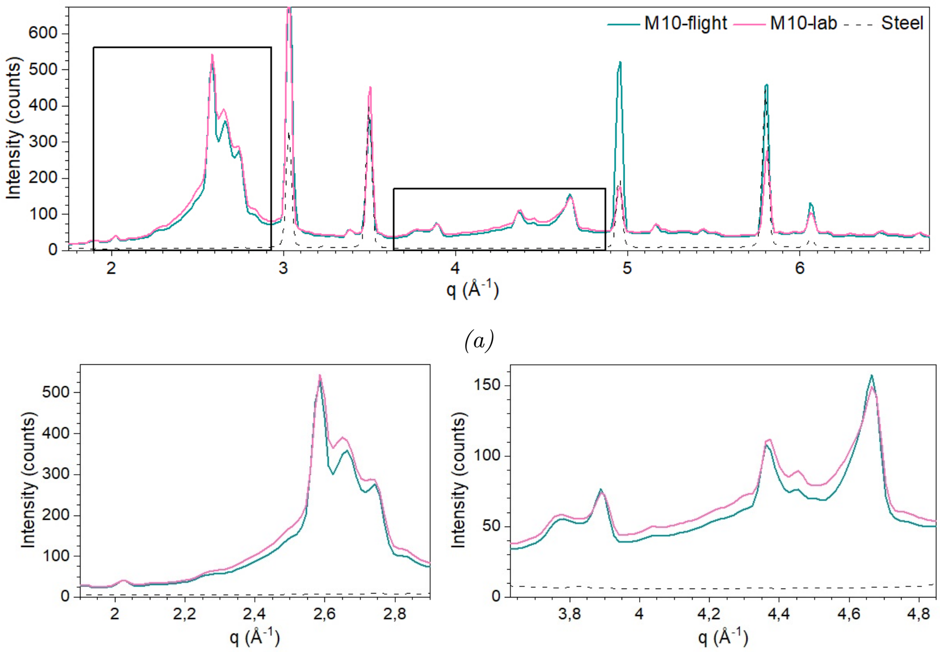

(a)

(b) *(c)*

Figure 5.38: (a) Averaged diffraction scan from the M10 µg- and lab-samples. The peaks for steel are clearly visible. The variations in steel peak intensity are due to local texture changes in the sintered porous build-platform. Intensity was capped for better visibility of the lower intensity amorphous parts. (b,c) Magnified view of sections typically of interest for AMLOY-Zr01.

		Flight Sample (nm)	Lab Equivalent (nm)
Spherical		21.12 ± 6.10	94.67 ± 25.62
Ellipsoidal	L	64.96 ± 20.86	113.40 ± 28.08
	ST	33.70 ± 10.50	68.28 ± 16.86
Ratio		1.95 ± 0.34	1.70 ± 0.38

Table 5.5: Size of nanocrystalline spherical-shaped and ellipsoidal-shaped phases observed by TEM in µg-sample and lab equivalent of AMLOY-Zr01 in nm. L is the longitudinal and ST is the short transverse measurement direction.

lab equivalent (see fig. 5.41b and 5.41c, respectively) show an FCC structure with an average d-spacing of 4.354 ± 0.533 Å (fig. 5.41c). Because the zone axis of the displayed pattern is $[\bar{1}11]$ so that the diffraction spots close to it belong to the $\{220\}$ plane family [143], an average lattice parameter of 12.284 ± 0.152 Å is determined, very probably fitting to Cu_2Zr_4O [106, 115, 149, 150, 162, 163].

As for the ellipsoidal particles in the µg-sample, FFT shows either an FCC structure in figs. 5.41e-g, or a hexagonal structure in figs. 5.41i-m. The FCC

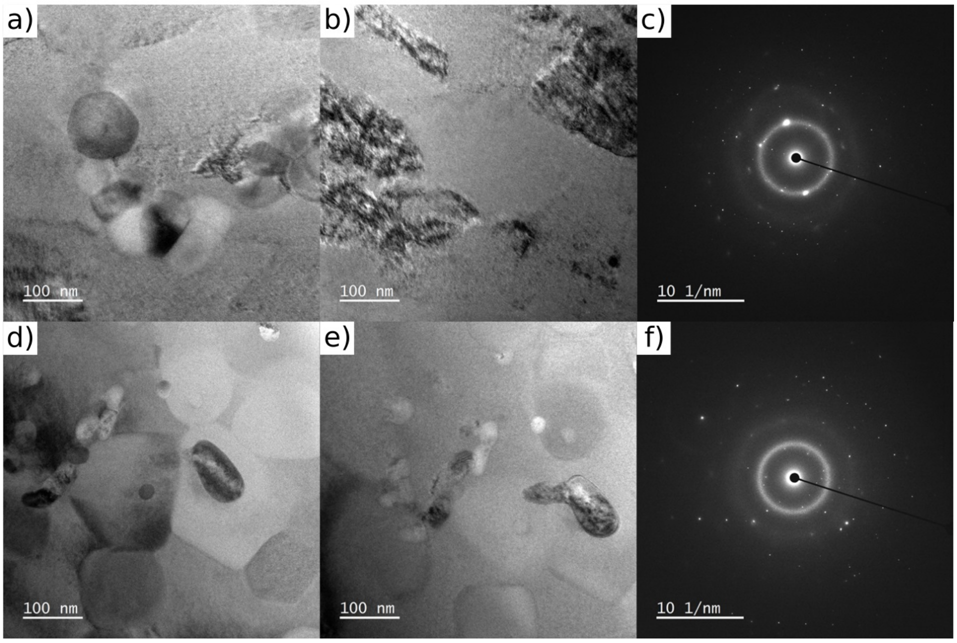

Figure 5.39: TEM-BF view and the corresponding SAED patterns of (a – c) the M10 lab-sample and (d – f) the μg-sample, at a boundary region between two layers.

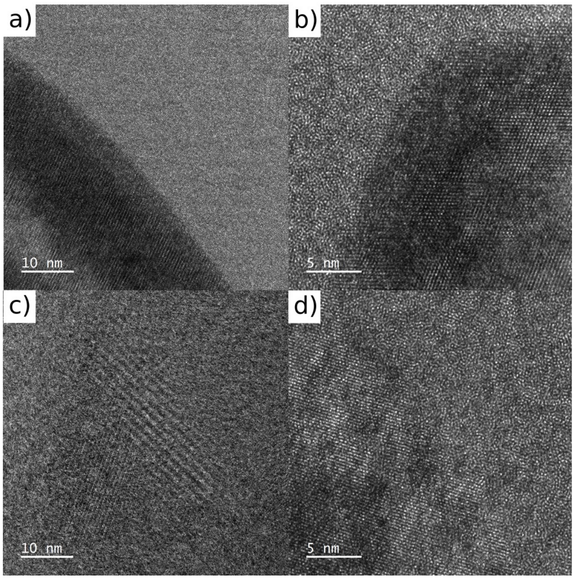

Figure 5.40: HRTEM-BF view of (a,b) the M10 μg-sample and (c,d) the lab-sample, at a boundary region between two layers.

structure does not fit to any reported cubic phase, though the local chemical composition seems to point to Cu_2Zr_4O. As to the hexagonal structure, the calculated lattice parameter c matches that of hexagonal Al_3Zr_4 [164].

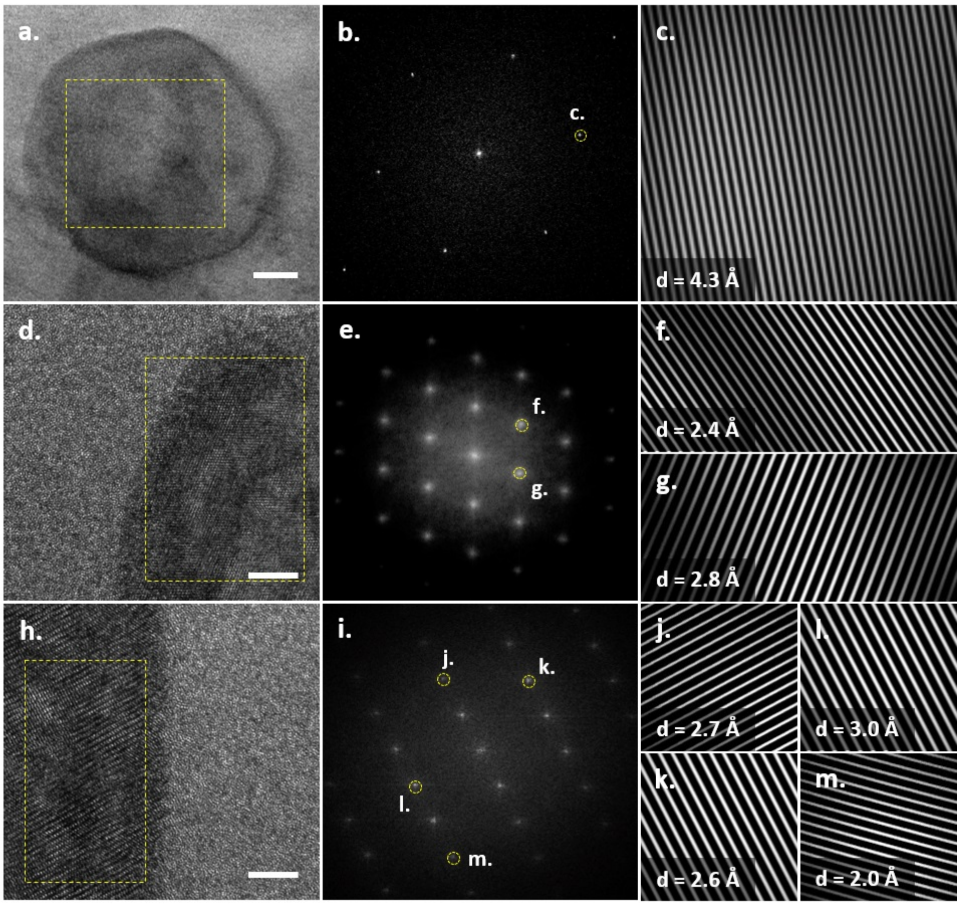

Figure 5.41: HRTEM-BF micrographs and corresponding FFT and IFFT processed images of the marked region of MAPHEUS-10 lab equivalent (a–c) and µg-sample (d–m) at the interface of two layers. The scale bar of HRTEM images is 20 nm *(a) and* 5 nm *(d,h).*

EDX mapping was then performed, the results of which are given in graphical form in figs. 5.42 and 5.43, and the local compositions of marked areas of these figures are given in table 5.6. The table indicates that compared to the nominal composition of AMLOY-Zr01 the nanocrystalline phases show a Zr depletion, but an O, Al and slight Cu enrichment, in agreement with the literature on the cubic phase Cu_2Zr_4O [115, 144, 149]. In both the lab- and the µg-sample, the amorphous matrix presents a slight Al and Zr depletion in the vicinity of the crystalline phases (column E), which is in general agreement with the work of de Oliveira *et al.* [149]. The oxygen content is slightly different between the samples, which could possibly be due to differences in the experiments themselves, though the atmosphere was flushed in the same manner. Finally, the Nb content is overall lower than expected from the original composition. Unfortunately, EDX does not

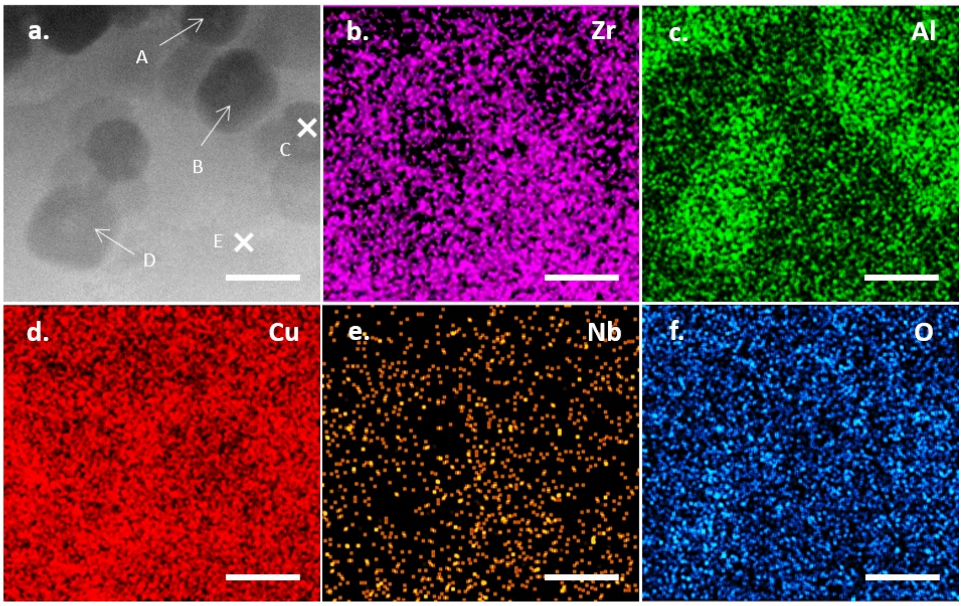

Figure 5.42: EDS maps of crystalline phases in the interface region of MAPEUS-10 lab equivalent sample of AMLOY-Zr01. Scale bar is equal to 100 nm*. Capital letters refer to local chemical composition depicted in table 5.6.*

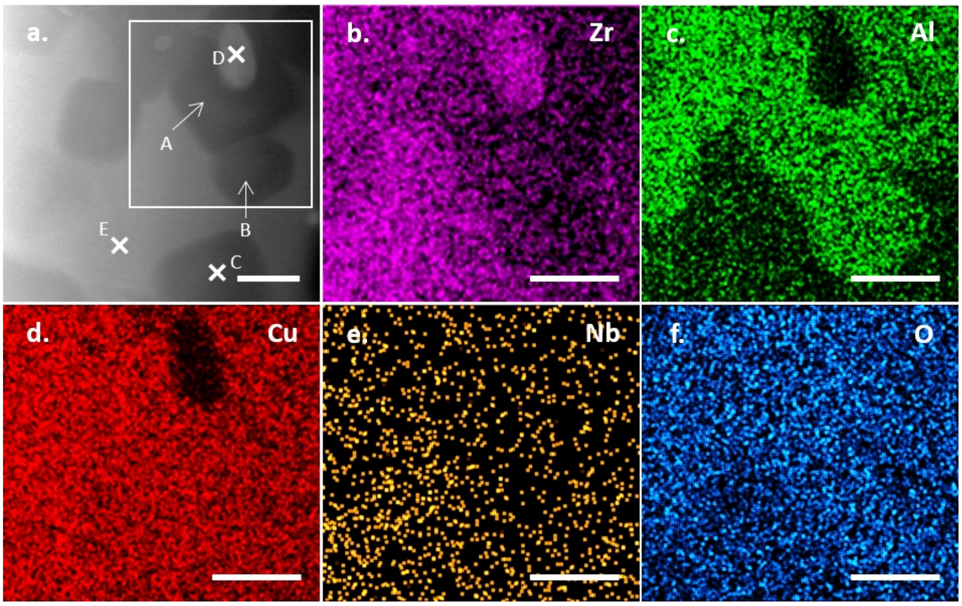

Figure 5.43: EDX maps of crystalline phases in the interface region of MAPHEUS-10 µg-sample of AMLOY-Zr01. Scale bar represents 100 nm*. Capital letters refer to local chemical composition depicted in table 5.6.*

permit a precise identification of the phases because of their size as well as

	Element	A	B	C	D	E
lab-sample	O	18.46	18.27	17.78	16.43	10.41
	Al	13.09	15.64	13.18	15.62	9.76
	Cu	31.18	32.05	31.10	32.86	29.27
	Zr	36.79	33.88	37.55	34.89	49.22
	Nb	0.49	0.16	0.40	0.21	1.34
µg-sample	O	13.97	13.64	14.02	18.84	10.29
	Al	12.39	10.05	12.81	2.65	4.45
	Cu	33.36	33.15	33.32	18.63	33.07
	Zr	39.97	39.98	40.18	59.31	50.94
	Nb	0.99	1.19	0.68	0.57	1.26

Table 5.6: Chemical composition in at. % of nanocrystalline phases and amorphous region next to it obtained from EDS spectra of the lab- and µg-sample with respect to location A-E in figs. 5.42 and 5.43, respectively.

signal overlap with the surrounding matter. Despite this, the results do seem to corroborate the literature about the Cu_2Zr_4O phase, in which a large amount of Al can be dissolved [144]. It is believed that Al substitutes Zr in its lattice sites, resulting in a wide range of reported lattice parameters from 11.9 Å to 12.28 Å [106, 115, 149, 150, 162, 163, 165], and that it also partly substitutes Cu, which was proposed by Tidefelt *et al.* for $(Al,Cu)Zr_2$ and $(Al,Cu)_3Zr_4$ [147], also resulting in an increase in the lattice constants due to the difference in atomic radii [166]. As stated by Pacheco *et al.*, thermodynamically stable phases in AMLOY-Zr01 are tetragonal $CuZr_2$ and hexagonal Al_3Zr_4 instead of cubic Cu_2Zr_4O [115]. Thus, it is possible that the detected phase is a transition state between Cu_2Zr_4O and $(Al,Cu)_3Zr_4$ due to its lattice parameter being close to those reported for hexagonal Al_3Zr_4 [164]. In the work of Tidefelt *et al.* on flash annealing of AMLOY-Zr01, the authors found that though Cu_2Zr_4O initially appeared in largest quantities compared to $CuZr_2$ and Al_3Zr_4, its fraction declined rapidly with a simultaneous increase in Al_3Zr_4(during the first tenth of a second) and $CuZr_2$ (throughout). The more oxygen was originally in the sample, the more Cu_2Zr_4O remained after stabilisation of the phase formation ($\sim$ 5 wt.% of the crystalline phase for 1.3 at.% O, vs. $\sim$ 25 wt.% of the crystalline phase for 4.3 at.% O) [147].

Though it is impossible to claim a full identification of all existing phases with TEM – especially as the analysis can only extend to a small area at a time – no definite difference could be observed with this method between the different gravity conditions in this work. However, the identification through TEM and SEM of Cu_2Zr_4O, and especially the presence of a transition region between Cu_2Zr_4O and $(Al,Cu)_3Zr_4$ suggests – corroborated by the work of Tidefelt *et al.* – that their formation is linked.

Generally, reducing the oxygen content and modifying MARS-M to allow an increase in the scanning speed seem the best routes for an improvement of the quality (in this case, amorphicity) of the final parts.

5.5 Mechanical properties

As we have seen in the previous sections thanks to SEM and synchrotron measurements, different building parameters led to different crystalline fractions. This is expected to also affect the mechanical properties, which were tested with nanoindentation.

The results obtained from nanomechanical testing are given in table 5.7 and typical indentation curves are shown in fig. 5.44a while the average hardness results are plotted in fig. 5.44b. The results are within the ranges published by Li *et al.* [22] and Marattukalam *et al.* [106], which give hardness values between 4.5 GPa and 8 GPa. In our case, there is only little variation between the samples built with 80 W, however, an increase in hardness is visible for the sample built using the highest energy density (4000 mm min^{-1} and 170 W). The crystallised product of AMLOY-Zr01 is reported as showing a higher hardness than its amorphous counterpart [22, 106, 144], so that this is an expected result, as this sample also displayed larger crystalline fraction in the synchrotron results. The lowest hardness is displayed by the sample built with 5500 mm min^{-1} and 170 W, which is a surprising result after the discussions above as one would expect it to be somewhere between the sample built with 80 W, 5500 mm min^{-1} and that built with 170 W, 4000 mm min^{-1} because of the crystalline fractions at these process parameters. There are different possible reasons for this result. Firstly, the sample surface quality (pores, scratches) as well as the preparation are very important for nanoindentation, because the surface is what is being probed: if the surface is not polished in an identical fashion for all samples, the strains induced into the surface by the grinding and polishing can vary, causing the surface to react differently to the indentation. This seems one of the two most likely sources of variation. Secondly – and the second most likely source

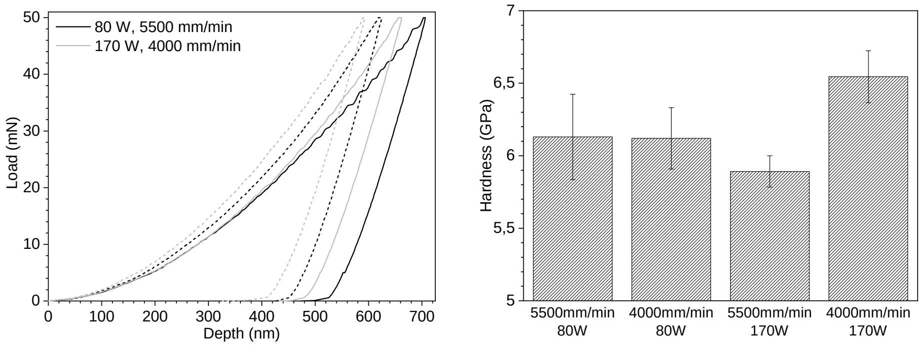

(a) *(b)*

Figure 5.44: (a) Example of load-displacement curves for the samples built with 80 W*,* 5500 mm min^{-1} *(in black) and* 170 W*,* 4000 mm min^{-1} *(in grey). (b) Average nanohardness results for varying build parameters.*

Property	Sample 1	Sample 2	Sample 3	Sample 4
Speed ($\mathrm{mm\,min^{-1}}$)	5500	4000	5500	4000
Laser power (W)	80	80	170	170
Max. depth (nm)	660.5 ± 15.0	668.1 ± 11.7	673.0 ± 5.7	640.7 ± 8.9
Contact depth (nm)	553.5 ± 13.3	553.7 ± 9.8	564.7 ± 5.4	534.6 ± 7.6
Hardness (GPa)	6.1 ± 0.3	6.1 ± 0.2	5.9 ± 0.1	6.5 ± 0.2
Reduced modulus (GPa)	105.3 ± 4.6	98.4 ± 3.8	101.8 ± 1.7	109.7 ± 3.6

Table 5.7: Nanomechanical results from nanoindentation performed on four samples built with different laser scanning speed and power.

of variation, as we have shown in previous sections, because the samples were first embedded parallel to the laser direction, the surface which is probed is dependent on where the polishing was interrupted. Thirdly, indenter shape can affect results, as the nanoscale tip wears over time and use. This should mostly be averted by regular calibration, though it has been argued in the literature that the current standards for calibration are less than satisfactory [167–169]. Fourthly, as we have seen in previous sections, the surface of these samples present alternating crystalline and amorphous regions: depending on where exactly the indentations are performed, one may probe more of one type of region that the other. In this case indents were performed over a wide area in the hope of probing all the different regions (see example in fig. 5.45), but this is also a matter of chance. In order to see which regions the measurements probed, the indents were observed in SEM, as shown in fig. 5.46. An overview of indents on a sample is given in fig. 5.45. We see that the indents span a large area over several crystalline regions, though as we have discussed above, the fact that the sample were embedded parallel to the laser direction makes the layer boundary visibility polishing-dependent. Figures 5.46a and 5.46b show that the amorphous matrix and the crystalline regions do not deform in the same way. Generally, wavelets/shear bands are visible around the indents in the amorphous region. This is coherent with the literature, as deformation of BMG during nanoindentation often

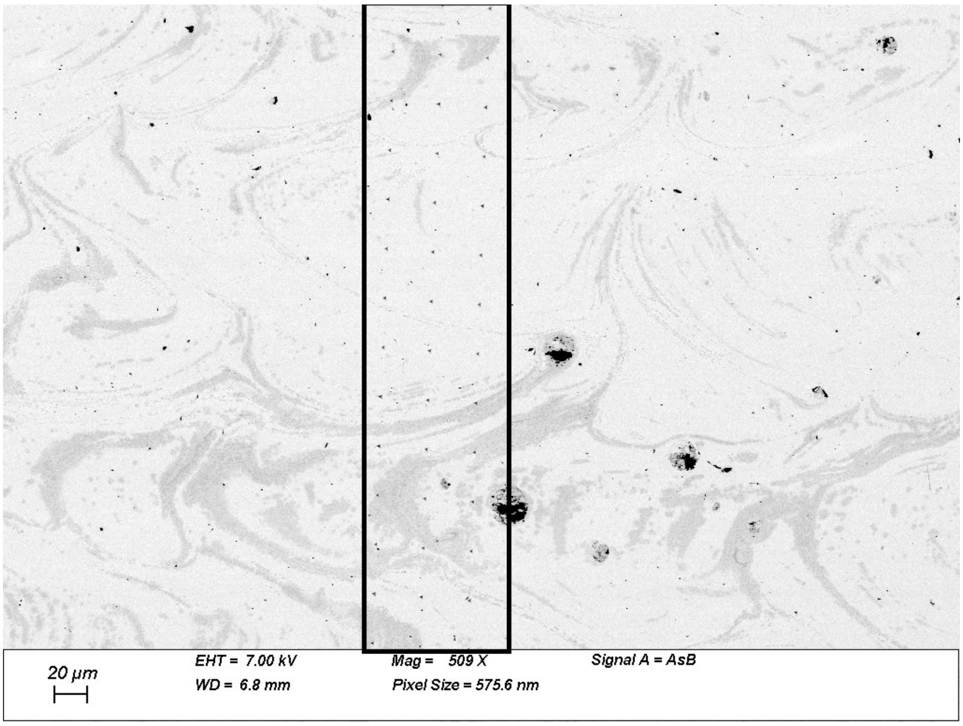

Figure 5.45: Overview of indents (in square) over the sample height.

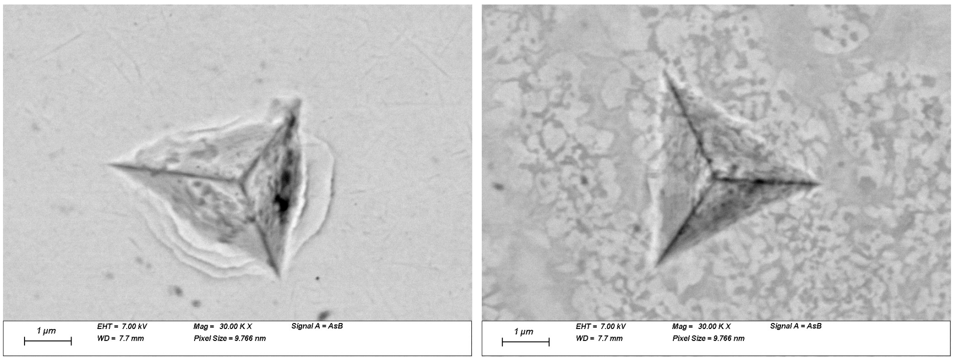

(a) *(b)*

Figure 5.46: (a) Indent in a glassy region. Deformation is visible and appears as shear bands at the indent edges. (b) Indent in a crystalline region where – unlike in (a) – deformation is not visible at the indent edges. The scale is 1 µm.

occurs through shear banding, as seen in fig. 5.47, and presenting serrated flow in the load-displacement curves [170, 171], such as the black solid curve in fig. 5.44a.

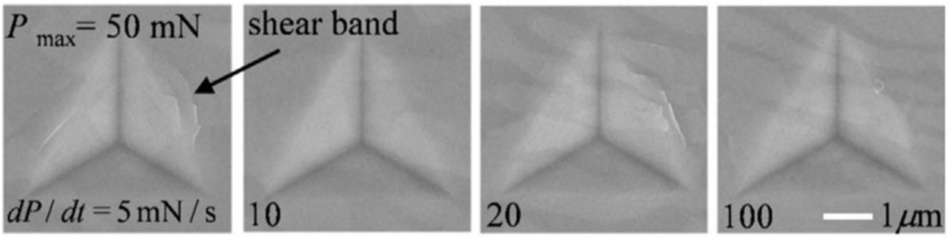

Figure 5.47: SEM micrographs of indents at different loading rates [171].

In conclusion, the mechanical results somewhat follow expectations from SEM and synchrotron analyses. The highest energy density also incurs the highest hardness (as expected from the increased crystalline fraction). The lowest energy density incurs a lower hardness, but not the lowest of all samples. This could be because of several reasons discussed above. If measurements were to be reproduced – and expanded, the samples would be embedded perpendicular to the laser direction, as discussed previously. Furthermore, a mapping such as that performed by Yang *et al.* over the HAZ (see fig. 5.48) would be of great interest in separating the mechanical properties of the crystalline and amorphous regions [144].

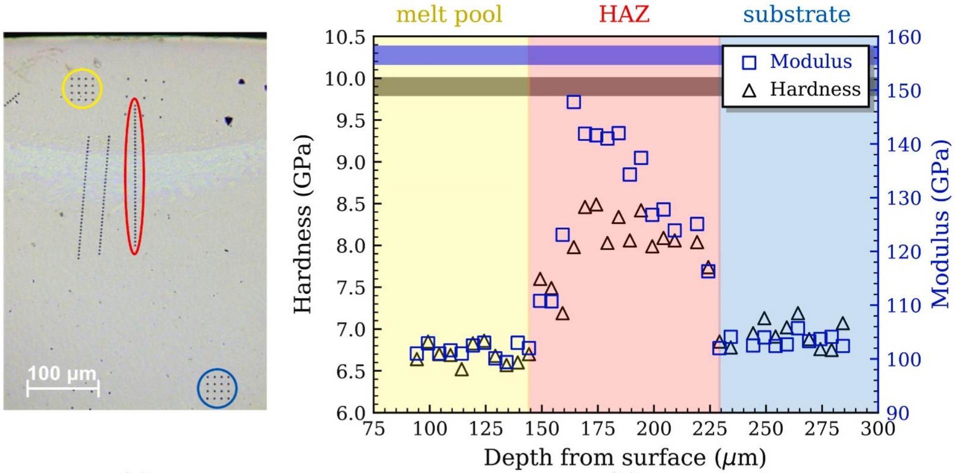

(a) (b)

Figure 5.48: (a) Nanoindents on an AMLOY-Zr01 sample. The yellow circle shows indentations performed in the melt pool, while the red ellipse shows indentations spanning the HAZ. The blue circle shows indentations on the substrate, far enough away from the melt pool and HAZ to avoid influence. (b) The hardness and modulus values along the depth as calculated from the indentations in the red ellipse in (a). At the top of (b), the shaded areas indicate the hardness (grey) of the fully crystallised sample ($9.9 \pm 0.1\,\mathrm{GPa}$*) and its modulus (blue,* $156.5 \pm 1.6\,\mathrm{GPa}$*). Taken from [144].*

Chapter 6

Conclusion and outlook

6.1 Conclusion

A first-of-its-kind device was designed and built to perform PBF-LB in space: MARS-M, a sounding rocket payload. Thanks to it, samples of AMLOY-Zr01 and AMLOY-Zr02 metallic glass were built on Earth and in microgravity onboard the MAPHEUS sounding rocket. The manufacturing process was optimised in the lab by developing a code for systematic parameter testing adaptable to a wide range of materials. This optimisation process was applied to the Zr-based BMG and the resulting samples were thoroughly analysed through SEM, synchrotron micro-diffraction, synchrotron XRD-CT, TEM, and nanoindentation, which exposed an amorphous matrix containing several different crystalline phases, the amount of which depends on the building parameters – here scanning speed and laser power, especially in the case of AMLOY-Zr01, while AMLOY-Zr02 showed less variability owing to its better GFA. The crystalline region mostly appears at the interlayer regions, as shown in SEM and synchrotron diffraction and CT. This is believed to be due to suboptimal parameters, though oxygen content is a further aspect to be improved, as revealed by the presence of Cu_2Zr_4O. The results presented have delved into the presence and origin of microstructural heterogeneities in the produced parts, exploring the complexity of the PBF-LB process applied to BMG.

This work also provides an analysis of the first ever BMG produced in space. Outside of physical appearance (especially the wetting behaviour), no large difference was observed in the microstructure between the microgravity- and lab-sample. We therefore assume that gravity – i.e. the gas flow-assisted method developed to replace it in space – does not excessively affect the PBF-LB process. As a result, we believe that with a device free of the constraint of mechanical resistance to rocket launch and re-entry, the gas flow-assisted system can be used at higher laser scanning speeds and therefore produce fully amorphous – and larger – parts. Of course, these parts will have to be lightweight structures (i.e. network / single-line structures) in order to always allow the gas-flow to pass through. A further point to be researched is how many layers this process can produce before the gas-flow is impeded by the height of the powder bed. In any case, this research is a successful first step towards the use of PBF-LB during long-term space missions.

6.2 Outlook

In the following we will look at further ideas in continuation with the work presented in this thesis.

6.2.1 Possible improvements of the process with MARS-M

First of all, some improvements to the current process are desirable.

Powder handling

Several points are considered:

- more regular characterisation of the powder oxidation or its oxygen content would be of interest,
- an improved storage of the powder is hoped to help with potential humidity and oxygen content,
- as mentioned in this work, turning the powder containers over when transporting to and from Kiruna could help delay the powder-size segregation within the containers during long transports,
- new powder recoating mechanisms are being developed and tested by Dr. Christian Neumann and Johannes Thore, in order to obtain a more even layer and less jamming of the build-platform during recoating,
- as of now, unmelted parts of the powder bed are vacuum-cleaned and discarded, whereas recycling this powder (though a challenge and research topic in itself) would help increase the sustainability (in economic and environmental terms) of this research.

Build-platform and laser scanning speed

New build-platform mechanics are being developed and tested by Dr. Christian Neumann and Johannes Thore. These aim at improving the smoothness and accuracy of build-platform movement. Increasing scanning speed without making the system too fragile for rocket flight would be of great help in building fully amorphous parts.

6.2.2 Further characterisation of samples

For the M10 µg- and lab-samples produced for this work, a possibility would be to cut through the samples to embed a cross-section for SEM, while for the typical “twinlines” samples, a more precise nanoindentation mapping of two layers would be of interest to detect more precisely the changes in hardness over the heat-affected zone.

6.2.3 PBF-LB in synchrotron beamline with MARS-X

The successful development and operation of MARS-M for PBF-LB in microgravity showed that the use of a powder bed was possible independently of gravity. This led to the concept of MARS-X (see fig. 6.1), an adaptation of MARS-M that possesses a gas-flow assisted *vertical* powder bed – which provides a larger degree of freedom and a more convenient setup for analysis in a beamline – and two openings for beam entrance and exit. This makes it ideal for observations in synchrotron and neutron beams during the melting process.

MARS-X is therefore able to perform additive manufacturing in a synchrotron beam, the objective being to obtain operando information about the structural variations happening during the building process, providing insight into the effect of process parameters not only on the phase formation but also the microstructural evolution during the process.

In the same manner as in MARS-M, the manufacturing process in MARS-X takes place in a sealed environment to ensure a low oxygen concentration for metallic samples and to avoid powder contamination. A more detailed look into the design and operation of MARS-X is available to the inquisitive reader in the appendix F on page 114. The synchrotron beam is used in diffraction (similarly to work done by Hocine *et al.* [96] and Schmeiser *et al.* [172]) instead of transmission (such as done by Leung *et al.* [91]) but what is unique about this device is that the build-platform is positioned vertically.

The first qualifying experiments were performed with AMLOY-Zr02 in synchrotron diffraction at the P23 beamline (DESY) over several days in June 2023, see figs. 6.2a and 6.2b. Measurements were carried out in diffraction geometry with an incoming X-ray energy of 18 keV, and a Pilatus 1M flat panel detector at about 350 mm downstream from the sample position, in order to ensure an accessible q-range of approx. $2.1 - 5.3\,\text{Å}^{-1}$. The beam size was set to 200 µm × 50 µm (vertical × horizontal). To achieve high enough time resolution different measurements were conducted at different sampling rates. Several types of measurements were performed: static tests in on point with observation of the effect of the laser being turned on and off (sampling rate: 0.01 s per frame i.e. 100 Hz), “hot” scans along a line where the beam “follows the laser” (in the build-platform referential) as it melts the powder bed (sampling rate: 0.005 s per frame i.e. 200 Hz), and finally “cold” scans,

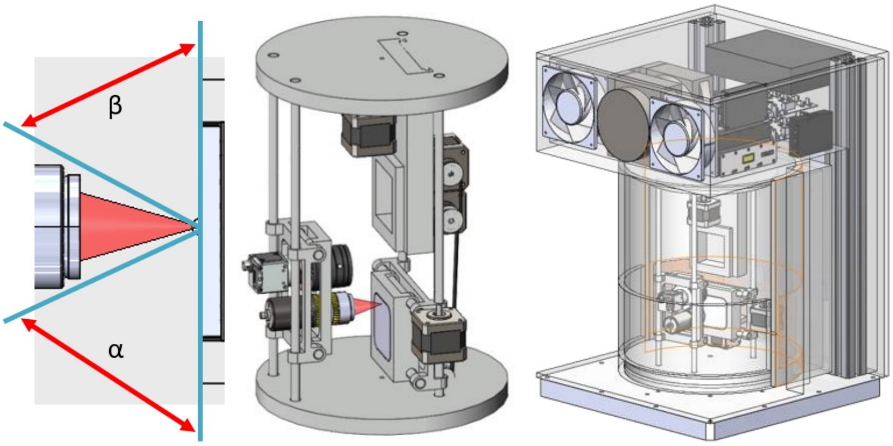

(a) (b) (c)

Figure 6.1: (a) Schematic representation of the laser beam and the vertical build-platform, seen from above – with the incoming and outgoing beam angles α and β – which is part of (b) the inner part of the device, which fits into (c) the whole setup.

which provide observations of the previously melted line after it has cooled down, with the laser being left off (sampling rate: 1 s per frame i.e. 1 Hz, 40 frames. Figure 6.2c shows a typical example of results, obtained on the powder layer melted at one point by the laser: amorphous powder state (the upper part of the plot, with peaks from the steel build-platform the powder rests on), the q values decreasing when the laser is turned on (increase in temperature), formation of new peaks, and cooling down when the laser is turned off with new peaks forming and some getting more intense. The peaks show that there are crystalline phases in an amorphous matrix and that they appear at different moments of the process: in the liquid phase when the melting is on, and during the cooling section.

A more detailed analysis will be provided in a future paper dedicated to MARS-X.

6.2.4 Further in-situ beamline experiments

Additionally, measurements with neutrons are planned to examine the residual stress in the built parts, as this will require only small adaptations to the device.

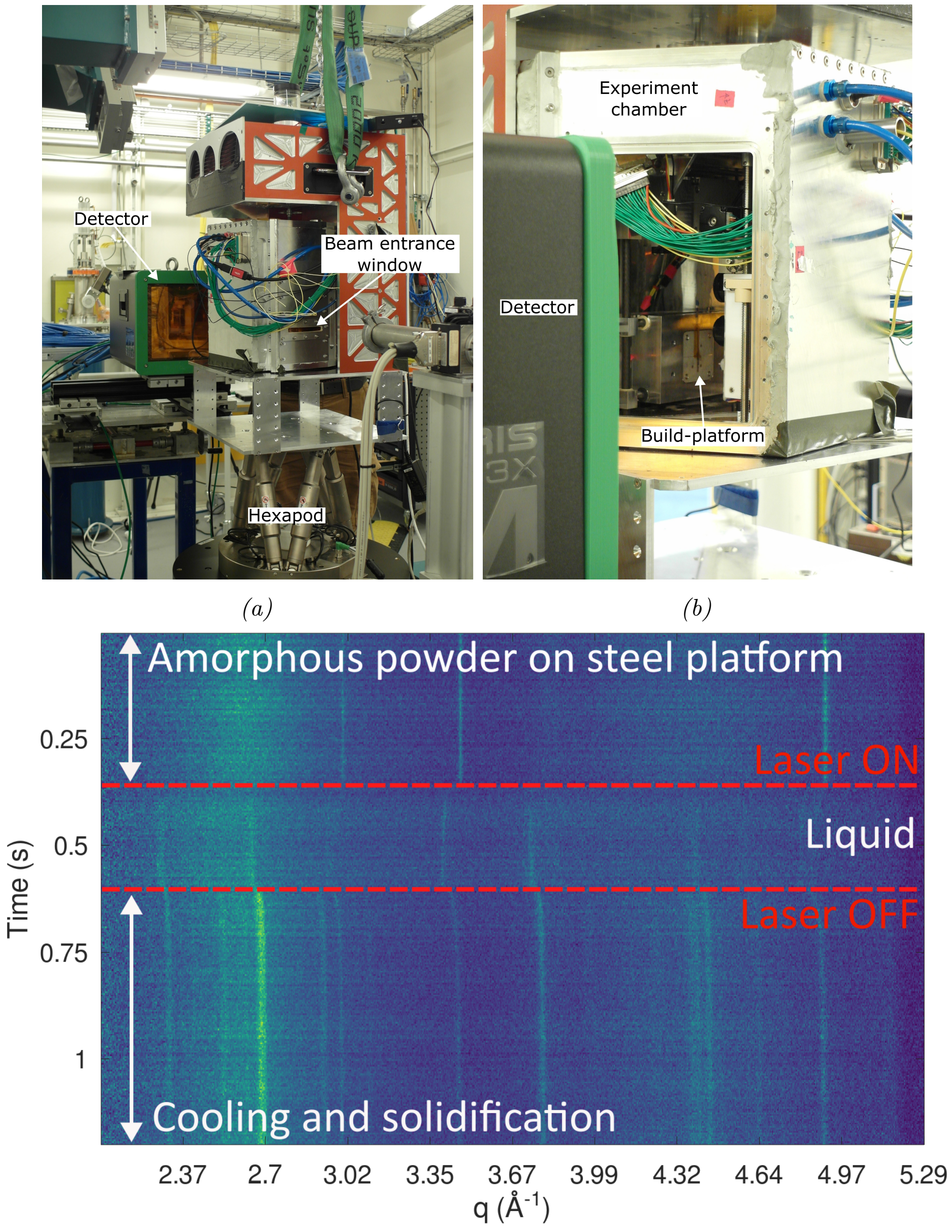

(a) *(b)*

(c)

Figure 6.2: (a) MARS-X in the beamline hutch preparing for position calibration. (b) A calibrant capillary was taped to the build-platform for position calibration. The beam output window was removed for the calibration, as no gas atmosphere was required yet. (c) Intensity variations with time as the laser is switched on then off, leading to the formation of crystals.

Appendix A

Manufacturer data for the materials

- Page 99 shows the manufacturer data for AMLOY-Zr01.
- Page 100 shows the manufacturer data for AMLOY-Zr01..

Heraeus AMLOY

AMORPHOUS ALLOYS
AMLOY-ZR01

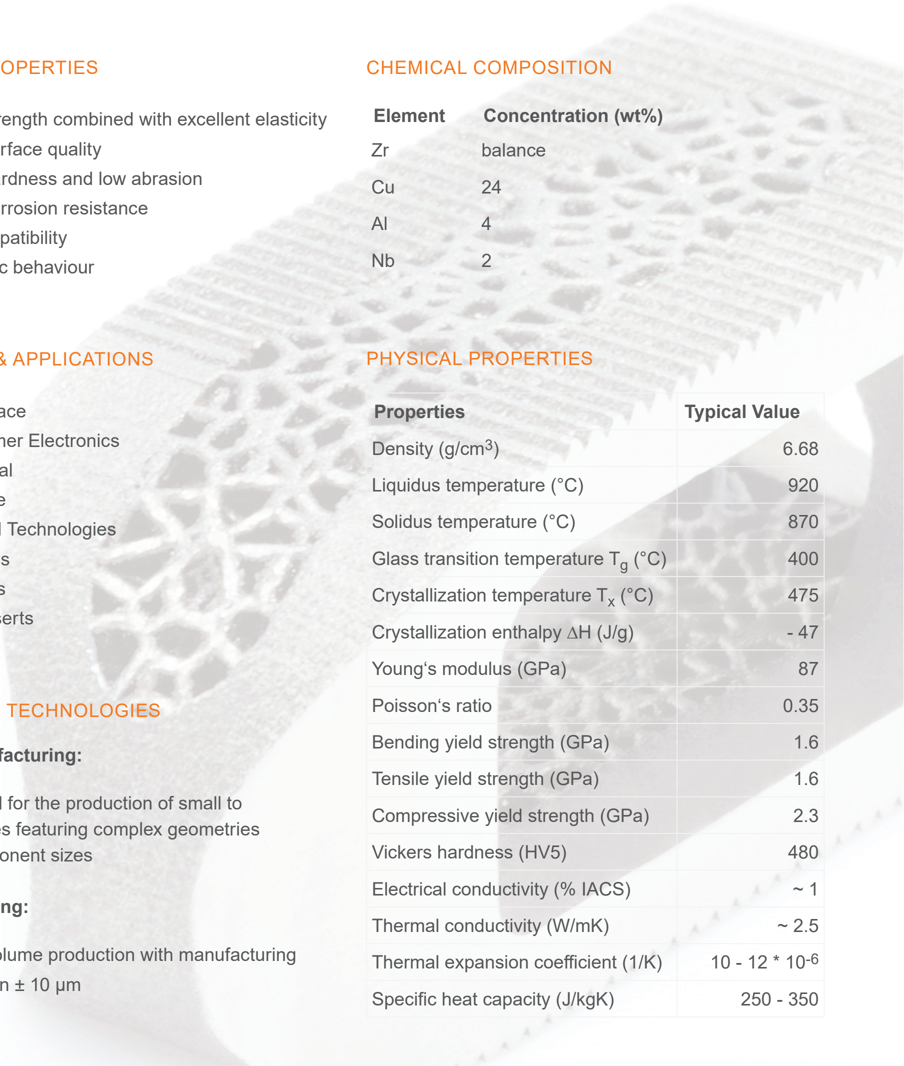

MATERIAL PROPERTIES

- High strength combined with excellent elasticity
- High surface quality
- High hardness and low abrasion
- High corrosion resistance
- Biocompatibility
- Isotropic behaviour

INDUSTRIES & APPLICATIONS

- Aerospace
- Consumer Electronics
- Industrial
- Lifestyle
- Medical Technologies
- Robotics
- Sensors
- Tool Inserts

PROCESSING TECHNOLOGIES

Additive Manufacturing:

Optimally suited for the production of small to medium volumes featuring complex geometries and large component sizes

Injection Molding:

Ideal for high volume production with manufacturing tolerances within ± 10 µm

CHEMICAL COMPOSITION

Element	Concentration (wt%)
Zr	balance
Cu	24
Al	4
Nb	2

PHYSICAL PROPERTIES

Properties	Typical Value
Density (g/cm^3)	6.68
Liquidus temperature (°C)	920
Solidus temperature (°C)	870
Glass transition temperature T_g (°C)	400
Crystallization temperature T_x (°C)	475
Crystallization enthalpy ΔH (J/g)	- 47
Young‘s modulus (GPa)	87
Poisson‘s ratio	0.35
Bending yield strength (GPa)	1.6
Tensile yield strength (GPa)	1.6
Compressive yield strength (GPa)	2.3
Vickers hardness (HV5)	480
Electrical conductivity (% IACS)	~ 1
Thermal conductivity (W/mK)	~ 2.5
Thermal expansion coefficient (1/K)	10 - 12 * 10^{-6}
Specific heat capacity (J/kgK)	250 - 350

Heraeus AMLOY Technologies GmbH
Seligenstädter Straße 100
63791 Karlstein am Main

amloy@heraeus.com
www.heraeus-amloy.com

Heraeus

AMLOY

AMORPHOUS ALLOYS
AMLOY-ZR02

MATERIAL PROPERTIES

- High strength combined with excellent elasticity
- High surface quality
- High hardness and low abrasion
- High corrosion resistance
- Biocompatibility
- Isotropic behaviour

CHEMICAL COMPOSITION

Element	Concentration (wt%)
Zr	balance
Cu	16
Ni	12
Al	4
Ti	3

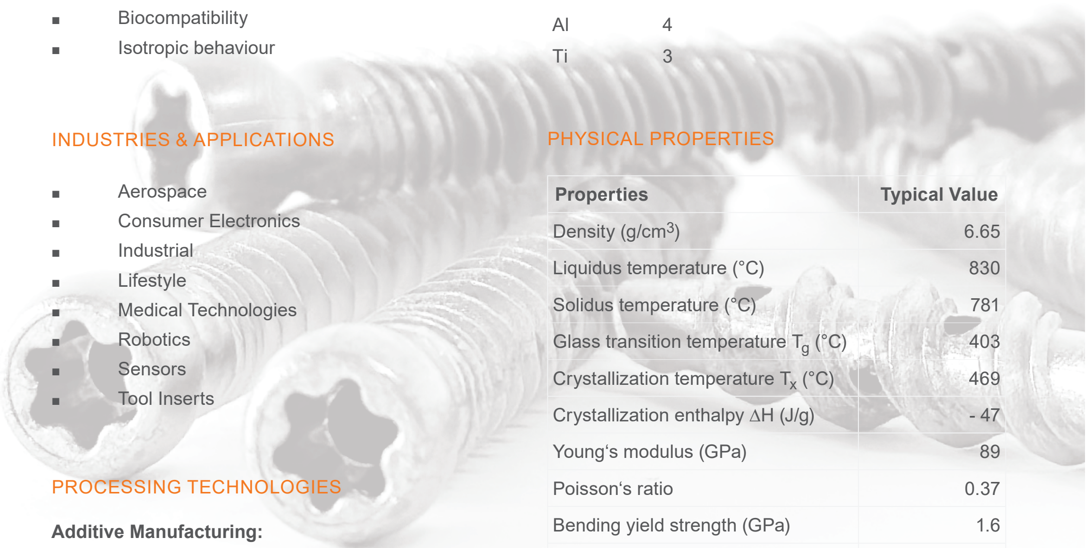

INDUSTRIES & APPLICATIONS

- Aerospace
- Consumer Electronics
- Industrial
- Lifestyle
- Medical Technologies
- Robotics
- Sensors
- Tool Inserts

PROCESSING TECHNOLOGIES

Additive Manufacturing:

The expanded design freedom of amorphous metals through 3D printing enables weight-reduced components

Injection Molding:

An automated 24/7 production process, excellent surface quality with an average roughness value (Ra) of 0.05 µm and low shrinkage of less than 0.5% are realised

PHYSICAL PROPERTIES

Properties	Typical Value
Density (g/cm^3)	6.65
Liquidus temperature (°C)	830
Solidus temperature (°C)	781
Glass transition temperature T_g (°C)	403
Crystallization temperature T_x (°C)	469
Crystallization enthalpy ΔH (J/g)	- 47
Young‘s modulus (GPa)	89
Poisson‘s ratio	0.37
Bending yield strength (GPa)	1.6
Tensile yield strength (GPa)	1.7
Compressive yield strength (GPa)	2.3
Vickers hardness (HV5)	540
Electrical conductivity (% IACS)	~ 1
Thermal conductivity (W/mK)	~ 2.5
Thermal expansion coefficient (1/K)	10 - 12 * 10^{-6}
Specific heat capacity (J/kgK)	250 - 350

Heraeus AMLOY Technologies GmbH
Seligenstädter Straße 100
63791 Karlstein am Main

amloy@heraeus.com
www.heraeus-amloy.com

Appendix B

G-code commands

G0 X[0..32] Y[0..45] Z[0..17] E[0..50] F[0..6000]

Moves respective axes from actual position to given coordinates in a straight line. Uses velocity F, given in $\mathrm{mm\,min^{-1}}$. X and Y move laser head, Z moves build plate, E is used for powder recoating, with values in mm.

G1 X[0..32] Y[0..45] Z[0..17] E[0..50] F[0..6000] S[0.2 .. 1]

Same as G0, but with laser power set to S, given in percentage of maximum power. Lower than 0.2 does not reliably emit any power from the laser module in use.

G2 X[0..32] Y[0..45] I[0..16] J[0 .. 22.5] F[0..6000] S[0.2 .. 1] (G3)

Same as G1, but doesn't go in a straight line, but on a circular perimeter from actual position to coordinates X and Y, with centre at coordinates I and J given in relative commands to actual position. G2 travels clockwise, G3 counter clockwise.

G4 S[0..∞] P[0..∞]

Pauses process for S seconds, or P milliseconds

G28 X Y Z E

Moves the axes listed into reference position at respective position switch. Homes all axes if no argument present.

G92 X[0..32] Y[0..45] Z[0..17] E[0..50]

Overrides the current position information without moving the axes.

M84

Disables all stepper drives, prevents waste heat when used at the end of the lasering of each layer, as well as the end of powder application and end of file.

M114

Returns current positions of all axes.

Machine-specific commands:

M106 S[127..255] (M107)

Enables gas pumps and sets pumping speed at S, by 8 bit proportional. For values lower than 127 the pumps do not start. M107 disables gas pumps.

M132 S50 (133)

Enables the output of a rectangular waveform for the piezo actuator. The frequency can be tuned in the configuration file, it is adjusted to the Eigenfrequency of the reservoir, and the duty cycle is usually 50 %. M133 disables the piezo waveform.

M134 (M135)

Enables an output for counting input to the data recorder. May be used for counting layers, or to indicate progress in running the code. To be followed by M135.

M600 Pauses process until begin-of-microgravity signal is received. This signal is generated by the MAPHEUS service module, M601 does an override.

M907 X[0..2] Y[0..2] Z[0..2] A[0..2] Temporarily overrides current settings for stepper drives from configuration file. Used to reduce current when axes are not in use.

“Play /sd/filename.gcode”, “Progress”, and “Abort” are valid commands too, and self-explanatory.

Appendix C

GranuDrum measurement results

- Page 104 shows GranuDrum measurement results for AMLOY-Zr01.
- Page 105 shows GranuDrum measurement results for AMLOY-Zr02.
- Page 106 shows GranuDrum measurement results for Stainless steel 316L.

GRANUDRUM™

GranuDrum Measurement Report

Sample name:0093W_AmloyZR01
Sample group : DLR

User name: user
2022.11.22 17:15:38

Analysis parameters :

Mode : Speeds Sequence
#Frames : 20
Sampling [ms] : 1000

BWThreshold : 94
CropRatio [%] : 10
Frame [pixels] : 972x972

Powder information :

Volume [ml] : 50
Weight [g] : 176
Temperature [°C] : 22,1
Hygrometry [%] : 25,00

Speeds Sequence

	Sequence	
RPM	**Angle**	**Cohesion**
2	47,9	34,2
4	48,8	38,1
6	55,9	41,5
8	51,2	42,4
10	54,8	44,2
12	51,9	44,1
14	54,8	45,7
16	54,7	41,0
18	56,6	50,5
20	50,6	35,5
40	55,7	41,4
60	50,4	68,5

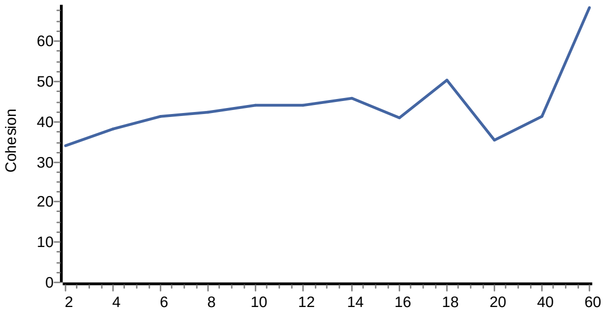

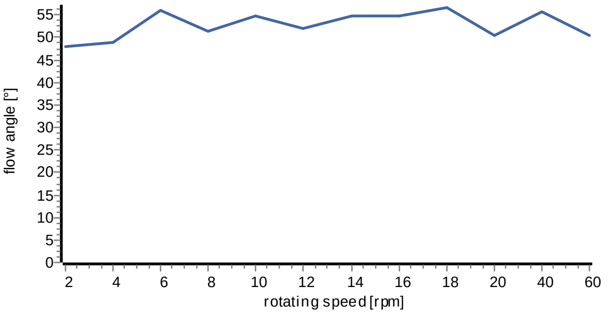

Operator notes: 93W Amloy ZR01 14-45µm

Date and signature of the operator:

GRANUTOOLS™

GranuDrum Measurement Report

Sample name : 0092W_Vit105AmloyZR2
Sample group : DLR

User name: user
2022.11.22 16:54:38

Analysis parameters :

Mode :	Speeds Sequence	BWThreshold :	94
#Frames :	20	CropRatio [%] :	10
Sampling [ms] :	1000	Frame [pixels] :	972x972

Powder information :

Volume [ml] :	50
Weight [g] :	189
Temperature [°C] :	22,1
Hygrometry [%] :	25,00

Speeds Sequence

	Sequence	
RPM	**Angle**	**Cohesion**
2	36,3	23,1
4	37,8	22,1
6	35,7	28,6
8	40,8	25,7
10	33,8	27,2
12	35,5	27,1
14	42,0	27,8
16	41,5	30,7
18	44,8	29,8
20	42,0	28,6
40	48,8	31,8
60	53,7	43,4

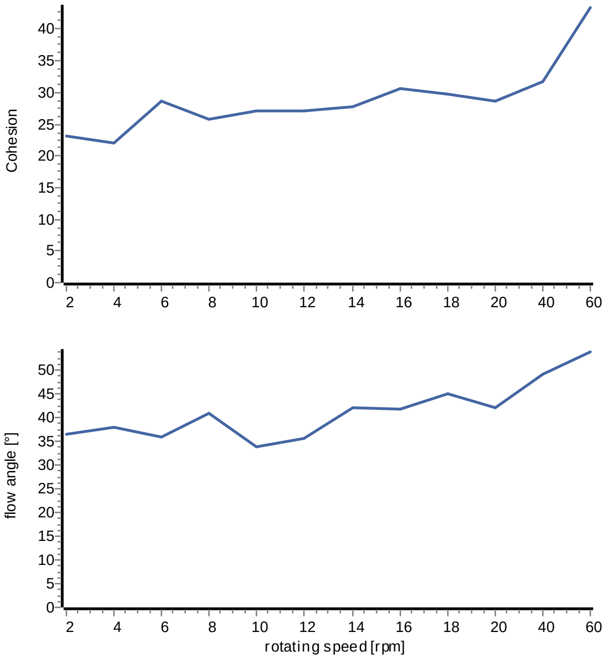

Operator notes: 92W Vit 105 Amloy ZR02

Date and signature of the operator:

GRANUDRUM™

GranuDrum Measurement Report

Sample name : 0094W_St14404
Sample group : DLR

User name: user
2022.11.22 17:38:16

Analysis parameters :

Mode : Speeds Sequence
#Frames : 20
Sampling [ms] : 1000

BWThreshold : 94
CropRatio [%] : 10
Frame [pixels] : 972x972

Powder information :

Volume [ml] : 50
Weight [g] : 260
Temperature [°C] : 21,9
Hygrometry [%] : 25,00

Speeds Sequence

	Sequence	
RPM	**Angle**	**Cohesion**
2	26,7	5,5
4	28,7	10,3
6	31,1	11,4
8	31,7	13,7
10	33,5	14,1
12	36,3	14,7
14	38,6	17,2
16	40,1	16,1
18	42,6	15,3
20	43,5	13,6
40	59,0	12,2
60	66,7	18,3

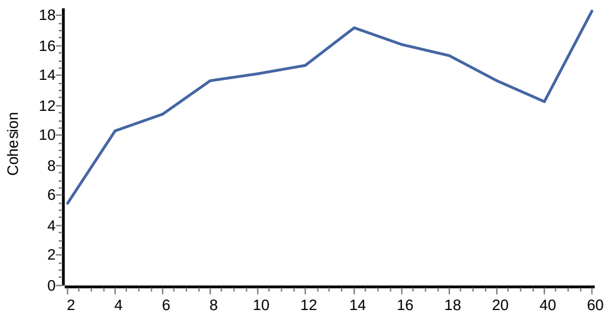

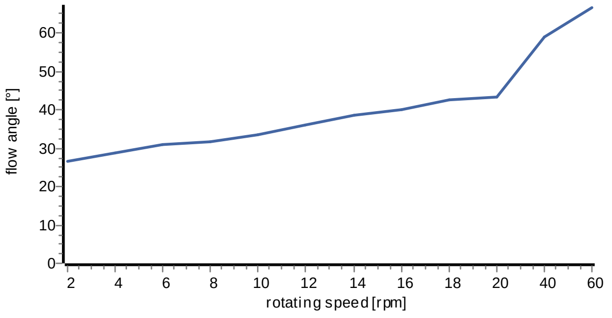

Operator notes: 94W St 1.4404 20-53µm

Date and signature of the operator:

GRANUTOOLS™

Appendix D

Samples and methods used

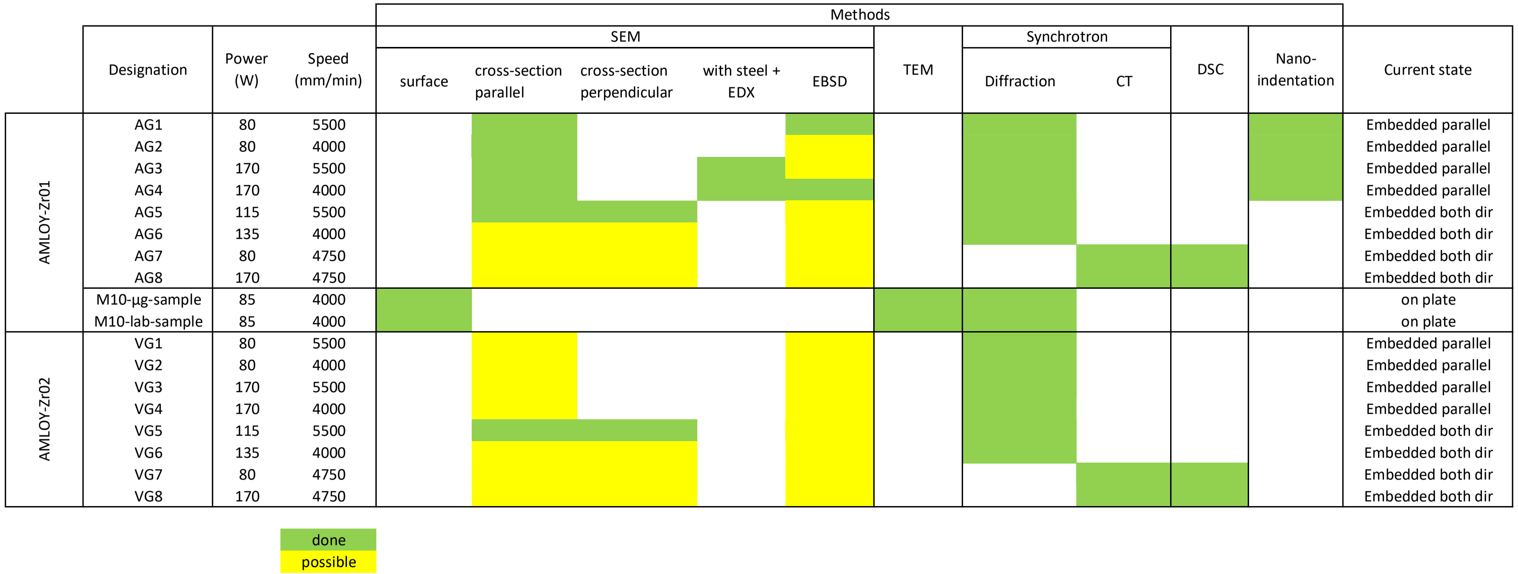

	Designation	Power (W)	Speed (mm/min)	Methods										Current state
				SEM					TEM	Synchrotron		DSC	Nano-indentation	
				surface	cross-section parallel	cross-section perpendicular	with steel + EDX	EBSD		Diffraction	CT			
AMLOY-Zr01	AG1	80	5500		🟩			🟩		🟩			🟩	Embedded parallel
	AG2	80	4000		🟩			🟨		🟩			🟩	Embedded parallel
	AG3	170	5500		🟩		🟩	🟨		🟩			🟩	Embedded parallel
	AG4	170	4000		🟩		🟩	🟩		🟩			🟩	Embedded parallel
	AG5	115	5500		🟩	🟩		🟨		🟩				Embedded both dir
	AG6	135	4000		🟨	🟨		🟨		🟩				Embedded both dir
	AG7	80	4750		🟨	🟨		🟨			🟩	🟩		Embedded both dir
	AG8	170	4750		🟨	🟨		🟨			🟩	🟩		Embedded both dir
	M10-µg-sample	85	4000	🟩					🟩	🟩				on plate
	M10-lab-sample	85	4000	🟩					🟩	🟩				on plate
AMLOY-Zr02	VG1	80	5500		🟨			🟨		🟩				Embedded parallel
	VG2	80	4000		🟨			🟨		🟩				Embedded parallel
	VG3	170	5500		🟨			🟨		🟩				Embedded parallel
	VG4	170	4000		🟨			🟨		🟩				Embedded parallel
	VG5	115	5500		🟩	🟩		🟨		🟩				Embedded both dir
	VG6	135	4000		🟨	🟨		🟨		🟩				Embedded both dir
	VG7	80	4750		🟨	🟨		🟨			🟩	🟩		Embedded both dir
	VG8	170	4750		🟨	🟨		🟨			🟩	🟩		Embedded both dir

🟩	done
🟨	possible

Figure D.1: Overview of the methods applied and to which samples (parameter sets).

Appendix E

Additional graphical results

E.1 Synchrotron diffraction

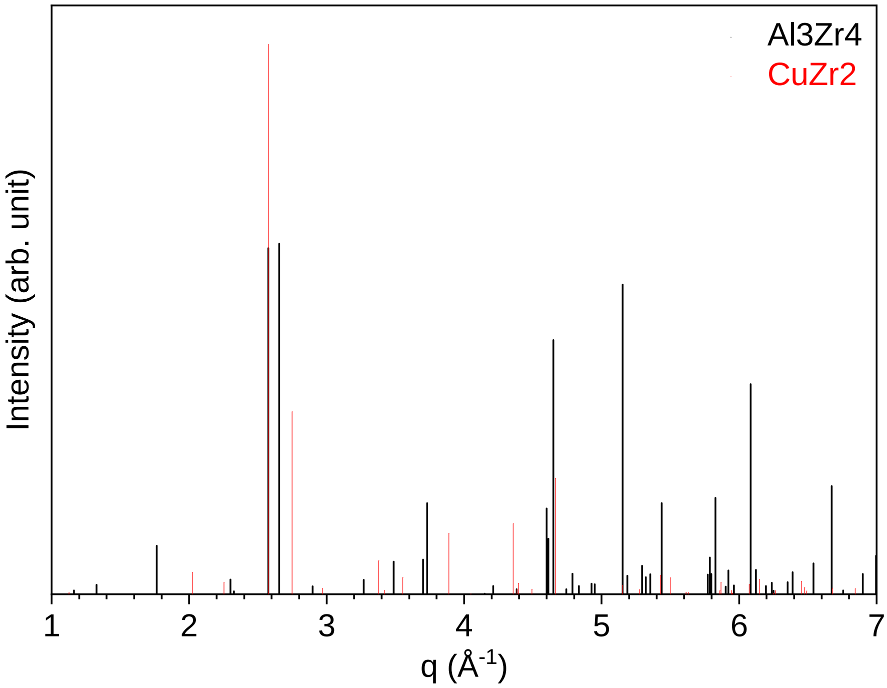

Figure E.1: Bragg peaks identifying $CuZr_2$ *and* Al_3Zr_4*.*

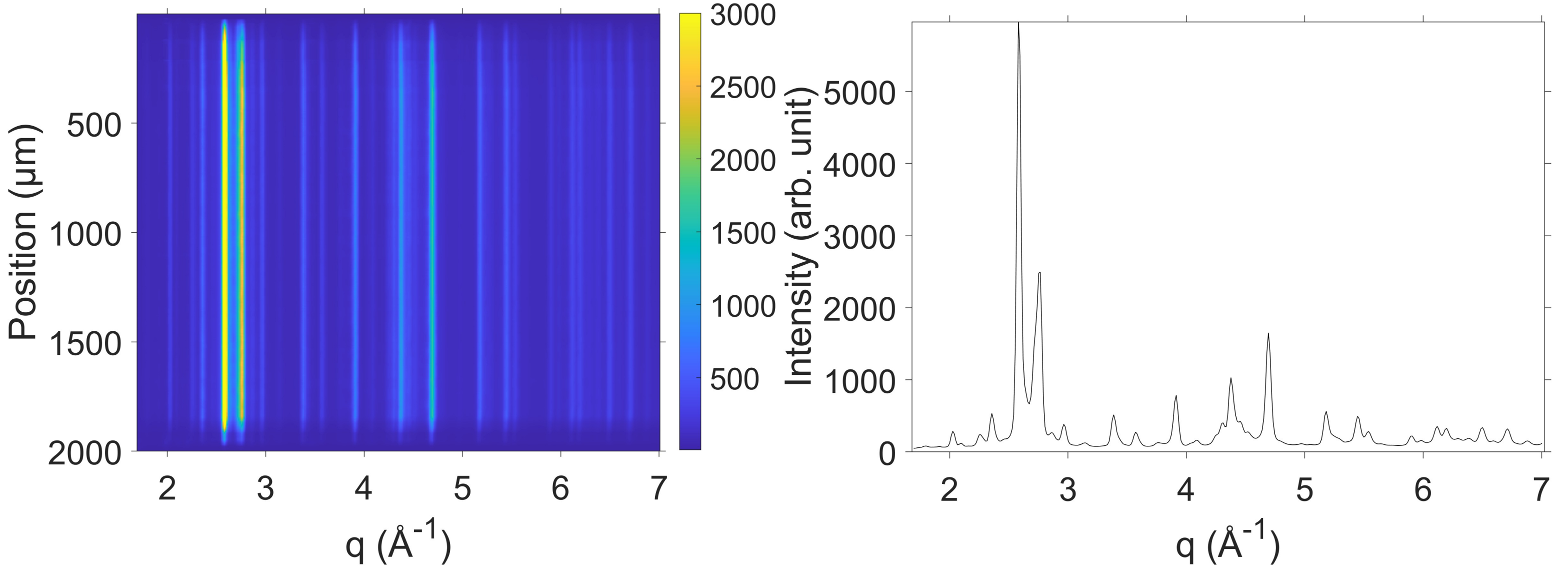

(a) *(b)*

Figure E.2: (a) Scan of the AMLOY-Zr01 sample built 170 W *and* 4000 mm min^{-1} *and forcibly recrystallised (maintained at* 600 °C *for* 5 h*). (b) Example of a diffraction pattern extracted from (a). Intensity is capped for the visibility of smaller peaks in (a).*

E.2 DSC

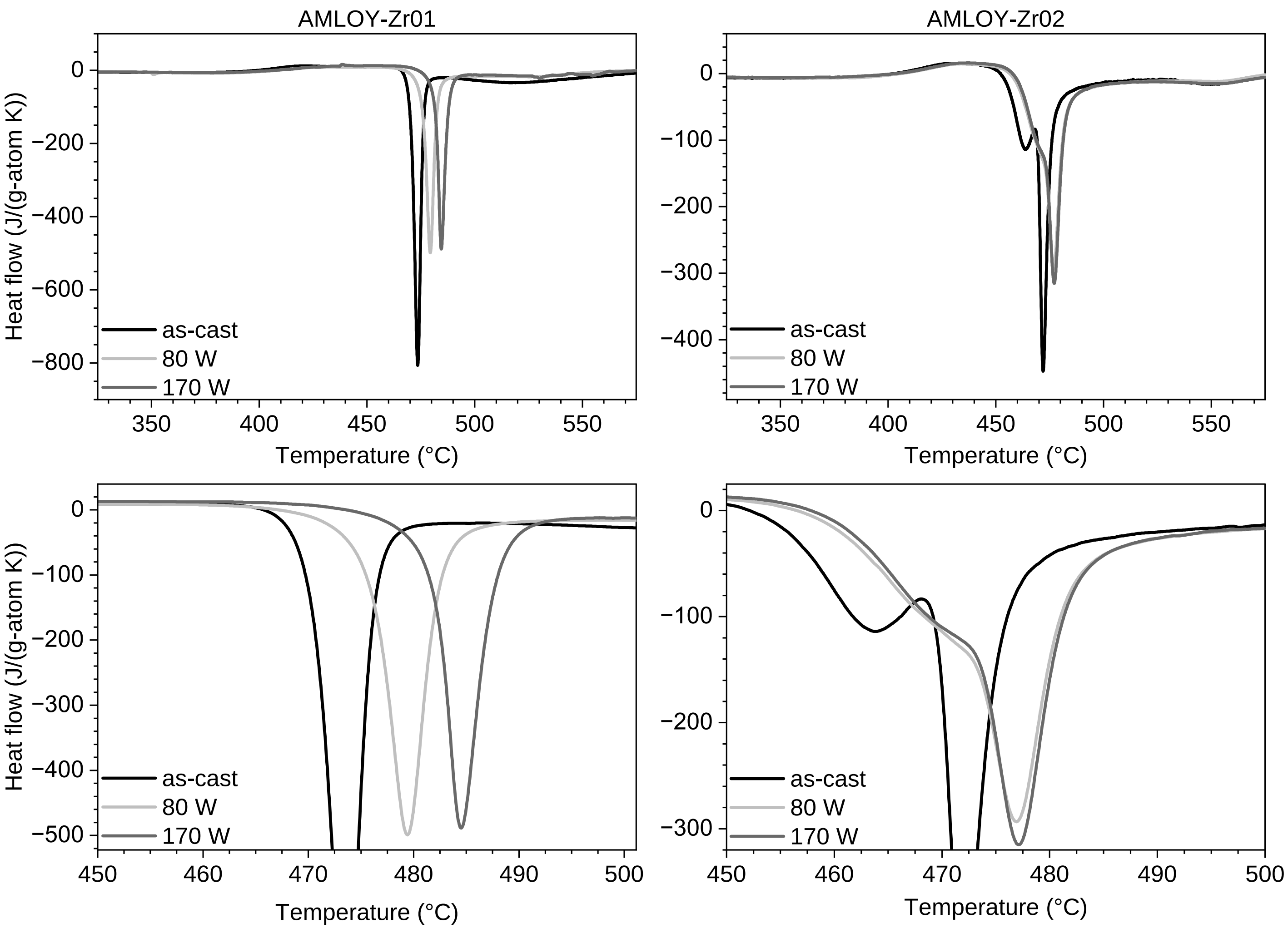

Figure E.3: (Top) Variations of heat flow with temperature of (left) AMLOY-Zr01 and (right) AMLOY-Zr02 of samples built with different laser powers, compared to the as-cast samples. (Bottom) Zoomed sections of (top).

E.3 Nanoindentation

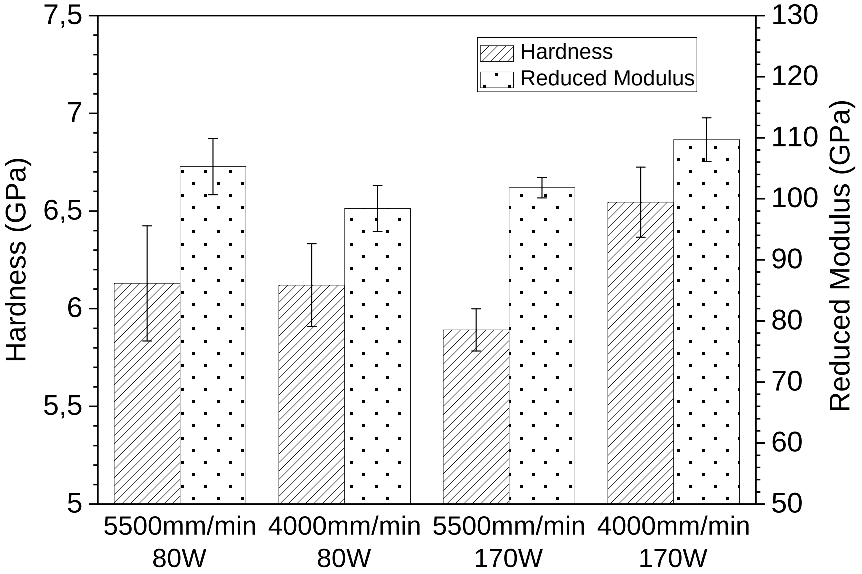

Figure E.4: Average nanohardness and reduced modulus results for varying build parameters.

Appendix F

MARS-X

This chapter provides a more detailed description of the design criteria and the operation of the MARS-X device.

F.1 Design and construction

The development of MARS-M for microgravity experiments on sounding rockets included device miniaturisation, gas-flow assisted deposition of the powder bed, and remote control. These advantages were also applied to MARS-X. The device is compact (its footprint is 400 mm × 400 mm, with max. height 660 mm) and lightweight (total mass less than 70 kg) and therefore easily transportable to the beamline. As previously mentioned, the build-platform is positioned vertically thanks to the gas-flow assisted powder deposition. As a part of lessons learned from MARS-M, the MARS-X build-platform is equipped with an improved Z-axis and upgraded software control.

Some of the design criteria are slightly different to those of MARS-M for the following reasons. Firstly, during experiments the device functions under normal gravity conditions and within normal atmosphere. Secondly, the device must allow the synchrotron beam to pass through it (and at specific entry and exit points) and reach the build-platform, which also implies additional laser-related safety measures. Lastly, MARS-X requires neither internal power (supply) nor internal gas supply.

F.2 Description of device

The building process happens in an easily removable cartridge which includes amongst others the powder container and the build-platform. The powder is stabilised by a closed gas loop passing by having a rubber hose attached to the mounting adapter for the build-platform, allowing vacuum generation below it. Because of the platform's porosity, a gas stream perpendicular to the surface is generated, pushing powder particles towards it. Outside of the cartridge, the gas stream is directed through a set of 10 µm particle filters, and a mass flow sensor (Red-Y series, Vögtlin Instruments GmbH), into two parallel acting controllable diaphragm pumps, type 3111.610 (Boxer GmbH). The build-platform is larger than that in MARS-M, as in this case it is the build-platform that provides the scanning movement during experiments.

The laser system consists of a fibre coupled diode laser as source, laser optics attached to the fibre end, diode driver electronics, a laser cooler system, and laser safety features. For the selective laser melting process a laser diode bar module is used, type Coherent IS58, with max. 283 W optical power delivered at centre wavelength of 976 nm into a 100 µm fibre core. The laser optic is assembled using standard C-mount lens adapters, a SMA-type fibre adapter, and laser-grade plano-convex lenses. All 1”-lenses are $\lambda/10$ grade uncoated Fused Silica lenses (Edmund Optics, Inc.). The front lens has a focal length of 35 mm, and focusses into a 80 µm laser spot on the build plate. A temperature sensor is attached to the optic’s assembly in order to avoid overheating – mostly due to the presence of dust.

Safety requirements for high energy lasers in beamline settings require multiple fail-safes to avoid damaging the hutch equipment. The implemented safety features are displayed in fig. F.1. An interlock circuit, a key switch, a warning light, and redundant relays for laser power are safety features to prevent laser power emittance, rendering the overall set-up a class 1 laser system. At the beamline, however, beam windows are in place that are laser transparent too, rendering the overall set-up class 4. Additionally to the

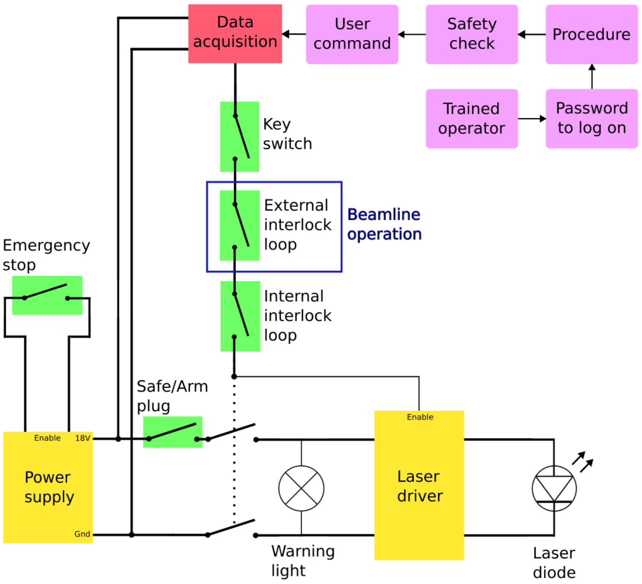

Figure F.1: Schematic of the inbuilt laser safety features of MARS-X.

previously mentioned safety features, the device has an interface to connect an external room interlock. Without this external confirmation that the hutch is closed and no personnel is present, the laser source is not powered and the driver is disabled. The safety system is designed to be failure tolerant. At any time, the laser spot is on the build plate only. No direct laser beam passes the windows, or hits other parts of the chamber – that includes that no direct laser beam can hit the X-ray detector or other items in the hutch. Scattered laser light can, however, it is not able to harm items or cause fire.

The experiment chamber is designed to resist under-pressure: a difference of up to 1 bar is needed when evacuating the atmosphere in preparation for flushing with the desired gas composition. The total chamber volume is around 7 L. The planned pressure range is 0.3 to 1.05 bar abs. The pressure system is two-failure tolerant.

The beam windows are made of Kapton film (160 µm thickness) framed by the device structure and with additional "glazing bars" (a grid increasing the stability of the film during continuous gas atmosphere purging). The experiment chamber can be rotated along the device's height to move the beam windows to change the q-range reaching the detector. The laser can be moved in a limited range for the purpose of calibration between the laser spot and the synchrotron beam spot positions on the powder bed.

The incoming beam is expected at about 100 mm above bottom side of the baseplate – we bring a 150 mm spacer to meet P23's hexapod requirements ($100 + 150 \overset{\wedge}{=} 251 \pm 25$). Our device needs 230 $\mathrm{V_{ac}}$ input at up to 1.3 kW and an at least 100 Mbit/sec Ethernet-connection to the control room. It needs to have a vacuum pump and a gas bottle connected, located within 5 m.

Bibliography

1. Neumann, C. *et al.* Additive manufacturing of metallic glass from powder in space. *NPJ microgravity* **9,** 80. ISSN: 2373-8065 (2023).
2. Zocca, A. *et al.* Challenges in the Technology Development for Additive Manufacturing in Space. *Chinese Journal of Mechanical Engineering: Additive Manufacturing Frontiers* **1,** 100018. ISSN: 27726657 (2022).
3. Clozel, M. *et al.* Microstructure formation during gas flow-assisted additive manufacturing of a metallic glass powder on ground and in microgravity. *Progress in Additive Manufacturing* (2025).
4. Zocca, A. *et al.* Enabling the 3D Printing of Metal Components in µ–Gravity. *Advanced Materials Technologies* **4,** 1900506. ISSN: 2365-709X (2019).
5. Culpan, D. *ISS finally resupplied after unprecedented string of failures* Wired.com, 2015. `https://www.wired.com/story/iss-supplies/`.
6. Gibson, I., Rosen, D. W. & Stucker, B. *Additive Manufacturing Technologies* (Springer US, Boston, MA, 2010).
7. Gibson, I., Rosen, D. & Stucker, B. *Additive Manufacturing Technologies* (Springer New York, New York, NY, 2015).
8. *Additive Manufacturing Technologies* (eds Gibson, I., Rosen, D., Stucker, B. & Khorasani, M.) (Springer International Publishing, Cham, 2021).
9. Srivastava, M., Rathee, S., Patel, V., Kumar, A. & Koppad, P. G. A review of various materials for additive manufacturing: Recent trends and processing issues. *Journal of Materials Research and Technology* **21,** 2612–2641. ISSN: 22387854 (2022).
10. Herderick, E. Additive Manufacturing of Metals: A Review. *Materials Science and Technology (MS&T)* (2011).
11. Williams, E. & Lavery, N. Laser processing of bulk metallic glass: A review. *Journal of Materials Processing Technology* **247,** 73–91. ISSN: 09240136 (2017).
12. Sanchez, S. *et al.* Powder Bed Fusion of nickel-based superalloys: A review. *International Journal of Machine Tools and Manufacture* **165,** 103729. ISSN: 08906955 (2021).

13. Sohrabi, N., Jhabvala, J. & Logé, R. E. Additive Manufacturing of Bulk Metallic Glasses—Process, Challenges and Properties: A Review. *Metals* **11,** 1279 (2021).
14. Mühler, T., Gomes, C. M., Heinrich, J. & Günster, J. Slurry-Based Additive Manufacturing of Ceramics. *International Journal of Applied Ceramic Technology* **12,** 18–25. ISSN: 1546542X (2015).
15. Zocca, A., Colombo, P., Gomes, C. M. & Günster, J. Additive Manufacturing of Ceramics: Issues, Potentialities, and Opportunities. *Journal of the American Ceramic Society* **98,** 1983–2001. ISSN: 00027820 (2015).
16. Goodridge, R. & Ziegelmeier, S. in *Laser additive manufacturing* (ed Brandt, M.) 181–204 (Elsevier and Woodhead Publishing, Amsterdam, Boston, and Cambridge, 2016). ISBN: 978-0-08-100433-3.
17. Kusoglu, I. M., Doñate-Buendía, C., Barcikowski, S. & Gökce, B. Laser Powder Bed Fusion of Polymers: Quantitative Research Direction Indices. *Materials* **14,** 1169. ISSN: 1996-1944 (2021).
18. Ashby, M. & Greer, A. L. Metallic glasses as structural materials. *Scripta Materialia* **54,** 321–326. ISSN: 13596462 (2006).
19. Kruzic, J. J. Bulk Metallic Glasses as Structural Materials: A Review. *Advanced Engineering Materials* **18,** 1308–1331. ISSN: 14381656 (2016).
20. Greer, A. L. & Ma, E. Bulk Metallic Glasses: At the Cutting Edge of Metals Research. *MRS Bulletin* **32,** 611–619. ISSN: 0883-7694 (2007).
21. Bordeenithikasem, P., Stolpe, M., Elsen, A. & Hofmann, D. C. Glass forming ability, flexural strength, and wear properties of additively manufactured Zr-based bulk metallic glasses produced through laser powder bed fusion. *Additive Manufacturing* **21,** 312–317. ISSN: 22148604 (2018).
22. Li, X. P., Roberts, M. P., O'Keeffe, S. & Sercombe, T. B. Selective laser melting of Zr-based bulk metallic glasses: Processing, microstructure and mechanical properties. *Materials & Design* **112,** 217–226. ISSN: 02641275 (2016).
23. Best, J. P. *et al.* Fracture and fatigue behaviour of a laser additive manufactured Zr-based bulk metallic glass. *Additive Manufacturing* **36,** 101416. ISSN: 22148604 (2020).
24. Suryanarayana, C. & Inoue, A. *Bulk metallic glasses* Second edition (CRC Press Taylor & Francis Group, Boca Raton, 2018).
25. Klement, W., Willens, R. H. & Duwez, P. O. Non-crystalline Structure in Solidified Gold–Silicon Alloys. *Nature* **187,** 869–870. ISSN: 0028-0836 (1960).
26. Schroers, J. Processing of bulk metallic glass. *Advanced materials (Deerfield Beach, Fla.)* **22,** 1566–1597 (2010).

27. Wang, W. H., Dong, C. & Shek, C. H. Bulk metallic glasses. *Materials Science and Engineering: R: Reports* **44,** 45–89. ISSN: 0927796X (2004).

28. Lu, Z. P., Tan, H., Ng, S. C. & Li, Y. The correlation between reduced glass transition temperature and glass forming ability of bulk metallic glasses. *Scripta Materialia* **42,** 667–673. ISSN: 13596462 (2000).

29. Lu, Z. P. & Liu, C. T. Glass formation criterion for various glass-forming systems. *Physical review letters* **91,** 115505 (2003).

30. Lu, Z. P. & Liu, C. T. A new approach to understanding and measuring glass formation in bulk amorphous materials. *Intermetallics* **12,** 1035–1043. ISSN: 09669795 (2004).

31. Kim, Y. J., Busch, R., Johnson, W. L., Rulison, A. J. & Rhim, W. K. Experimental determination of a time–temperature-transformation diagram of the undercooled $Zr_{41.2}Ti_{13.8}Cu_{12.5}Ni_{10.0}Be_{22.5}$ alloy using the containerless electrostatic levitation processing technique. *Applied Physics Letters* **68,** 1057–1059. ISSN: 0003-6951 (1996).

32. Busch, R., Masuhr, A., Bakke, E. & Johnson, W. L. Bulk Metallic Glass Formation from Strong Liquids. *Materials Science Forum* **269-272,** 547–552 (1998).

33. Busch, R., Bakke, E. & Johnson, W. L. Supercooled melting in multicomponent Zr–Al–Cu–Ni diffusion couples. *Applied Physics Letters* **68,** 2945–2947. ISSN: 0003-6951 (1996).

34. Tan, H., Zhang, Y., Ma, D., Feng, Y. & Li, Y. Optimum glass formation at off-eutectic composition and its relation to skewed eutectic coupled zone in the La based La–Al–(Cu,Ni) pseudo ternary system. *Acta Materialia* **51,** 4551–4561. ISSN: 13596454 (2003).

35. Louzguine–Luzgin, D. V., Miracle, D. B. & Inoue, A. Intrinsic and Extrinsic Factors Influencing the Glass–Forming Ability of Alloys. *Advanced Engineering Materials* **10,** 1008–1015. ISSN: 1438-1656 (2008).

36. Sohrabi, N. *Laser powder-bed fusion of metallic alloys with enhanced microstructures and properties* PhD thesis (Lausanne, EPFL, Neuchatel, Suisse, 2021).

37. Morrison, M. L. *et al.* Four-point-bending-fatigue behavior of the Zr-based Vitreloy 105 bulk metallic glass. *Materials Science and Engineering: A* **467,** 190–197. ISSN: 09215093 (2007).

38. Telford, M. The case for bulk metallic glass. *Materials Today* **7,** 36–43. ISSN: 13697021 (2004).

39. Schuh, C. A., Hufnagel, T. C. & Ramamurty, U. Mechanical behavior of amorphous alloys. *Acta Materialia* **55,** 4067–4109. ISSN: 13596454 (2007).

40. Hofmann, D. C. *et al.* Towards additively manufacturing excavating tools for future robotic space exploration. *Engineering Reports.* ISSN: 2577-8196 (2020).
41. Heinrich, J., Busch, R. & Nonnenmacher, B. Processing of a bulk metallic glass forming alloy based on industrial grade Zr. *Intermetallics* **25,** 1–4. ISSN: 09669795 (2012).
42. Hays, C. C. *et al.* Vitrification and determination of the crystallization time scales of the bulk-metallic-glass-forming liquid $Zr_{58.5}Nb_{2.8}Cu_{15.6}$-$Ni_{12.8}Al_{10.3}$. *Applied Physics Letters* **79,** 1605–1607. ISSN: 0003-6951 (2001).
43. Lin, X. *Bulk glass formation and crystallization of Zr-Ti based alloy* PhD thesis (California Institute of Technology, 1997).
44. ISO & ASTM. *Additive manufacturing: General principles - Fundamentals and vocabulary* 11.2011. `https://www.iso.org/obp/ui/#iso:std:iso-astm:52900:ed-2:v1:en` (2023).
45. Di, O., Li, N., Xing, W., Zhang, J. & Liu, L. 3D printing of crack-free high strength Zr-based bulk metallic glass composite by selective laser melting. *Intermetallics* **90,** 128–134. ISSN: 09669795 (2017).
46. Li, X. P., Kang, C. W., Huang, H. & Sercombe, T. B. The role of a low-energy–density re-scan in fabricating crack-free $Al_{85}Ni_5Y_6Co_2Fe_2$ bulk metallic glass composites via selective laser melting. *Materials & Design* **63,** 407–411. ISSN: 02641275 (2014).
47. Li, P. *et al.* Metallurgical reactions and tribological properties of self-lubricating Al-WS2 composites: Laser powder bed fusion Vs. spark plasma sintering. *Materials & Design* **216,** 110543. ISSN: 02641275 (2022).
48. Wits, W. W., de Smit, M., Al-Hamdani, K. & Clare, A. T. Laser powder bed fusion of a Magnesium-SiC metal matrix composite. *Procedia CIRP* **81,** 506–511. ISSN: 22128271 (2019).
49. Gibson, M. A. *et al.* 3D printing metals like thermoplastics: Fused filament fabrication of metallic glasses. *Materials Today* **21,** 697–702. ISSN: 13697021 (2018).
50. Tarasov, S. Y. *et al.* Effect of heat input on phase content, crystalline lattice parameter, and residual strain in wire-feed electron beam additive manufactured 304 stainless steel. *The International Journal of Advanced Manufacturing Technology* **99,** 2353–2363. ISSN: 0268-3768 (2018).
51. Zhang, Y., Lin, X., Wei, L., Liu, F. & Huang, W. Influence of powder size on the crystallization behavior during laser solid forming $Zr_{55}Cu_{30}$-$Al_{10}Ni_5$ bulk amorphous alloy. *Intermetallics* **76,** 1–9. ISSN: 09669795 (2016).

52. Grasso, M. & Colosimo, B. M. Process defects and in situ monitoring methods in metal powder bed fusion: a review. *Measurement Science and Technology* **28,** 044005. ISSN: 0957-0233 (2017).

53. Pauly, S. *et al.* Processing metallic glasses by selective laser melting. *Materials Today* **16,** 37–41. ISSN: 13697021 (2013).

54. Yadroitsev, I. & Smurov, I. Selective laser melting technology: From the single laser melted track stability to 3D parts of complex shape. *Physics Procedia* **5,** 551–560. ISSN: 18753892 (2010).

55. Borlaf, M., Serra-Capdevila, A., Colominas, C. & Graule, T. Development of UV-curable ZrO2 slurries for additive manufacturing (LCM-DLP) technology. *Journal of the European Ceramic Society* **39,** 3797–3803. ISSN: 0955-2219 (2019).

56. Tang, H.-H. & Yen, H.-C. Slurry-based additive manufacturing of ceramic parts by selective laser burn-out. *Journal of the European Ceramic Society* **35,** 981–987. ISSN: 0955-2219 (2015).

57. DebRoy, T. *et al.* Additive manufacturing of metallic components – Process, structure and properties. *Progress in Materials Science* **92,** 112–224. ISSN: 00796425 (2018).

58. Edwards, P., O'Conner, A. & Ramulu, M. Electron Beam Additive Manufacturing of Titanium Components: Properties and Performance. *Journal of Manufacturing Science and Engineering* **135.** ISSN: 1087-1357 (2013).

59. Simchi, A. & Pohl, H. Effects of laser sintering processing parameters on the microstructure and densification of iron powder. *Materials Science and Engineering: A* **359,** 119–128. ISSN: 09215093 (2003).

60. Yang, G. *et al.* Laser solid forming Zr-based bulk metallic glass. *Intermetallics* **22,** 110–115. ISSN: 09669795 (2012).

61. Yadroitsev, I. & Smurov, I. Surface Morphology in Selective Laser Melting of Metal Powders. *Physics Procedia* **12,** 264–270. ISSN: 18753892 (2011).

62. Pattanayak, S. & Sahoo, S. K. Gas metal arc welding based additive manufacturing—a review. *CIRP Journal of Manufacturing Science and Technology* **33,** 398–442. ISSN: 1755-5817 (2021).

63. Vimal, K., Naveen Srinivas, M. & Rajak, S. Wire arc additive manufacturing of aluminium alloys: A review. *Materials Today: Proceedings* **41,** 1139–1145. ISSN: 22147853 (2021).

64. Frazier, W. E. Metal Additive Manufacturing: A Review. *Journal of Materials Engineering and Performance* **23,** 1917–1928. ISSN: 1059-9495 (2014).

65. Furumoto, T. *et al.* Evaluating the thermal characteristics of laser powder bed fusion. *Journal of Materials Processing Technology* **299,** 117384. ISSN: 09240136 (2022).

66. Khairallah, S. A., Anderson, A. T., Rubenchik, A. M. & King, W. E. Laser powder-bed fusion additive manufacturing: Physics of complex melt flow and formation mechanisms of pores, spatter, and denudation zones. *Acta Materialia* **108,** 36–45. ISSN: 13596454 (2016).

67. Chen, Y. *et al.* In-situ Synchrotron imaging of keyhole mode multi-layer laser powder bed fusion additive manufacturing. *Applied Materials Today* **20,** 100650. ISSN: 23529407 (2020).

68. Yadroitsev, I. *Selective laser melting: Direct manufacturing of 3D-objects by selective laser melting of metal powders* ISBN: 3838317947 (Lambert Academic Publishing, Saarbrücken, 2009).

69. Rehme, O. & Emmelmann, C. in *Lasers in manufacturing 2005* (ed Beyer, E.) 227–232 (AT-Fachverl., Stuttgart, 2005). ISBN: 3000164022.

70. Mugwagwa, L., Dimitrov, D., Matope, S. & Yadroitsev, I. Influence of process parameters on residual stress related distortions in selective laser melting. *Procedia Manufacturing* **21,** 92–99. ISSN: 23519789 (2018).

71. Yadroitsev, I., Yadroitsava, I., Bertrand, P. & Smurov, I. Factor analysis of selective laser melting process parameters and geometrical characteristics of synthesized single tracks. *Rapid Prototyping Journal* **18,** 201–208. ISSN: 1355-2546 (2012).

72. Yadroitsev, I., Krakhmalev, P., Yadroitsava, I., Johansson, S. & Smurov, I. Energy input effect on morphology and microstructure of selective laser melting single track from metallic powder. *Journal of Materials Processing Technology* **213,** 606–613. ISSN: 09240136 (2013).

73. Sun, J., Yang, Y. & Di Wang. Parametric optimization of selective laser melting for forming Ti6Al4V samples by Taguchi method. *Optics & Laser Technology* **49,** 118–124. ISSN: 00303992 (2013).

74. Wegner, J., Frey, M., Kleszczynski, S., Busch, R. & Witt, G. Influence of process gas during powder bed fusion with laser beam of Zr-based bulk metallic glasses. *Procedia CIRP* **94,** 205–210. ISSN: 22128271 (2020).

75. King, W. E. *et al.* Observation of keyhole-mode laser melting in laser powder-bed fusion additive manufacturing. *Journal of Materials Processing Technology* **214,** 2915–2925. ISSN: 09240136 (2014).

76. Campanelli, S. L., Casalino, G., Contuzzi, N., Angelastro, A. & Ludovico, A. D. *Analysis of the molten/solidified zone in selective laser melted parts* in *High-Power Laser Materials Processing* (ed Dorsch, F.) (2014), 896311.

77. Ciurana, J., Hernandez, L. & Delgado, J. Energy density analysis on single tracks formed by selective laser melting with CoCrMo powder material. *The International Journal of Advanced Manufacturing Technology* **68,** 1103–1110. ISSN: 0268-3768 (2013).

78. Scipioni Bertoli, U., Wolfer, A. J., Matthews, M. J., Delplanque, J.-P. R. & Schoenung, J. M. On the limitations of Volumetric Energy Density as a design parameter for Selective Laser Melting. *Materials & Design* **113,** 331–340. ISSN: 02641275 (2017).

79. Prashanth, K. G., Scudino, S., Maity, T., Das, J. & Eckert, J. Is the energy density a reliable parameter for materials synthesis by selective laser melting? *Materials Research Letters* **5,** 386–390 (2017).

80. Gu, H. *et al. Influences of Energy Density on Porosity and Microstructure of Selective Laser Melted 17-4PH Stainless Steel* in *Proc. of Solid Freeform Fabrication Symp.* (2013), 474–479.

81. Madison, J. D. & Aagesen, L. K. Quantitative characterization of porosity in laser welds of stainless steel. *Scripta Materialia* **67,** 783–786. ISSN: 13596462 (2012).

82. Aboulkhair, N. T., Everitt, N. M., Ashcroft, I. & Tuck, C. Reducing porosity in AlSi10Mg parts processed by selective laser melting. *Additive Manufacturing* **1-4,** 77–86. ISSN: 22148604 (2014).

83. Trapp, J., Rubenchik, A. M., Guss, G. & Matthews, M. J. In situ absorptivity measurements of metallic powders during laser powder-bed fusion additive manufacturing. *Applied Materials Today* **9,** 341–349. ISSN: 23529407 (2017).

84. Zhang, J. *et al.* Influence of Particle Size on Laser Absorption and Scanning Track Formation Mechanisms of Pure Tungsten Powder During Selective Laser Melting. *Engineering* **5,** 736–745. ISSN: 20958099 (2019).

85. Tremsin, A. S. *et al.* Monitoring residual strain relaxation and preferred grain orientation of additively manufactured Inconel 625 by in-situ neutron imaging. *Additive Manufacturing* **46,** 102130. ISSN: 22148604 (2021).

86. Mercelis, P. & Kruth, J.-P. Residual stresses in selective laser sintering and selective laser melting. *Rapid Prototyping Journal* **12,** 254–265. ISSN: 1355-2546 (2006).

87. Cheng, B., Shrestha, S. & Chou, K. Stress and deformation evaluations of scanning strategy effect in selective laser melting. *Additive Manufacturing* **12,** 240–251. ISSN: 22148604 (2016).

88. Deng, X., Piotrowski, G., Williams, J. & Chawla, N. Effect of porosity and tension–compression asymmetry on the Bauschinger effect in porous sintered steels. *International Journal of Fatigue* **27,** 1233–1243. ISSN: 01421123 (2005).
89. Ferrar, B., Mullen, L., Jones, E., Stamp, R. & Sutcliffe, C. J. Gas flow effects on selective laser melting (SLM) manufacturing performance. *Journal of Materials Processing Technology* **212,** 355–364. ISSN: 09240136 (2012).
90. Tammas-Williams, S. *et al.* XCT analysis of the influence of melt strategies on defect population in Ti–6Al–4V components manufactured by Selective Electron Beam Melting. *Materials Characterization* **102,** 47–61. ISSN: 10445803 (2015).
91. Leung, C. L. A. *et al.* In situ X-ray imaging of defect and molten pool dynamics in laser additive manufacturing. *Nature communications* **9,** 1355 (2018).
92. Matthews, M. J. *et al.* Denudation of metal powder layers in laser powder bed fusion processes. *Acta Materialia* **114,** 33–42. ISSN: 13596454 (2016).
93. Thijs, L., Verhaeghe, F., Craeghs, T., van Humbeeck, J. & Kruth, J.-P. A study of the microstructural evolution during selective laser melting of Ti–6Al–4V. *Acta Materialia* **58,** 3303–3312. ISSN: 13596454 (2010).
94. Withers, P. J. & Bhadeshia, H. Residual stress. Part 2 – Nature and origins. *Materials Science and Technology* **17,** 366–375. ISSN: 0267-0836 (2001).
95. Stopyra, W., Gruber, K., Smolina, I., Kurzynowski, T. & Kuźnicka, B. Laser powder bed fusion of AA7075 alloy: Influence of process parameters on porosity and hot cracking. *Additive Manufacturing* **35,** 101270. ISSN: 22148604 (2020).
96. Hocine, S. *et al.* A miniaturized selective laser melting device for operando X-ray diffraction studies. *Additive Manufacturing* **34,** 101194. ISSN: 22148604 (2020).
97. Mumtaz, K. & Hopkinson, N. Top surface and side roughness of Inconel 625 parts processed using selective laser melting. *Rapid Prototyping Journal* **15,** 96–103. ISSN: 1355-2546 (2009).
98. Kruth, J.-P., Levy, G., Klocke, F. & Childs, T. Consolidation phenomena in laser and powder-bed based layered manufacturing. *CIRP Annals* **56,** 730–759. ISSN: 00078506 (2007).
99. Gusarov, A. V., Yadroitsev, I., Bertrand, P. & Smurov, I. Model of Radiation and Heat Transfer in Laser-Powder Interaction Zone at Selective Laser Melting. *Journal of Heat Transfer* **131.** ISSN: 0022-1481 (2009).

100. Xia, M. *et al.* Influence of hatch spacing on heat and mass transfer, thermodynamics and laser processability during additive manufacturing of Inconel 718 alloy. *International Journal of Machine Tools and Manufacture* **109,** 147–157. ISSN: 08906955 (2016).

101. Ly, S., Rubenchik, A. M., Khairallah, S. A., Guss, G. & Matthews, M. J. Metal vapor micro-jet controls material redistribution in laser powder bed fusion additive manufacturing. *Scientific reports* **7,** 4085 (2017).

102. Nakamura, H., Kawahito, Y., Nishimoto, K. & Katayama, S. Elucidation of melt flows and spatter formation mechanisms during high power laser welding of pure titanium. *Journal of Laser Applications* **27,** 032012. ISSN: 1042-346X (2015).

103. Simonelli, M. *et al.* A Study on the Laser Spatter and the Oxidation Reactions During Selective Laser Melting of 316L Stainless Steel, Al-Si10-Mg, and Ti-6Al-4V. *Metallurgical and Materials Transactions A* **46,** 3842–3851. ISSN: 1073-5623 (2015).

104. Liu, Y., Yang, Y., Mai, S., Di Wang & Song, C. Investigation into spatter behavior during selective laser melting of AISI 316L stainless steel powder. *Materials & Design* **87,** 797–806. ISSN: 02641275 (2015).

105. Sames, W. J., Medina, F., Peter, W. H., Babu, S. S. & Dehoff, R. R. *Effect of Process Control and Powder Quality on Inconel 718 Produced Using Electron Beam Melting* in *8th International Symposium on Superalloy 718 and Derivatives* (eds Ott, E. *et al.*) (Wiley, 2014), 409–423. ISBN: 9781119016854.

106. Marattukalam, J. J. *et al.* Development of process parameters for selective laser melting of a Zr-based bulk metallic glass. *Additive Manufacturing* **33,** 101124. ISSN: 22148604 (2020).

107. Sohrabi, N. *et al.* Characterization, mechanical properties and dimensional accuracy of a Zr-based bulk metallic glass manufactured via laser powder-bed fusion. *Materials & Design* **199,** 109400. ISSN: 0264-1275 (2021).

108. Best, J. P. *et al.* Structural periodicity in laser additive manufactured Zr-based bulk metallic glass. *Applied Physics Letters* **115,** 031902. ISSN: 0003-6951 (2019).

109. Mahbooba, Z. *et al.* Additive manufacturing of an iron-based bulk metallic glass larger than the critical casting thickness. *Applied Materials Today* **11,** 264–269. ISSN: 23529407 (2018).

110. Krakhmalev, P. *et al.* Microstructure, Solidification Texture, and Thermal Stability of 316 L Stainless Steel Manufactured by Laser Powder Bed Fusion. *Metals* **8,** 643 (2018).

111. Schroers, J., Masuhr, A., Johnson, W. L. & Busch, R. Pronounced asymmetry in the crystallization behavior during constant heating and cooling of a bulk metallic glass-forming liquid. *Physical Review B* **60,** 11855–11858. ISSN: 1098-0121 (1999).
112. Shen, Y., Li, Y. & Tsai, H.-L. Evolution of crystalline phase during laser processing of Zr-based metallic glass. *Journal of Non-Crystalline Solids* **481,** 299–305. ISSN: 00223093 (2018).
113. Zhang, Y. *et al.* Microstructural analysis of $Zr_{55}Cu_{30}Al_{10}Ni_5$ bulk metallic glasses by laser surface remelting and laser solid forming. *Intermetallics* **66,** 22–30. ISSN: 09669795 (2015).
114. Jonas, I., Hembree, W., Yang, F., Busch, R. & Meyer, A. Industrial grade versus scientific pure: Influence on melt properties. *Applied Physics Letters* **112,** 171902. ISSN: 0003-6951 (2018).
115. Pacheco, V. *et al.* Thermal stability and crystallization of a Zr-based metallic glass produced by suction casting and selective laser melting. *Journal of Alloys and Compounds* **825,** 153995. ISSN: 09258388 (2020).
116. Ericsson, A. *et al.* Crystallization of a Zr-based metallic glass produced by laser powder bed fusion and suction casting. *Journal of Non-Crystalline Solids* **571,** 120891. ISSN: 00223093 (2021).
117. Yang, Z. *et al.* Isothermal crystallization kinetics of an industrial-grade Zr-based bulk metallic glass. *Journal of Non-Crystalline Solids* **573,** 121145. ISSN: 00223093 (2021).
118. Dittus, H. Drop tower 'bremen': A weightlessness laboratory on earth. *Endeavour* **15,** 72–78. ISSN: 01609327 (1991).
119. Pletser, V. Short duration microgravity experiments in physical and life sciences during parabolic flights: the first 30 ESA campaigns. *Acta Astronautica* **55,** 829–854. ISSN: 00945765 (2004).
120. Pletser, V. European aircraft parabolic flights for microgravity research, applications and exploration: A review. *REACH* **1,** 11–19. ISSN: 23523093 (2016).
121. Stamminger, A. *et al.* *DLR's Mobile Rocket Base –Flight Opportunities for Israeli Universities and Research Institutes* in *55th Israel Annual Conference on Aerospace Sciences* (IACAS, 2015).
122. Stamminger, A., Altenbuchner, L., Ettl, J., Jung, W. & Turner, P. *MORABA - Overview on DLR's Mobile Rocket Base and Projects* in *SpaceOps 2012 Conference* (2012).
123. Stamminger, A. *et al.* *DLR'S Mobile Rocket Base – Flight tickets for your microgravity experiments* in *64th International Astronautical Congress* **IAC-13-A2.5.10** (2013).

124. Schmidt, A., Stamminger, A. & Turner, P. *DLR's Mobile Rocket Base – 47 years of microgravity and technical experiments on suborbital flights* in *65th International Astronautical Congress* **IAC-14-A2.5.7** (International Astronautical Federation., 2014).

125. Enz, T., Steinbach, S., Simicic, D., Kasperovich, G. & Ratke, L. First Experiments Using the Materials Science Laboratory on Board the International Space Station. *Microgravity Science and Technology* **23,** 345–353. ISSN: 0938-0108 (2011).

126. Günster, J. *Personal communication* (ed Clozel, M.) 31.05.2023.

127. Blochberger, G. *et al.* ATLAS-M and Batt-M: development of flight hardware for MAPHEUS sounding rocket. *Journal of Physics: Conference Series* **327,** 012051. ISSN: 1742-6588 (2011).

128. Carr, R. L. Evaluating flow properties of solids. *Chemical Engineering* **72,** 163–168 (1965).

129. Spierings, A. B., Voegtlin, M., Bauer, T. & Wegener, K. Powder flowability characterisation methodology for powder-bed-based metal additive manufacturing. *Progress in Additive Manufacturing* **1,** 9–20. ISSN: 2363-9512 (2016).

130. Kieffer, J. & Karkoulis, D. PyFAI, a versatile library for azimuthal regrouping. *Journal of Physics: Conference Series* **425,** 202012. ISSN: 1742-6588 (2013).

131. Kieffer, J., Valls, V., Blanc, N. & Hennig, C. New tools for calibrating diffraction setups. *Journal of synchrotron radiation* **27,** 558–566 (2020).

132. Eaton, J. W., Bateman, D., Hauberg, S. & Wehbring, R. *GNU Octave version 7.3.0 manual: a high-level interactive language for numerical computations* (2022). `https://www.gnu.org/software/octave/doc/v7.3.0/`.

133. Inc., T. M. *MATLAB version: 9.13.0 (R2022b)* Natick, Massachusetts, United States, 2022. `https://www.mathworks.com`.

134. Zheng, Q. *et al.* Understanding Glass through Differential Scanning Calorimetry. *Chemical reviews* **119,** 7848–7939 (2019).

135. Slipenyuk, A. & Eckert, J. Correlation between enthalpy change and free volume reduction during structural relaxation of $Zr_{55}Cu_{30}Al_{10}Ni_5$ metallic glass. *Scripta Materialia* **50,** 39–44. ISSN: 13596462 (2004).

136. Oliver, W. C. & Pharr, G. M. An improved technique for determining hardness and elastic modulus using load and displacement sensing indentation experiments. *Journal of Materials Research* **7,** 1564–1583. ISSN: 0884-2914 (1992).

137. Fischer-Cripps, A. C. Critical review of analysis and interpretation of nanoindentation test data. *Surface and Coatings Technology* **200,** 4153–4165. ISSN: 02578972 (2006).

138. Podczeck, F. & Mia, Y. The influence of particle size and shape on the angle of internal friction and the flow factor of unlubricated and lubricated powders. *International Journal of Pharmaceutics* **144,** 187–194. ISSN: 03785173 (1996).

139. Marchetti, L., Mellin, P. & Neil Hulme, C. Negative impact of humidity on the flowability of steel powders. *Particulate Science and Technology* **40,** 722–736. ISSN: 0272-6351 (2022).

140. Meier, C., Weissbach, R., Weinberg, J., Wall, W. A. & Hart, A. J. Critical influences of particle size and adhesion on the powder layer uniformity in metal additive manufacturing. *Journal of Materials Processing Technology* **266,** 484–501. ISSN: 09240136 (2019).

141. Wegner, J. *et al.* Influence of powder characteristics on the structural and the mechanical properties of additively manufactured Zr-based bulk metallic glass. *Materials & Design* **209,** 109976. ISSN: 02641275 (2021).

142. Schneider, C. A., Rasband, W. S. & Eliceiri, K. W. NIH Image to ImageJ: 25 years of image analysis. *Nature Methods* **9,** 671–675. ISSN: 1548-7105 (2012).

143. Andersen, L. M. *Toughness of wear-resistant Cu-Zr-based bulk metallic glasses* (University of California, San Diego, 2016).

144. Yang, Z. *et al.* Evolution of an industrial-grade Zr-based bulk metallic glass during multiple laser beam melting. *Journal of Non-Crystalline Solids* **589,** 121649. ISSN: 0022-3093 (2022).

145. Kawase, D., Tsai, A. P., Inoue, A. & Masumoto, T. Crystallization on supercooled liquid in metallic Zr-Cu-Al glasses. *Applied Physics Letters* **62,** 137–139. ISSN: 0003-6951 (Jan. 1993).

146. Qiang, J. B., Zhang, W., Xie, G. Q. & Inoue, A. The effect of Ti, Nb, and Ta additions to ZrAlCu metallic glass on the crystallization and formation of the icosahedral phase. *Journal of Materials Research* **22,** 1093–1097. ISSN: 2044-5326 (2007).

147. Tidefelt, M. *et al.* In Situ Mapping of Phase Evolutions in Rapidly Heated Zr-Based Bulk Metallic Glass with Oxygen Impurities. *Advanced Science* **11,** 1–13. ISSN: 2198-3844 (2024).

148. Lindwall, J. *et al.* Simulation of phase evolution in a Zr-based glass forming alloy during multiple laser remelting. *Journal of Materials Research and Technology* **16,** 1165–1178. ISSN: 2238-7854 (2022).

149. De Oliveira, M. F., Kaufman, M. J., Botta Filho, W. J. & Kiminami, C. S. The “Big-Cube” Phase Found in Zr-Cu-Al-Ni Easy Glass Forming Alloys. *Materials Science Forum* **403,** 101–106 (2002).

150. Goetz, I. K. *et al.* Convective Flow Redistribution of Oxygen by Laser Melting of a Zr-Based Amorphous Alloy. *Materials* **16,** 4113 (2023).

151. Köster, U., Meinhardt, J., Roos, S. & Liebertz, H. Formation of quasicrystals in bulk glass forming Zr–Cu–Ni–Al alloys. *Applied Physics Letters* **69,** 179–181. ISSN: 0003-6951 (1996).

152. Khare, V. *et al.* Influence of alloying on the formation of Zr-based quasicrystals. *Journal of Non-Crystalline Solids* **334-335,** 23–28. ISSN: 0022-3093 (2004).

153. Köster, U., Zander, D. & Janlewing, R. *Quasicrystal formation, phase selection and crystallization kinetics in Zr-Cu-Ni-Al based metallic glasses* in *Materials Science Forum* **386** (2002), 89–98.

154. Zander, D., Janlewing, R., Rüdiger, A. & Köster, U. Nucleation of quasicrystals in bulk glass forming Zr-Cu-Ni-Al alloys. *Journal of Metastable and Nanocrystalline Materials* **1,** 25–30. ISSN: 2297-6620 (1999).

155. Zander, D., Köster, U. & Khare, V. Hydrogen induced transformations in Zr–Cu–Ni–Al quasicrystals. *Journal of non-crystalline solids* **334,** 247–252. ISSN: 0022-3093 (2004).

156. Nolze, G., Tokarski, T., Rychłowski, Ł., Cios, G. & Winkelmann, A. Crystallographic analysis of the lattice metric (CALM) from single electron backscatter diffraction or transmission Kikuchi diffraction patterns. *Journal of applied crystallography* **54,** 1012–1022. ISSN: 0021-8898 (2021).

157. Sohrabi, N. *et al.* Fatigue Performance of an Additively Manufactured Zr-Based Bulk Metallic Glass and the Effect of Post-Processing. *Metals* **11,** 1064 (2021).

158. Becker, M., Wegener, M., Drescher, J. & Kargl, F. Nucleation and Growth Dynamics of Equiaxed Dendrites in Thin Metallic Al–Cu and Al–Ge Samples in Microgravity and on Earth. *Metallurgical and Materials Transactions A* **54,** 4188–4202. ISSN: 1073-5623 (2023).

159. Nguyen-Thi, H., Reinhart, G. & Billia, B. On the interest of microgravity experimentation for studying convective effects during the directional solidification of metal alloys. *Comptes Rendus Mécanique* **345,** 66–77. ISSN: 16310721 (2017).

160. Liu, H. *et al.* Additive manufacturing of metallic glasses and high-entropy alloys: Significance, unsettled issues, and future directions. *Journal of Materials Science & Technology* **140,** 79–120. ISSN: 10050302 (2023).

161. Wang, J., Zhu, R., Liu, Y. & Zhang, L. Understanding melt pool characteristics in laser powder bed fusion: An overview of single- and multi-track melt pools for process optimization. *Advanced Powder Materials* **2,** 100137. ISSN: 2772834X (2023).

162. Mackay, R., Miller, G. J. & Franzen, H. F. New oxides of the filled-Ti2Ni type structure. *Journal of Alloys and Compounds* **204,** 109–118. ISSN: 0925-8388 (1994).

163. Yan, M., Zou, J. & Shen, J. Cooling rate effects on the microstructure and phase formation in $Zr_{51}Cu_{20.7}Ni_{12}Al_{16.3}$ bulk metallic glass. *Science and Technology of Advanced Materials* **7,** 806. ISSN: 1468-6996 (2006).

164. Wilson, C., Thomas, D. & Spooner, F. The crystal structure of Zr4Al3. *Acta Crystallographica* **13,** 56–57. ISSN: 0365-110X (1960).

165. Sviridova, T., D'yakonova, N., Shelekhov, E. & Glazkov, V. Change of crystal structure of Zr 2 Cu after a treatment in ball mill and annealing. *Poverkhnost'. Rentgenovskie, Sinkhrotronnye i Nejtronnye Issledovaniya,* 28–32 (2004).

166. Takeuchi, A. & Inoue, A. Classification of Bulk Metallic Glasses by Atomic Size Difference, Heat of Mixing and Period of Constituent Elements and Its Application to Characterization of the Main Alloying Element. *Materials Transactions* **46,** 2817–2829 (2005).

167. Herrmann, K. *et al.* Progress in determination of the area function of indenters used for nanoindentation. *Thin Solid Films* **377-378,** 394–400. ISSN: 00406090 (2000).

168. Meneve, J. L., Smith, J. F., Jennett, N. M. & Saunders, S. Surface mechanical property testing by depth sensing indentation. *Applied Surface Science* **100-101,** 64–68. ISSN: 01694332 (1996).

169. McElhaney, K. W., Vlassak, J. J. & Nix, W. D. Determination of indenter tip geometry and indentation contact area for depth-sensing indentation experiments. *Journal of Materials Research* **13,** 1300–1306. ISSN: 0884-2914 (1998).

170. Burgess, T. & Ferry, M. Nanoindentation of metallic glasses. *Materials Today* **12,** 24–32. ISSN: 13697021 (2009).

171. Marimuthu, K. P., Lee, K., Han, J., Rickhey, F. & Lee, H. Nanoindentation of zirconium based bulk metallic glass and its nanomechanical properties. *Journal of Materials Research and Technology* **9,** 104–114. ISSN: 22387854 (2020).

172. Schmeiser, F., Krohmer, E., Schell, N., Uhlmann, E. & Reimers, W. Experimental observation of stress formation during selective laser melting using in situ X-ray diffraction. *Additive Manufacturing* **32,** 101028. ISSN: 22148604 (2020).